UNIVERSITY OF CALIFORNIA

Los Angeles

Development of Tunable Nanoscale Materials for Energy Applications

A dissertation submitted

in partial satisfaction of the requirements for the degree

Doctor of Philosophy in Chemistry

by

Daniel Ian Baumann

2020

ABSTRACT OF THE DISSERTATION

Development of Tunable Nanoscale Materials for Energy Applications

By

Daniel Ian Baumann

Doctor of Philosophy in Chemistry

University of California, Los Angeles, 2020

Professor Xiangfeng Duan, Chair

The demand for energy storage, both portable and stationary, is constantly increasing with the advent of modern technologies like portable electronics and electric vehicles. Supercapacitors are an energy storage technology that can provide high power and long cycle life to devices across a wide variety of applications. Recent studies have explored how various parameters effect supercapacitor performance, however few have studied how to enhance the mass loading of the active material – a crucial criterion for bringing research chemistry to real world applications. This project aims to develop high surface area carbon with tunable hierarchical pores to improve (i) ion conductivity in the pores, (ii) power density/rate capability of ionic liquid electrolytes, (iii) and

increased mass loading of the active material in the device. In addition, modified graphene and lithium sulfur batteries are discussed for applications in catalysis and energy storage respectively.

Chapter 1 presents an introduction to the relevant background for each chapter. Chapter 2 presents how covalent triazine frameworks can be synthesized to have tunable porosities allowing for hierarchical porous networks. In Chapter 3, hierarchical porous frameworks are utilized as supercapacitor active materials for high mass loading devices. Chapter 4 outlines a college level lab for students to get hands on experience with nanomaterials through fabricating supercapacitors out of reduced graphene oxide. Chapter 5 presents a method for functionalizing graphene with triazine motifs, which can be chelated with metals for high metal loading. Chapter 6 probes the chemistry of lithium sulfur batteries, and how using catalysts can help with polysulfide shuttling.

Overall these results emphasize how different nanomaterials can be tuned for a variety of applications including supercapacitors, catalysis, and batteries.

The dissertation of Daniel Ian Baumann is approved.

Jeffrey I. Zink

Sarah H. Tolbert

William M. Gelbart

Xiangfeng Duan, Committee Chair

University of California, Los Angeles

2020

Dedicated to my family and friends near and far,

your support is forever invaluable.

TABLE OF CONTENTS

LIST OF FIGURES

LIST OF TABLES

ACKNOWLEDGMENTS

Getting a PhD is probably the hardest thing I'll ever have to do. It is an emotion filled journey full of frustration, doubt, excitement, pride, and everything in-between. First, I would like to thank my advisor, Professor Xiangfeng Duan. His directness will always be appreciated, as I always knew what was expected of me. His guidance throughout my years of graduate school allowed me to grow into the scientist I am today. Another person who has had a huge impact on my life is Dr. Shannon Stitzel, from Towson University. She set me on the path to graduate school, and for that I'm forever grateful. I would also like to take the time to thank Professor Sarah Tolbert. She taught me one of the most valuable skills a scientist can have – how to make a flawless PowerPoint and present it like a true salesman. I also want to thank Professor Bill Gelbart and Professor Zink for taking the time to be on my committee and providing me with advice for the future. The last professor I'd like to thank is Professor Johnny Pang. While most grad students consider teaching a hassle, I found it the opposite because of Dr. Pang. Thank you to Dan Zhu and Frank Song for being excellent lab mates and friends, our conversations were always something else. Thank you Chengzhang Wan, a dear friend, and one of the most intelligent and humble scientists I've ever met. I've had some exceptional mentors in the Duan lab. I want to thank Dr. Benjamin Papandrea, Dr. Chain Lee, and Dr. Boris Volosskiy for being excellent mentors, and guiding me in the beginning of my graduate school career. You three taught me the skills and techniques I used every day. Thank you all for your guidance and support.

My time at UCLA has been spent with some of the most wonderful people on planet Earth. I feel incredibly lucky to be a part of the 2015 chemistry cohort, which I firmly believe (albeit with heavy bias) to be the most fun cohort the chemistry department has ever had. Not only have the people in California supported me, but so have my friend and family abroad. Thank you all. To

my family, for loving and supporting me unconditionally, for my entire life. I especially want to thank my father, Dr. Michael Baumann, who nurtured my curiosity and love for science, even when some “experiments” may have been (slightly) dangerous. To my friends in Baltimore for including me in their everyday life even though I’m 2500 miles away. To Dan Hatfield and Erick Harr, my first two friends at UCLA who made the transition to California so much fun. To Priera Panescu for putting up with me. To Justyna, Nick, and Annie for making sure I never missed a deadline. To Ohara’s and Barney’s, where friendships were forged and the greatest ideas were never remembered. To Kyle Tamshen, Patrick Yee, Mary & Johnathon Grumbles, Yolanda Li, Mit Muni, and so many more. Lastly, I’d like to thank KJ Winchell. You have always been my biggest supporter. The last 4 years with you have been wonderful and I can’t wait to see where our future takes us. I thank you all from the bottom of my heart. I’m filled with gratitude that each and every one of you is in my life, because you’ve made my journey through grad school unforgettable.

Previous Publications and Contributions of Co-Authors

Chapter 2 is a version of "Hierarchical Porous Carbon Derived from Covalent Triazine Frameworks for High Mass Loading Supercapacitors". Dr. Chain Lee's concepts started the ideas for the paper. He also taught me the CTF synthesis. Chengzhang Wan took TEM images as well as helped edit the paper. I collected all other data and wrote the manuscript.

Chapter 3 is a version of "Hierarchical Porous Carbon Derived from Covalent Triazine Frameworks for High Mass Loading Supercapacitors". Dr. Hontao Sun taught me how to make electrodes and test them. I performed all experiments.

Chapter 4 and Appendix A are a lab developed for Chem 185/285. I created the lab under the direction of Dr. Xiangfeng Duan. Ignacio Martini was pivotal in the troubleshooting of the instruments to get the lab running in the undergraduate lab. I designed the lab, and the students of CHEM 185 provided the data in the chapter.

Chapter 5 are preliminary experiments for a new project where all experiments were performed by me.

Chapter 6 was work completed with the help of Dr. Benjamin Papandrea. Dr. Papandra and I contributed equally to the project from concepts to experiments.

BIOGRAPHICAL SKETCH

Education:

University of California, Los Angeles	Los Angeles, CA
Advancement to Candidacy	June 2017
PhD, Materials Chemistry	2015 – Present
Towson University	Towson, MD
B.S., Major in Chemistry, Minor in Physics	2011 – 2015

Publications:

Daniel Baumann, Chain Lee, Chengzhang Wan, Hongtao Sun, Xiangfeng Duan. Hierarchical porous carbon derived from covalent triazine frame-works for high mass loading supercapacitors. *ACS Materials Letters*. (Accepted).

Zheng Fan, Liqiang Zhang, **Daniel Baumann**, Lin Mei, Yuxing Yao, Xidong Duan, Yumeng Shi, Jianyu Huang, Yu Huang, and Xiangfeng Duan. In situ transmission electron microscopy for energy materials and devices. *Advanced Materials*. 1900608, 1–22 (2019).

Hongtao Sun, Jian Zhu, **Daniel Baumann**, Lele Peng, Yuxi Xu, Imran Shakir, Yu Huang, and Xiangfeng Duan. Hierarchical 3D electrodes for electrochemical energy storage. *Nature Reviews Materials*, 4, 45–60 (2019).

Presentations/Posters:

Presentation. "Hierarchical porous carbon derived from covalent triazine frame-works for high mass loading supercapacitors" D. Baumann, Chain Lee, Chengzhang Wan, Hongtao Sun, Xiangfeng Duan. ACS National Meeting San Diego, CA. Aug. 2019

Presentation. "Hierarchical Porous N-doped Carbon Derived from Covalent Triazine Frameworks for Energy Storage" D. Baumann, X. Duan. University of California, Los Angeles, CA. Nov. 2018

Poster. "Cross-linking Monomer Effect on Response of Molecularly Imprinted Polymers for Metal Ion Detection" D. Baumann, S. Stitzel, C. Zanelotti, T. Mai, ACS National Meeting Denver, CO. March 2015

Poster. "Cross-Linker Effect on Specificity of Molecularly Imprinted Polymers" D. Baumann, S. Stitzel. Towson University Undergraduate Research Symposium, MD. April 2014, 2015

Poster. "Factors Affecting the Formation of Non-Covalent Complexes Between the Well Known A_{2a} and D_2 Receptors" D. Baumann, S. Jackson, and A. Woods. National Institute of Health, MD. August 2014

CHAPTER 1: INTRODUCTION AND BACKGROUND

1.1 A Broad View of Energy Storage

Today's portable electronics, electric vehicles, and much more would not exist without the research and development of energy storage devices (ESDs). Advancements in this field are more important than ever due to the constant increasing demand for such devices. In addition, energy storage is vital to a sustainable and renewable energy future as the majority of renewable energies *produce* energy, and cannot *store* energy. This work primarily focuses on the development of high surface area, hierarchical porous carbons for supercapacitor applications. In addition, lithium sulfur chemistry is explored as well as the modification of graphene.

Energy storage technologies come in a variety of flavors, and the main way to compare different devices is by measuring their energy density and power density. Energy density is the total amount of charge per unit mass/volume and power density is a measure of how quickly that charge can be applied per unit mass/volume (Figure 1a). Battery technologies generally have high energy density but low power density, and supercapacitors are the opposite with high power and

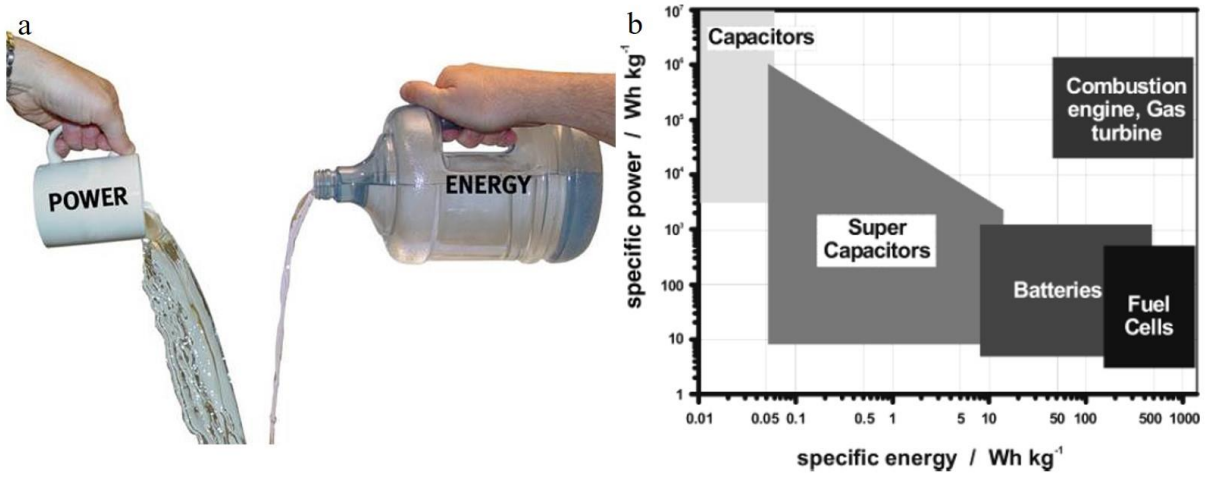

Figure 1. (a) Depiction of power and energy. (b) Ragone plot of various energy storage devices.[1]

low energy densities. By graphing power vs energy, termed a Ragone plot, one can visualize the differences between different storage types (Figure 1b).[1] The overall goal of energy storage technologies is to have a device with both high power and energy densities. However, they usually come at the expense of one another due to intrinsic mechanisms of the various storage methods. Some of the only devices able to generate both high power and energy are combustion engines which rely on the burning of fossil fuels. However, there is a push to develop competitive storage systems that does not rely on such environmentally harmful methods. In these research projects, various approaches are used to enhance either the supercapacitor or battery's position on the Ragone plot; for supercapacitors, the energy density is increased and for batteries the power is increased. We hope to contribute to the development of these technologies to one day replace the combustion engine altogether for a sustainable future.

1.2 Covalent Organic Frameworks

Covalent organic frameworks (COFs) were first developed in 2005 by Dr. Omar Yaghi.[2] COFs are unique set of polymers that have high crystallinity, porosity, and surface area. The pore size can be controlled through the monomers used and surface areas of over 2500 m^2/g have been achieved.[3,4] Due to these characteristics, COFs have a variety of uses like CO_2 & H_2 storage and catalysis. They can be constructed from an almost infinite array of organic building blocks leading to an extensive library of COFs with a variety of predetermined 2D or 3D geometries (Figure 2). The most common COFs contain boron-oxygen linkages but they can also contain carbon-nitrogen linkages. The main prerequisite for synthesis is that the bonding of monomers is reversible. This condition allows for a 'self-correcting' of the polymer structure producing a thermodynamically stable, crystalline product frequently taking many days for the reaction to finish. Due to the nature

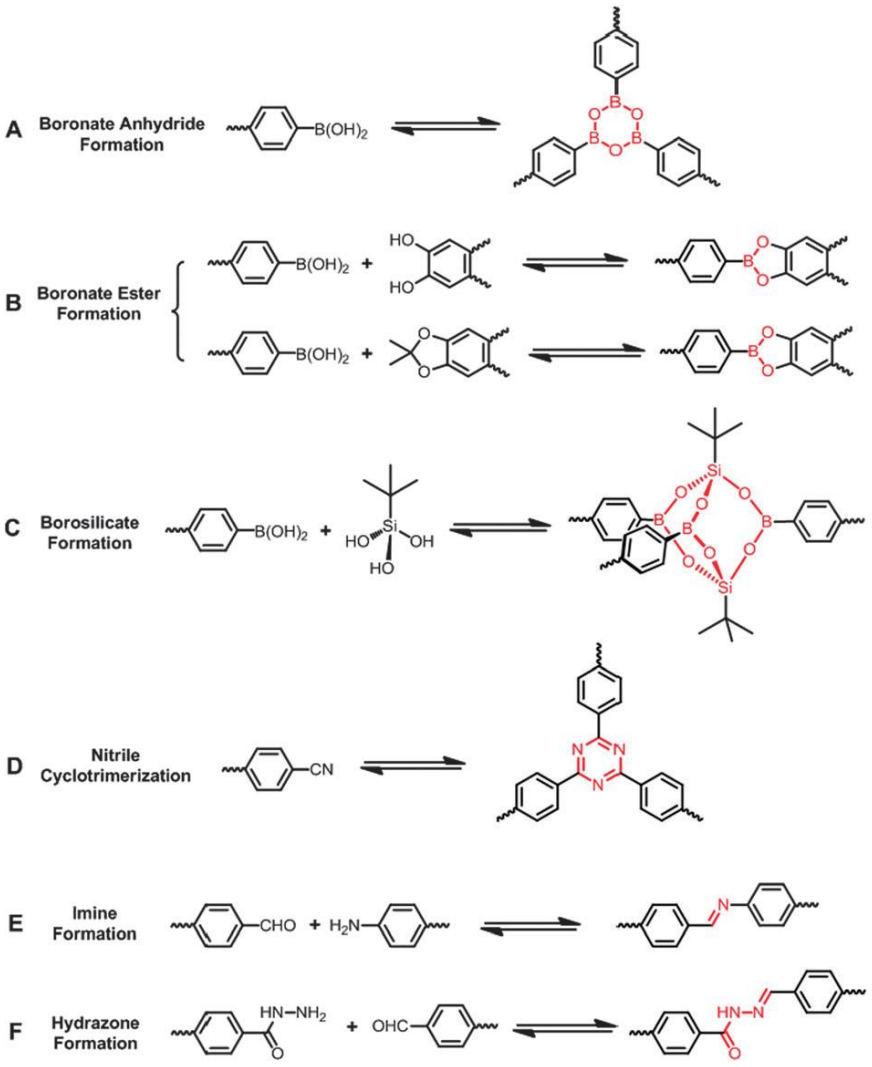

Figure 2. Various types of COF preparations containing boron-oxygen linkages (a-c) as well as carbon-nitrogen linkages (d-f).[3]

of COF's being networks of covalent bonds, most are completely nonconductive limiting their use in electrochemical applications.[5] To overcome this problem, many solutions have been explored. One of the most common ways to increase conductivity is to pyrolyze of the COF to generate conductive graphitized carbon, however this method is difficult to control.[6] Another more controllable method is to use conjugated building blocks to impart intrinsic conductivity in the final structure. To this end, a class of COF termed covalent triazine frameworks (CTFs) were developed that has a fully conjugated backbone allowing for much higher conductivity.

1.2.1 Fundamentals of Covalent Triazine Frameworks

Covalent triazine frameworks were first reported by Kuhn et al.[7] These CTFs are formed by the trimerization of aromatic nitriles at high temperatures (>400 °C) in molten zinc chloride (Figure 3a). More recent synthesis methods include a superacid catalyzed route as well as a Friedel Crafts reaction route.[8,9] The structure is dependent on the monomer used giving rise to various geometries (Figure 3b & c). The resulting CTFs have limited periodicity because of the diminished reversibility of the trimerization reaction. Triazines are very stable, thus the reverse reaction is impeded. However, this gives the CTF's very high stability, both chemically and physically. In

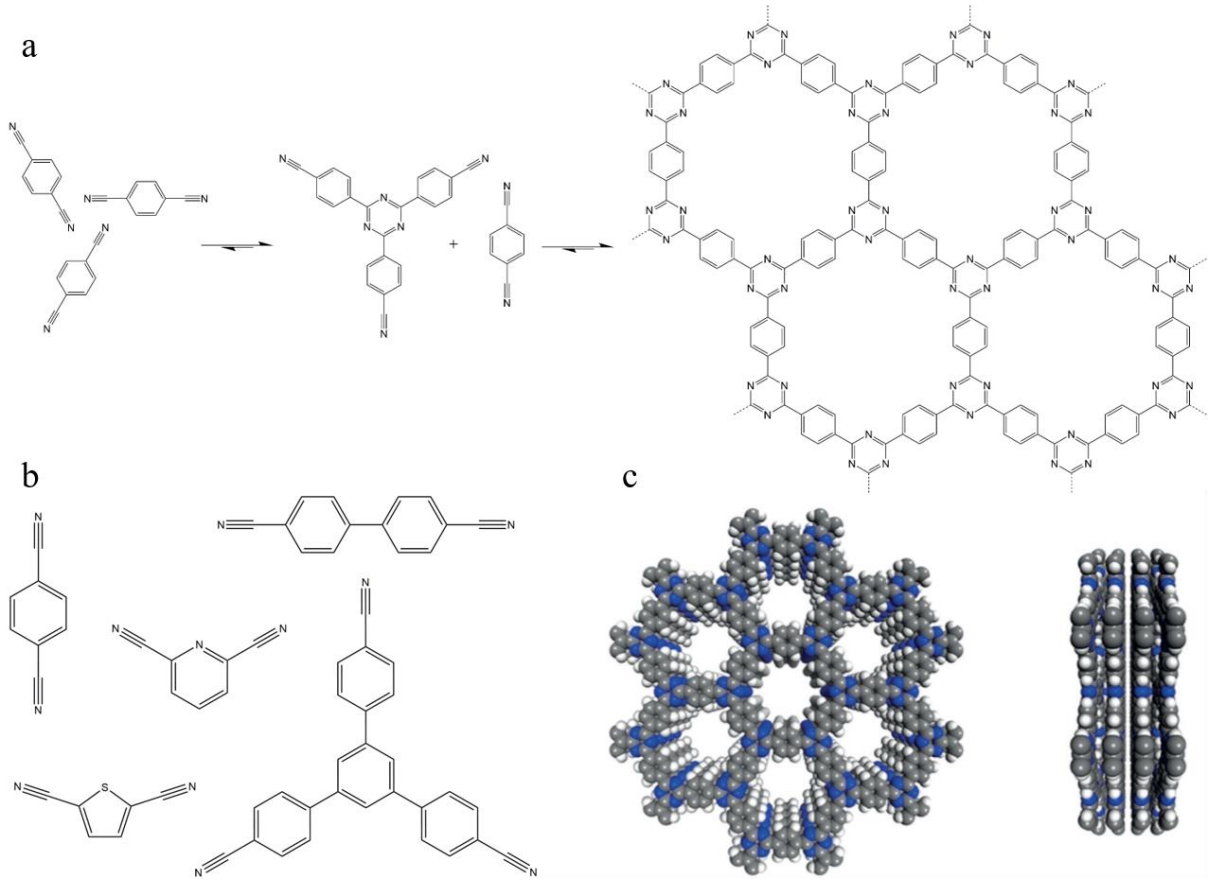

Figure 3. *(*a) CTF-1 synthesis from monomer to bulk structure. (b) A few common monomers for CTF synthesis, all being aromatic molecules with two cyano groups. (c) 3D rendering of CTF-1 with in and out of plane views.[7]

addition to these properties, CTFs are moderately conductive, have high surface area, and tunable porosity.

The CTF's properties allow for its use in various applications. Similar to other COFs, it has been used in gas adsorption and pollution removal.[5] However, due to the high intrinsic amount of nitrogen and conductivity CTFs have also been in catalysis. Chelating metals like platinum or palladium to the CTF structure has produced novel homogeneous catalysis for oxygen reduction and glycol oxidation respectively.[10,11] CTFs have also been used in energy storage applications.[12] Hao et al. are responsible for the first attempt at using CTFs in supercpacitors.[13] Here, the group enhanced the conductivity and porosity of the CTF by increasing the reaction temperature. These are all examples of why CTFs are an excellent candidate for energy storage applications, and why we explored them further.

1.3 Hierarchical Porous Materials

Porous materials are substances that have a large fraction of their volume as void space.[14] Pores can be classified into different size regime; the largest are macropores which have diameters of > 50 nm, followed by mesopores from 2 – 50 nm, and finally micropores with the smallest diameters of < 2 nm (Figure 4).[14–16] When these pore types are combined, the material is said to be hierarchically porous.

The synthesis of hierarchical pores can be accomplished through a variety of methods including soft/hard templating, sol-gel processing, and chemical etching.[14] Hierarchical pores give materials unique properties as compared to a monodispersed pore size. Large pores afford the material with high ion mobility while small pores increase the surface area and active site density. When used as a scaffold for other active materials (nanoparticles, battery materials, catalysts, etc.),

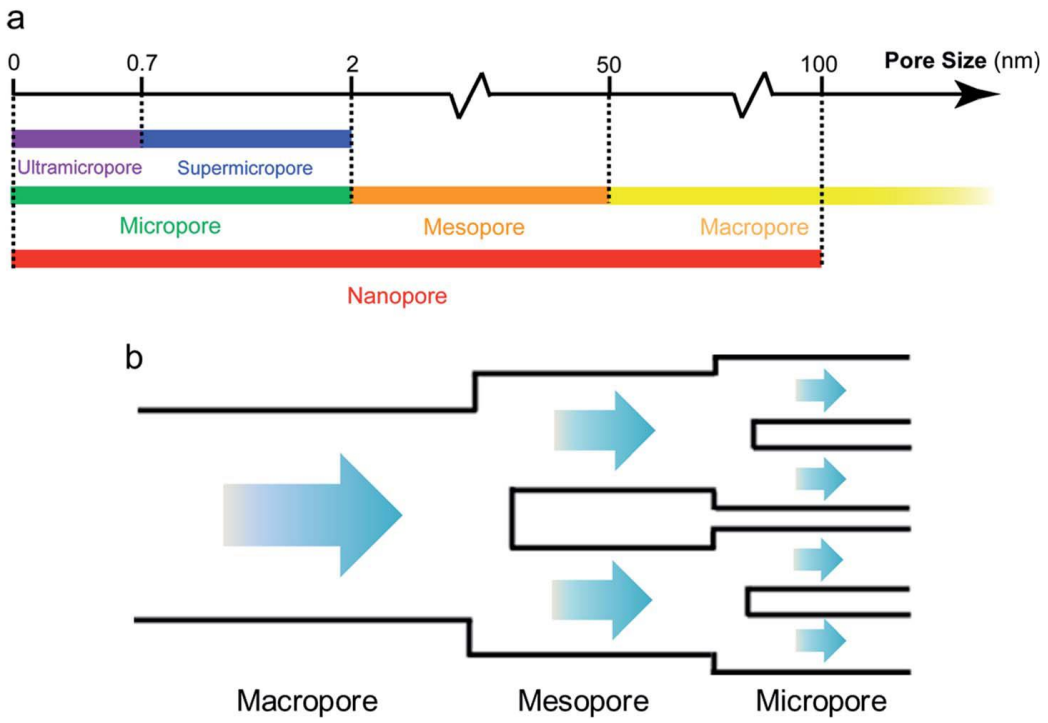

Figure 4. (a) Pore size classification. (b) Hierarchical pores have multiple types, where ions diffuse from largest to smallest pores.[16]

conductive hierarchical porous structures can afford excellent charge transfer to fully utilize novel high performance materials.[15] In this work, we rely on the bottom up synthesis conditions to yield hierarchical porous materials for finer control over the materials pore size distribution.

Hierarchical pores have many uses in various applications that are advantageous over other porous systems with a narrow pore size distribution. Heterogeneous catalysis is a field where reactant and product diffusion in and out of the electrode is a determining factor in the performance of the material. Hierarchical pores enhance mass diffusion, especially of bulky molecules, allowing for increased performance over other traditional heterogeneous catalysts.[17] In addition to catalysis, energy storage is a field that benefits from hierarchical porous materials. Electrolyte must flow in and out of an electrode is all different types of energy storage devices. Hierarchical pores impart enhanced mass transfer throughout the electrode increasing the cycling rates achievable by the devices.

One of the main (and often overlooked) features across all applications of hierarchical porous materials is the ability to fabricate high mass loading electrodes.[15] Mass loading is simply the amount of material loaded in a device per unit area. In order for new materials to be considered for industrial/commercial applications the loading of the material must be a significant volume/weight of the overall device. There are many inert component of a device (current collector, casing, electrolyte) that do not contribute to output, which lower the overall performance of the device as whole (dividing output by total weight of all components). Thus, the material loading should be as high as possible to account for inert components, with realistic values close to current commercial loading amounts > 10 mg/cm^2.[18] Normally, research efforts focus on achieving the highest performance values attainable for a given material (capacity for batteries, turnover number for catalysis, power density for supercapacitors, ect.). In order to stay competitive, the mass loading of the active material is kept extremely low (0.5 – 1 mg/cm^2). By loading a small amount of material, mass and charge transport effects are limited. However, once the loading of the active material is increased, transport effects begin to severely limit performance.[18] Hierarchical porous materials attempt to solve this fundamental challenge by allowing for enhanced transport both ionically and electrically. In one example, loadings of over 10 mg/cm^2 were achieved with only a 12% reduction in performance as compared to a 1 mg/cm^2 loading when the system was nanostructured to have hierarchical pores.[19]

In this work, we develop a method for synthesizing materials with tunable hierarchical pores. With the ability to control the pore size of the material, optimal pore size distributions can be found to suite various applications using the same material and synthesis methods.

1.4 Supercapacitors

Supercapacitors are energy storage devices that can deliver a large amount of charge in a small amount of time, otherwise known as having high power. Compared to conventional capacitors, supercapacitors are able to store up to 10 – 100 times more charge per unit volume.[1,20] They also have extremely long cycle, achieving over 10,000 cycles with little to no degradation. These properties make supercapacitors ideal for applications that require large bursts of energy like regenerative braking, electronic vehicles, lasers, computer components, and more.

Supercapacitor is a general term which includes three classifications differentiated by how each stores charge; electric double layer capacitors, psuedocapacitors, and hybrid capacitors. The most common, and focus of this work, is the electric double layer capacitor (EDLC). The charge storage process is non-faradaic, meaning ions can adsorb and desorb with relative ease. This is why EDLCs are able to cycle so efficiently and quickly. During charging, ions are adsorbed to the surface of the active material building up charge. Upon discharge the ions desorb producing a current opposite of the original charging current (Figure 5). The most common material for EDLCs are high surface area, porous carbons.[20]

Psuedocapacitors store charge via fast surface based faradaic reactions. Upon charging, reduction and oxidation occurs at the surface of the active material. When discharging these reactions proceed in reverse. These materials can cycle faster than batteries due to the quick surface based reactions, however their cycle lives are not as robust as EDLCs. Common materials for pseudocapacitance include various metal oxide like MnO_2 and RuO_2.[21]

Hybrid capacitors utilize mechanisms from both EDLCs, psuedocapacitors, or batteries to achieve the best of both devices. Usually, hybrid supercapacitors are comprised of asymmetric

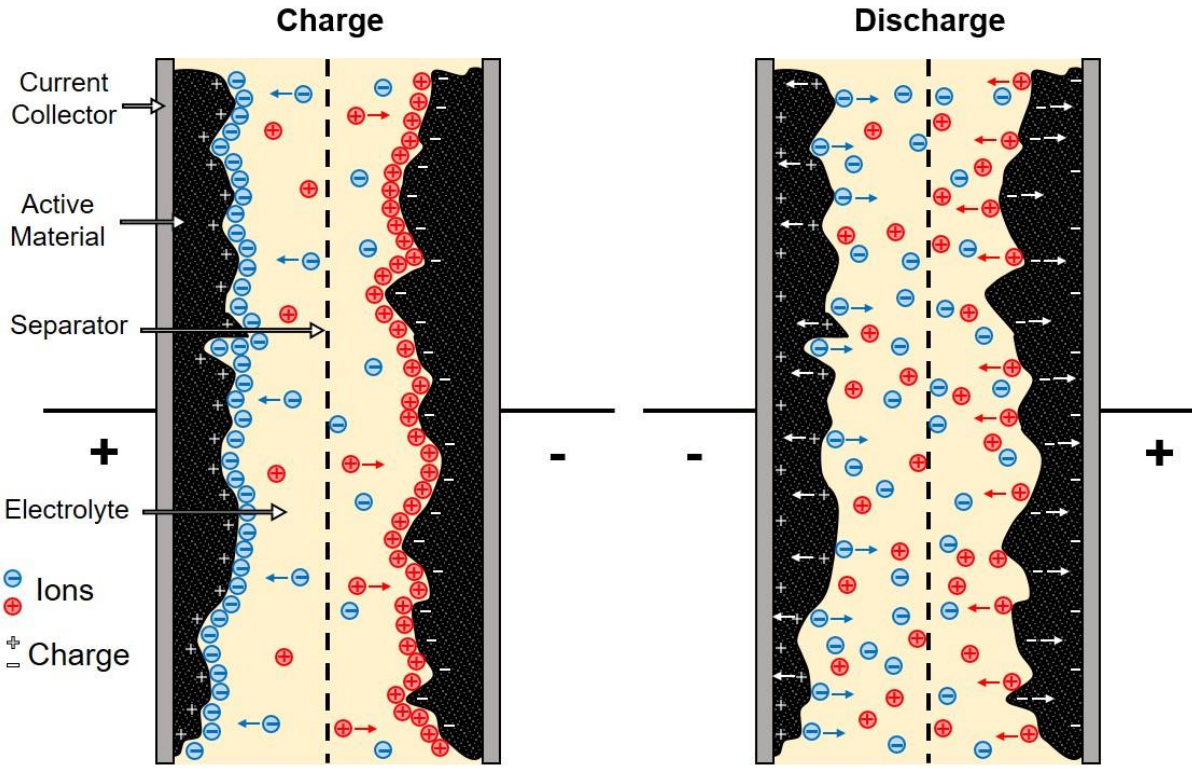

Figure 5. General schematic and operating principle of a symmetric electric double layer capacitor. When in the charged state ions are adsorbed to the surface of opposite charge, held by electrostatic interactions. Once discharged, the ions desorb allowing for the retrieval of stored charge.

electrodes containing an EDLC material and a slower faradaic controlled material.[22] This allows for both high energy and power to be achieved in a single device.

A summary of the properties of different supercapacitor morphology can be found in Table 1as well as the electrolyte properties in **Table 2**. It can be seen that the pore morphology as well as the electrolyte play vital roles in the resulting supercapacitor properties. In this work we focus on developing hierarchical porous electrodes to attain both high rates as well as high loadings.

1.4.1 The Electric Double Layer

In traditional capacitors two parallel plates are separated by a dielectric material. The accumulated charge on the surface of the electrodes can be calculated as the capacitance, C, and is given by Equation 1,

$$C = \varepsilon \frac{A}{d} \quad (1)$$

where ε is the dielectric constant of the interlayer, A is the surface area, and d is the distance between the plates. A supercapacitor has a similar mechanism with some key differences. The dielectric is the electrolyte used and the area is much, much large (1000 – 2500 m^2/g). In addition, the distance separating the charged layers is the electric double layer which is atomically thin, making d in Equation 1 very small. Coupled with high surface areas of electrodes (A in Equation 1), the resulting capacitance is orders of magnitude larger than conventional capacitors.

The operating mechanism behind EDLCs high power is the electric double layer effect. This effect occurs when a charged electrode is placed in an electrolyte. The electrolyte ions will adsorb to the electrode surface in order to achieve charge balance. This mechanism can be described by several models including the Helmholtz, Gouy-Chapman, and Stern models (Figure 6). In each, Ψ_0 is the electrode potential and Ψ is the potential between the layers.

In the Helmholtz model, a charged electronic conductor is balanced by a rigid layer of oppositely charged ions at a distance *d* from the surface (Figure 6a). This model is the most simplistic and is very similar to a parallel plate capacitor. It approximates the potential between the layers drops abruptly after the first adsorbed layer. It neglects interactions of solvation spheres as well as electrolyte concentration.[23]

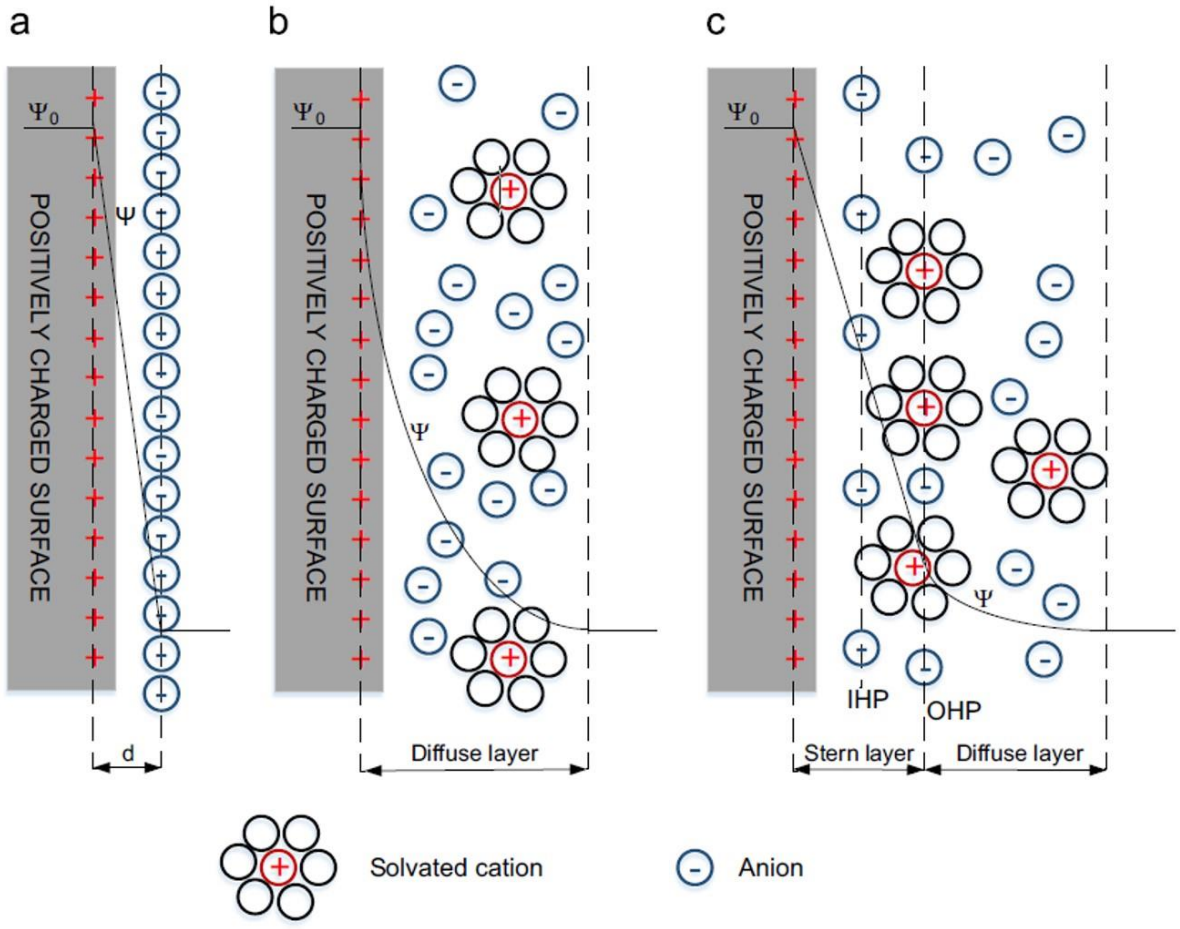

Figure 6. The electric double layer as described in the (a) Helmholtz model, (b) Gouy-Chapman model, (c) Stern Model. In these models Ψ_0 is the electrode potential and Ψ is the potential between the layers.[23]

The Gouy-Chapman model improves on the Helmholtz model. Here, the ions are considered labile on the surface (Figure 6b). It also takes into account ions diffusing into the liquid layer and the kinetic energy of the ions in solution.[23] In this model the potential across the layer decreases exponentially as the distance from the surface increases, due to the ion concentration at the surface following a Boltzmann distribution.

The most complete model of the electric double layer is the Stern model. Here, the electrolyte solution is thought to be made up of multiple layers (Figure 6c). The first layer, or inner layer, is comprised of unsolvated ions located closest to a charge solid surface. The layer of

specifically adsorbed ions is referred to as the "inner Helmholtz plane" (IHP). The next set of non-specifically adsorbed solvated ions in the next layer out is referred to as the "outer Helmholtz plane". Together, the IHP and OHP make up the Stern Layer. Outside of the Stern Layer lies the diffuse layer, where the ion concentration drops exponentially similar to the Gouy-Chapman model. The Stern model can be thought of as combining the Helmholtz model of a tightly bound inner layer with the diffuse layer of the Gouy-Chapman layer.[24]

1.4.2 The Supercapacitor as a Device

Some of the most important properties of a supercapacitor device are the specific capacitance, energy density, and power density. Specific capacitance is a value used to measure the total charge per unit weight held by an active material, and can be directly compared with others to gauge the competitiveness of a material. The specific capacitance of a symmetric device can be calculated from the galvanostatic charge-discharge (GCD) using Equation 2,

$$C_g = 2\frac{I\Delta t}{m\Delta V} \qquad 2$$

where I is the current, Δt is the discharge time, m is the mass of a single electrode, and ΔV is the voltage window the electrolyte. Energy density and power density are also important properties that can be used to compare different active materials. Energy density is given by Equation 3,

$$E = \frac{1}{2}C_g V^2 \qquad 3$$

And Power density is given by Equation 4.

$$P = \frac{E}{\Delta t} \qquad 4$$

The device components of a supercapacitor include quite a few components as seen in Figure 5. Each device contains two electrodes which can be either identical in the case of a symmetric cell or different in the case of an asymmetric cell. A symmetric cell can be thought of as two capacitors in series. This means that in order to calculate the active materials capacitor one must use Equation 5,

$$\frac{1}{C_T} = \frac{1}{C_1} + \frac{1}{C_2} \qquad 5$$

where C_T is the total capacitance and C_1 and C_2 are each electrode. Because C_1 and C_2 are the same, the total capacitance of the device is only half of each electrode. This is why a factor of 2 is included in the capacitance calculation (Equation 2). The electrodes are coated on current collectors, which are usually any material that is both corrosive resistant and conductive to act as a substrate to hold the active material. These electrodes are separated by a thin membrane called a separator, which is electrically insulating and ionically conductive. The entire device is saturated in electrolyte which can vary depending on the desired application.

The most common active materials for EDLCs are activated carbons. Activated carbons are high surface area, low cost carbons derived from various carbon rich organic precursors.[23] Carbons are activated by heating them at high temperatures (600 – 1000 °C) in inert atmosphere in the presence of oxidative compounds like KOH or NaOH. This process controllably oxidizes the carbon sources producing porous networks with high surface areas normally falling between 1000 – 2500 m^2/g.[25] Other active materials for supercapacitors include graphene, conductive polymers, and other conductive high surface area material summarized in Table 1. Each different

Table 1. Summary of various materials for EDLC materials with synthesis methods included.[23,25]

Active Material	Synthesis Method	Surface Area (m^2/g)	Pore Size (nm)	Specific Capacity (F/g)
Mesoporous Carbon	Pyrolysis of polymers	953	2-4	185
N-Doped Graphene-like Carbon sheets	Hard Template	1277	2-30	261
Carbon Nanofibers	Solution Growth	1725	1.1	280
N-Doped Mesoporous Carbon	Templating	200	13-14	167
CNT/graphite nanofiber nanocomposite	CVD	1863	2-5	270
Holey Graphene	Hydrothermal	1560	1-12	298
TaPa-Py Covalent Organic Framework	Solvothermal	687	1.5	209

active material has varying surface areas and pore size distributions in order to optimize the device. However, there is no straightforward variable to maximize in order to obtain a high performance material. Even if the surface area is record high, if the porous network is not accessible to the ions it won't be a good supercapacitor. This is why there is such a large library of supercapacitor materials that have a wide variety of surface areas, pore size distributions, and synthesis methods. Since supercapacitor excel at high power densities, extensive effort has gone into increasing their energy density. However, the active material type is not the only factor that dictates supercapacitor performance.

Electrolytes are the other main contributing factor to supercapacitor performance. There are three main electrolytes used in supercapacitors; aqueous, organic, and ionic liquids. A summary of these electrolytes can be found in Table 2. Aqueous electrolytes have the highest power density due to the high mobility of ions in water.[26] However, the voltage window is limited because above 1.23 V the solvent, water, begins to degrade and water splitting begins. This hard

Table 2. Summary of the most common electrolytes used for supercapacitor applications. The mobility and max voltage of the electrolytes play vital roles in power and energy density, respectively.[24,26,28]

	Electrolyte	Max Voltage (V)	Conductivity (mS/cm)
Aqueous	H_2SO_4	0.8 – 1.2	750
	KOH	0.6 – 1	540
	Na_2SO_4	0.8 – 1.6	91.1
Organic	$TEABF_4$/ACN	2.5 – 3	55
	$TEABF_4$/PC	2.5 – 3	13
	EC-DMC $LiPF_6$	3 – 4	11.8
Ionic Liquid	EMI-BF_4	3 – 4	12
	EMI-TFSI	3 – 4	8.4
	PYR_{14}-TFSI	2.5 – 3.5	2.6

limit has been overcome by utilizing novel electrolytes like Na_2SO_4 which actively suppress the water splitting reaction affording voltage windows up to 1.6 V, greatly enhancing energy density.[27]

Organic electrolytes are a feasible alternative to aqueous electrolytes. The main reason organic electrolytes are used is because of the large voltage window when compared to an aqueous electrolyte. Many organic electrolytes can handle voltages of 3 V before degrading. Energy density is proportional to voltage squared (Equation 3), meaning organic electrolyte have a distinct advantage in energy density, even if their capacities and ion mobilities are lower in comparison to other electrolytes.[28] One other disadvantage to organic electrolytes is their safety. Organic electrolytes are typically flammable raising safety concerns.

Ionic liquids are the final type of supercapacitor electrolyte. Ionic liquids are salts that are liquid at relatively low temperatures (< 100 °C). Usually, the cation is a large organic molecule commonly using imidazoliums, pyrrolidiniums, or tetraalkylammoniums. Normally, bulky anions

like PF_6^-, BF_4^-, or TFSI are used as countercharges. When paired together, crystallization is limited because of the weak bonds between the ions. This effectively gives a solation of ions without any solvent. Due to the large ion size, ionic liquids are typically some of the least mobile electrolytes. However, they have some of the highest voltage windows, with some reaching up to 6 V.[29] They are also nonflammable alleviating the safety concerns of organic electrolytes.

In this work, we utilize the ionic liquid [EMIM][BF_4]. Coupled with our hierarchical porous carbon, we aimed to increase the mobility of the ionic liquid to provide high power to an already high energy electrolyte.

1.5 Chemical Modification of Graphene

Graphene is a 2D allotrope of carbon with remarkable properties including high strength, conductivity, and flexibility.[30,31] It can be synthesized in a variety of ways including mechanical exfoliation, chemical vapor deposition (CVD), oxidation of graphite, and thermal decomposition.[30,32,33] It has the potential to improve various areas of science that rely on these properties like energy storage, catalysis, and transistor technology. However, it does have limitations like difficulty processing and irreversible agglomeration which prevent its application in many areas. To this end, researchers have probed the chemical modification of graphene to improve these limitations (Figure 7). In addition, the modification of graphene can introduce new properties like enhanced solubility, wettability, or mechanical properties with a wide variety of applications.[30,32,33] These modifications can be either non-covalent or covalent depending on the application.

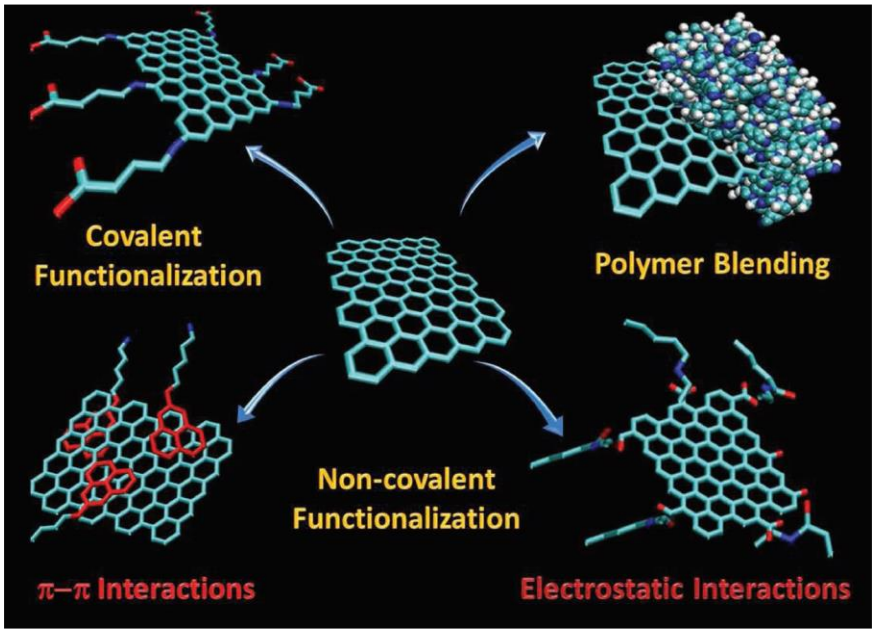

Figure 7. A few depictions of the ways graphene can be modified either covalently or non-covalently.[34]

1.5.1 Non-Covalent Modification of Graphene

There has been tremendous focus on creating composites with graphene to take advantages it's unique properties. Usually, graphene is used as a scaffold for other nanostructured materials like nanoparticles or polymers to create nanocomposites. The non-covalent modification can occur in a multitude a ways ranging from Van der Waals, electrostatic, hydrogen bonding, and π-π stacking interactions.[30,34]

Common non-covalent modifications include introducing surfactants for dispersion stability and polymers for stability. Another very common method of modification is using graphene as a scaffold for various nanostructures. This usually involves synthesizing nanoparticles on graphene to aid in conductivity. This has a huge number of applications ranging from catalysis, electronic devices, and energy storage.

1.5.2 Covalent Modification of Graphene

The covalent modification of graphene involves chemically bonding atoms/molecules to graphene. This does damage the pristine graphene structure, and reduce properties like conductivity, however the gain in desired properties significantly outweighs this loss. Some methods of direct covalent modification of graphene is atomically doping it. Metal doping can be done through high temperature annealing in the presence of a metal salts while nitrogen doping can be achieved though annealing graphene in an ammonia atmosphere.[35]

A more common method for covalent modification of graphene is though reactions with graphene oxide (GO). GO is one of the most well-known chemically modified graphenes. GO is graphene that has been heavily oxidized, and contains a myriad of oxygen containing functional groups like carboxylic acids, hydroxyl, epoxides, and carbonyl groups. The synthesis involves the controlled oxidation of graphite via very strong oxidants. During the synthesis graphite becomes oxygenated and is chemically exfoliated during the process yielding an aqueous solution of graphene oxide.[36] GO is one of the most promising methods for graphene production, as it can be reduced easily to yield reduced graphene oxide (rGO), which has properties similar to graphene with much easier processability.

The oxygen containing functional groups on GO can act as a center for covalent modification. Some reactions include addition, electrophilic/nucleophilic substitutions, condensation reactions. These types of reactions can add various functionalities to GO like amines or amides for increased organic solvent solubility, ferrocene to introduce magnetic effects, and polymers to increase structural stability.[33]

Another more modern approach to producing covalently modified graphene is through reactions with fluorographene. Fluorographene is fluorinated graphene, once thought to be

chemically inert, and has gained recent attention to its rich chemistries available discovered recently.[37] Fluorographene is unique in the fact that it has the potential to have a much higher and more specific degree of functionalization as compared to GO or graphene.

In this work we utilize fluorographite as a starting reagent in an effort to produce triazine functionalized graphene. In addition, we explore the use of rGO to host sulfur in lithium-sulfur batteries in Chapter 6.

1.6 Lithium Sulfur Batteries

Lithium sulfur batteries (LSBs) are a promising new energy storage technology. With a theoretical capacity of 1675 mAh/g, they are an attractive alternative to lithium ion batteries with common active materials like $LiCoO_2$ only achieving theoretical capacities of 274 mAh/g.[38] The operating principle behind the LSB is sulfurs reaction with lithium, seen in the overall reaction in Equation 6.

$$2Li + S \rightarrow Li_2S \qquad 6$$

However, the reaction is more complicated than just the overall net ionic equation. During the reaction lithium reacts with elemental sulfur to form lithium polysulfides beginning at 2.4 V (Figure 8a). These polysulfides begin as high order polysulfides like Li_2S_8 and breakdown as the reaction proceeds to smaller polysulfides like Li_2S_6 and Li_2S_4 occurring around 2.2 V (Figure 8b). Finally, upon completion of the reaction Li_2S is formed as the final discharge product.[39]

Even with its high capacity, lithium sulfur batteries currently have some very large limitations. Lithium sulfur batteries suffer from three major problems. First, the charge and discharge products, elemental sulfur and Li_2S, are intrinsically insulating. During cycling insulating products can build up on the electrode surface blocking electron transfer (Figure 9a &

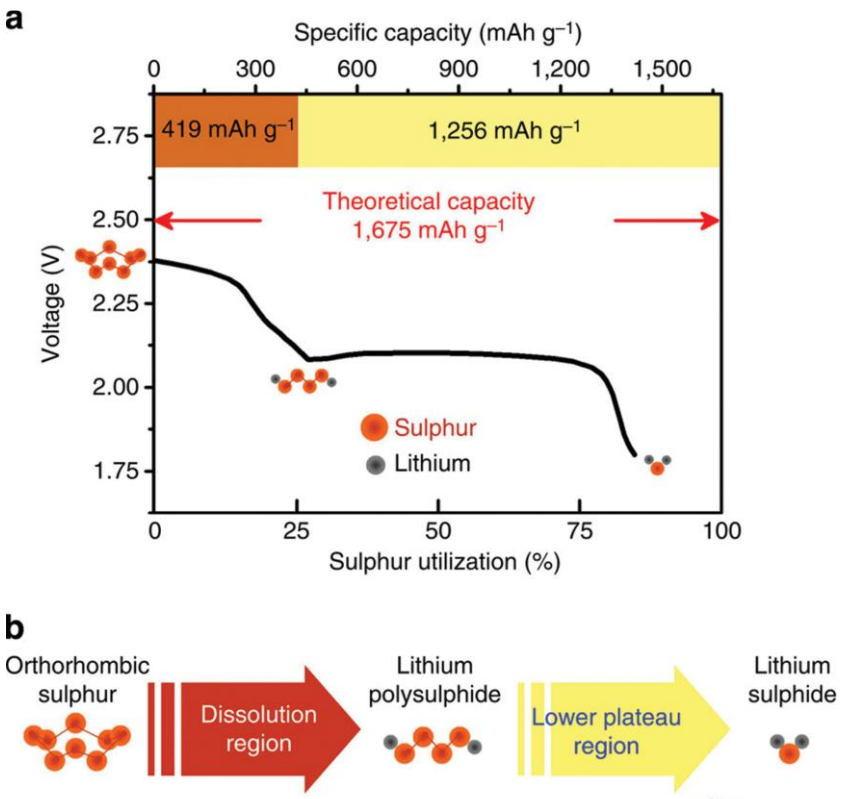

Figure 8. (a) A typical discharge profile of a LSB, with the corresponding voltage plateaus of lithium polysulfide generation and consumption. (b) Corresponding dissolution of polysulfides until they react to form insoluble Li_2S.[44]

b). Second, during charge and discharge there is a large volume expansion of over 80%. This leads to reduced cyclability because active material can lose contact with the current collector and no long cycle. The last issue, and most problematic, is polysulfide shuttling. Polysulfide shuttling occurs during the discharge where soluble intermediates dissolve into the electrolyte. Polysulfides can diffuse away from the electrode causing loss of active material (Figure 9c) as well as detachment from the electrode (Figure 9d). During recharge polysulfides can create an insulating layer on the current collector blocking electron transfer (Figure 9e).[40]

Tremendous effort has gone into solving these three problems. The conductivity problem has been alleviated in multiple ways, however the most common way is to create a composite of sulfur with conductive materials. A few examples include sulfur composites with graphene and

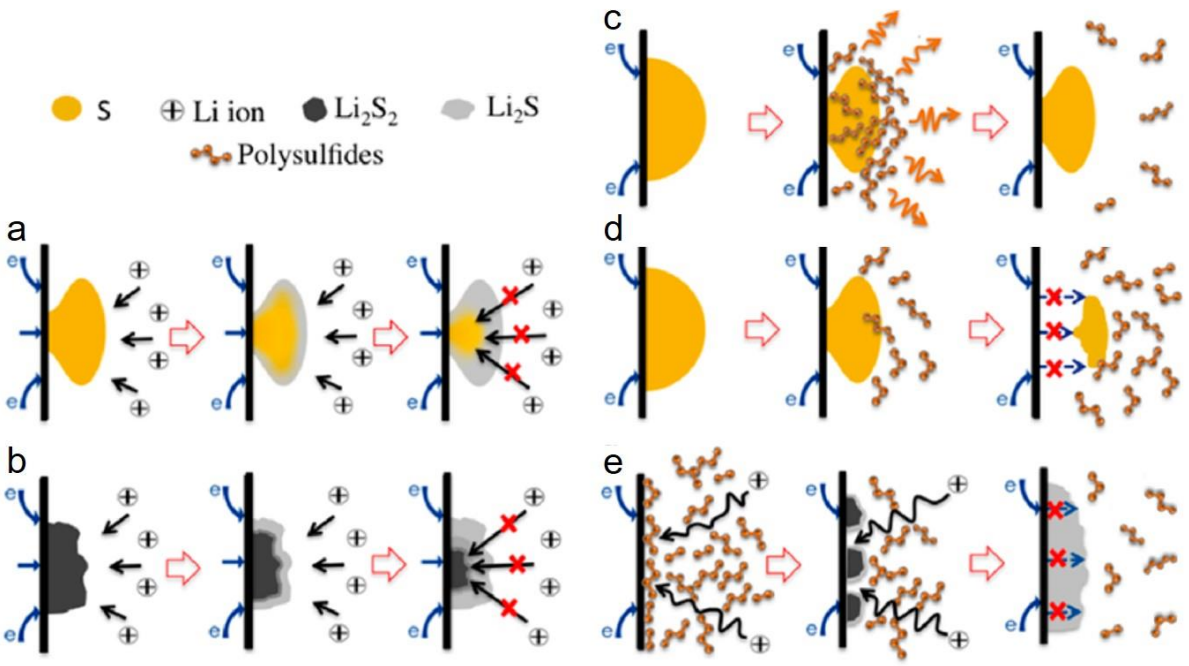

Figure 9. Different lithium sulfur battery degradation mechanisms. (a) Insulating layers of Li_2S can build up on sulfur preventing the full reaction from taking place. (b) Similar to a, thick insulating layers can prevent the full use of active material. (c) Polysulfides can diffuse away from the electrode resulting in a loss of active material. (d) Dissolution of polysulfides can detach active material from the current collector. (e) Layers of Li_2S can build up on the electrode preventing recharge.[40]

other conductive carbons like Super P and KetJen Black.[41] As for volume expansion, flexible scaffolds can be used to accommodate the expansion of the active material. Additionally, yolk shell structures show promise in handling the volume change due to internal void space that allows for the expansion.[42] Polysulfide shutting has been reduced through two main methods; physical encapsulation and chemical adsorption/repulsion. Physical encapsulation methods include using porous materials like activated carbon and conductive polymers.[43,44] Encapsulation methods work well in reducing polysulfide shuttling, however it requires a large percent of material dedicated to polysulfide confinement, reducing the overall active material percent. Chemical adsorption methods include developing highly sulfiphilic materials like N-doped carbon for high adsorption

of polysulfides as well as chemical repulsion methods which include methods like functionalizing separators with charged species to electrostatically repel polysulfides.[45,46]

A newer method recently explored to reduce polysulfide shuttling is the catalysis of the lithium sulfur reactions. First discovered by Yuan et al, CoS_2 nanoparticles were used as catalytic centers to both adsorb polysulfides and enhance polysulfide reactions.[47] In Chapter 6, we explore a method for developing single metal atom catalysis to enhance sulfur reduction reactions in hopes of increasing the cycle life and rate capabilities of lithium sulfur batteries.

CHAPTER 2. TUNING THE POROSITY OF COVALENT TRIAZINE FRAMEWORKS TO CREATE HIERARCHICAL POROUS CARBON

2.1 Introduction

Covalent organic frameworks (COFs) are a unique class of material made from organic monomer units that have high crystallinity, surface area, and pore volume. These are attractive features for electrochemical applications however, most COFs are insulating. Covalent triazine frameworks (CTFs) solve this problem because they contain a conjugated backbone allowing for moderate conductivity.

Pioneered by Kuhn et al., these CTFs contain a triazine motif with high surface area, and are synthesized from cheap, abundant aromatic nitriles.[48,49] The conjugated CTFs fulfill all of the necessary attributes for use in electrochemical applications due to their high surface areas, moderate electrical conductivity, high chemical/physical stability, and tunable geometries.[13,49] By varying the synthesis conditions, the nanostructure of CTFs can be altered. Varying the monomer

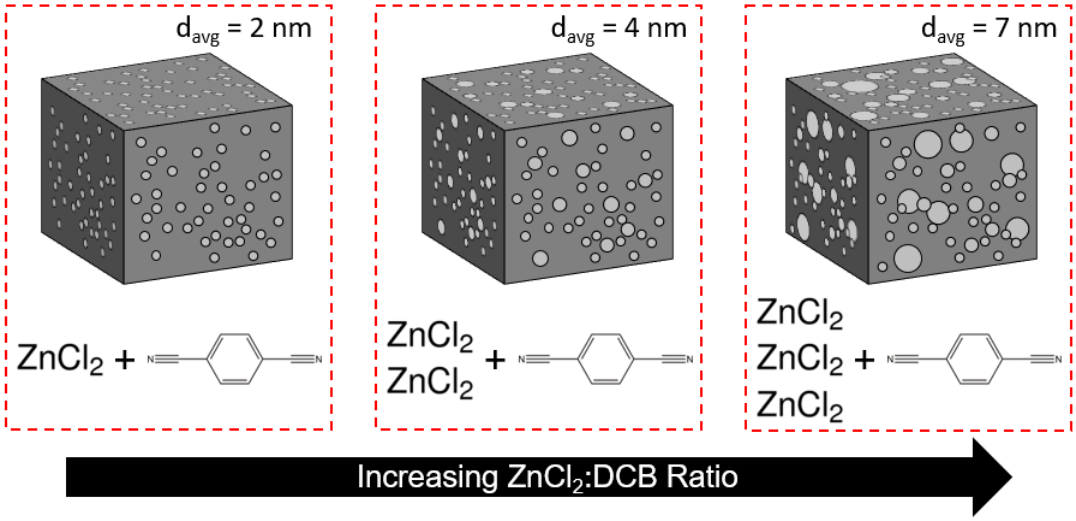

Figure 10. The porosity evolution in the CTF-derived HPCs with varying $ZnCl_2$ to DCB ratios. Small micropores are maintained for high surface area, while larger mesopores are created to ensure efficient ion diffusion throughout the material.

of the CTF has been extensive explored, and has been shown to vary the pore size depending on the monomer used.[7] The temperature has also been shown to increase the mesoporosity in the resulting CTF structure.[13] The generation of mesopores allow for the synthesis of a material with both nano- and mesopores – otherwise known as hierarchical pores. This type of conductive pore system may allow for improved ion transport as well as active material mass loading for electrochemical applications.[15]

Here, we focus on developing tunable hierarchical porous frameworks that contain both micropores and mesopores to allow for efficient ion diffusion while still maintaining a high surface area. This is crucial for many applications ranging from energy storage to catalysis. Hierarchical porous carbon (HPC) with modest nitrogen content (~ 7 – 9 at%) was generated through the high temperature ionothermal synthesis and partial pyrolysis of a CTF in molten $ZnCl_2$. By tailoring the 1,4-dicyanobenzene (DCB) monomer precursor concentration in the $ZnCl_2$ melt, HPCs can be readily produced with widely tunable pore size distributions (Figure 10).

2.2 Experimental

The HPCs were synthesized from the trimerization reaction of 1,4-dicyanobenzene (DCB) in a molten $ZnCl_2$ salt. In a typical synthesis, 400 mg of DCB and the desired weight of $ZnCl_2$ were ground together in a pestle and mortar inside of a glovebox. The resulting mixture was transferred to a quartz ampoule, evacuated, and sealed. The samples were heated to 700 °C in one hour, and reacted for 20 hours. After cooling to room temperature, a large black monolith was obtained, which was ground and then washed with a 0.5 M HCl solution three times, water once, and THF twice. The washed sample was dried in a vacuum oven at 120 °C overnight. The same

method was also used to prepare HPCs using 1,3-dicyanobeznene (mDCB), or 2,6-dicyanopyradine (DCP) monomers for mechanism studies.

The morphology of the samples was studied by scanning electron microscopy (SEM), using a JEOL JSM-6700F FE-SEM at 8 kV. Energy dispersive X-ray (EDAX) spectroscopy was obtained from a METEK Z2e analyzer at 10 kV and a probe current of 15 μA. Transmission electron microscopy (TEM) was performed using a FEI T12 operated at 120 kV.

N_2 adsorption-desorption isotherms were obtained at 77 K using a micromeritics TriStar 3020. Samples were degassed at 175 °C under vacuum overnight before measurements. Surface areas were calculated from Brunauer-Emmett-Teller (BET) theory, and pore size distributions were obtained through density functional theory (DFT).

Raman spectroscopy experiments were performed on the HPCs using a Horiba LabRam HR800 system with an excitation wavelength of 514 nm.

Powder X-ray diffraction (XRD) was performed on a Bruker D8 with Cu Kα x-rays (λ = 0.15418 nm). The step size was 0.014° every 0.18 s operated at 45 V and 10 mA.

2.3 Results & Discussion

The high temperature synthesis of DCB has been proven to increase surface area, porosity, and conductivity of the resulting CTF.[13] By further tuning the reaction conditions, hierarchically porous carbon (HPC) was obtained from the simultaneous synthesis and pyrolysis of the CTF at 700 °C. The DCB to $ZnCl_2$ molar ratio was varied from 1:1 to 1:20 to create the various HPCs (Figure 10). Of the samples obtained with this method, four with significantly different pore size distributions were chosen for characterization and electrochemical studies. From the smallest pore size to the largest, the samples are denoted s, m, L, and XL-HPC, corresponding to HPCs obtained

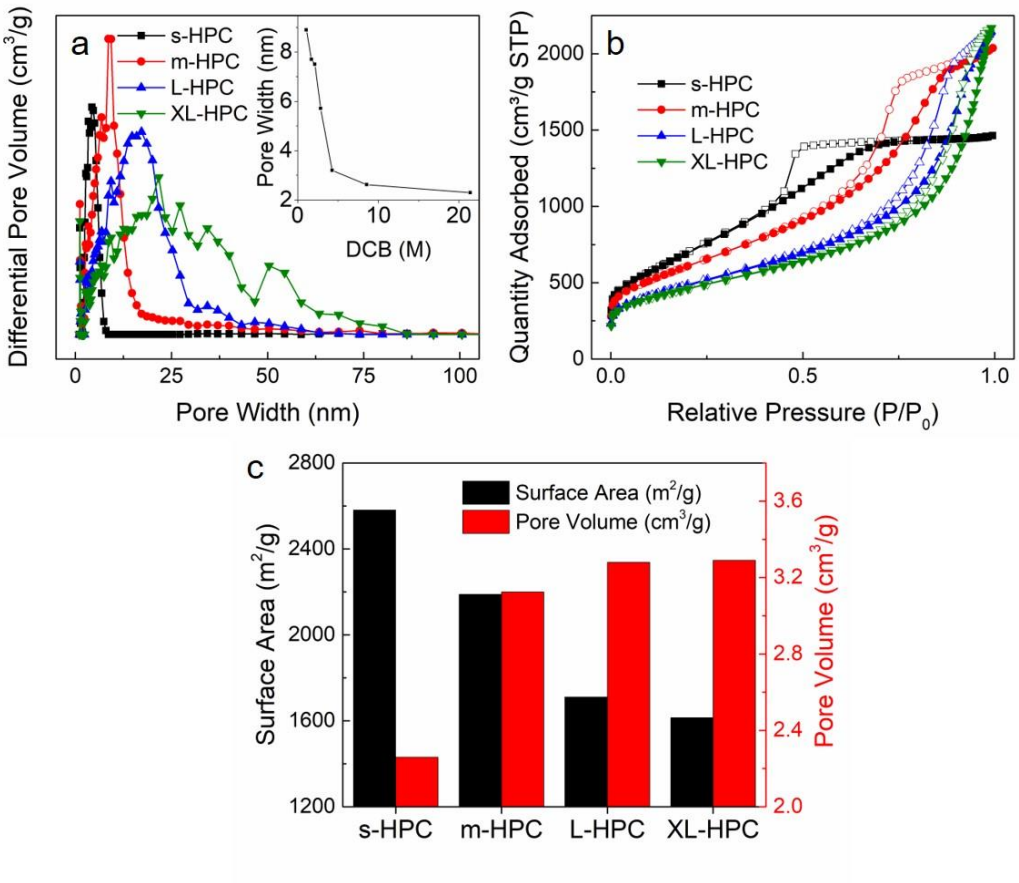

Figure 11. BET isotherm (a) and differential pore volume (b) plots shows hierarchical porosity of the samples prepared with different monomer:$ZnCl_2$ ratios denoted s, m, L, and XL-HPC for increasing pore size distribution. The inset in (b) shows that the average pore size is directly correlated to the concentration of DCB in solution, reaching a minimum at around 2.5 nm. The hysteresis in the isotherm plot is indicative of mesoporous samples. A summary of the surface area and pore size are shown in (c).

with DCB:$ZnCl_2$ ratios of 1:5, 1:7.5, 1:12.5, and 1:20, respectively. N_2 adsorption and desorption isotherms were used to determine the surface characteristics of the HPCs (Figure 11a). The adsorption-desorption curves take the shape of a type IV isotherm, indicating the presence of both micropores and mesopores in each HPC. Furthermore, the hysteresis loop gradually shifts from H2 to H3 type as the ratio of $ZnCl_2$ gets higher (Figure 11a), indicating the change from "ink bottle" pores to slit like pores.[50] This is most likely due to the $ZnCl_2$ acting as a porogen during the synthesis, as also postulated previously.[51,52] The differential pore size distributions for the

series of samples are further shown in Figure 11b. It is apparent that the s-HPC obtained with the DCB:$ZnCl_2$ ratio of 1:5 shows limited hierarchical porosity. With an increasing ratio of $ZnCl_2$, the pores expand dramatically, with an average pore diameter shift from 2.5 nm in s-HPC to almost 10 nm in XL-HPC (Figure 11b). One important aspect of the differential pore volume plots is the preservation of small pores (0.5 – 2 nm) in the structure, which are essential for retaining high surface while hierarchical porosity is being introduced with the increasing $ZnCl_2$ ratio.

SEM images confirm the porosimetry results, showing a gradual shift from small pores to large pores (Figure 12a-d). Comparing the smallest sample, s-HPC (Figure 12a), to the largest, XL-HPC (Figure 12d), one can see the stark difference in the porosities. No large voids are seen

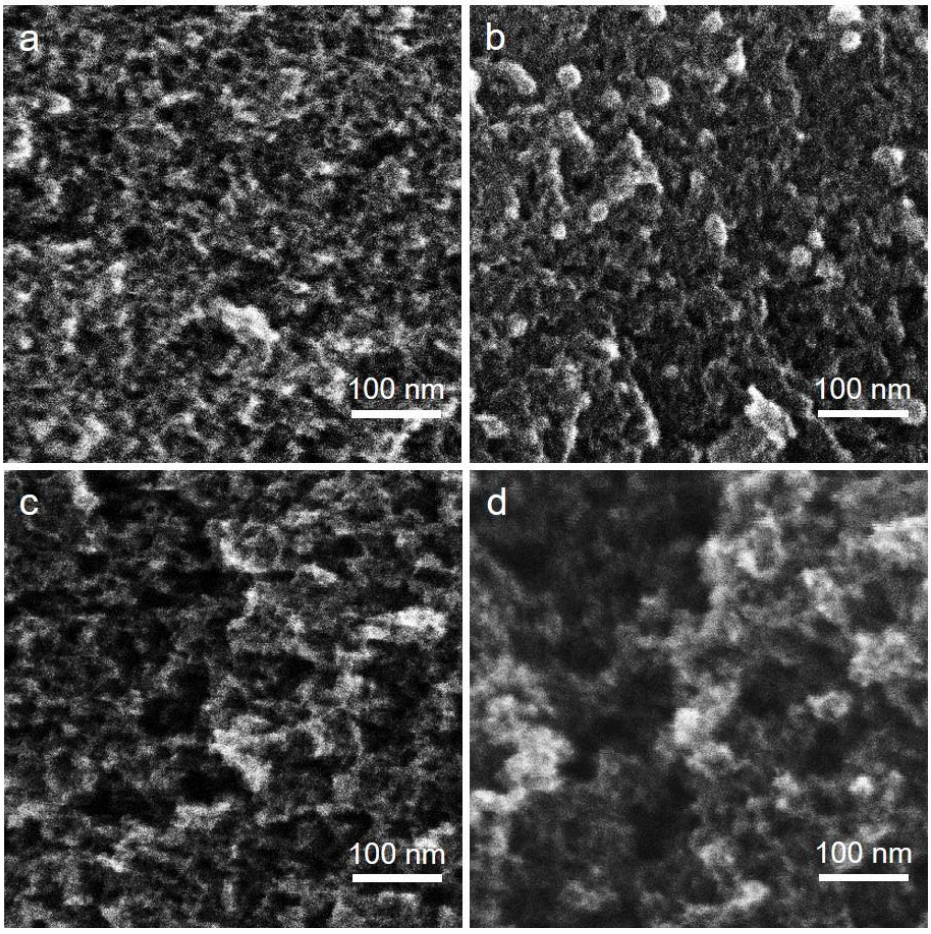

Figure 12. The SEM images of s-HPC (a), m-HPC (b), L-HPC (c), and XL-HPC (d) show an increasing pore size in the resulting HPCs.

in s-HPC and the surface is relatively uniform, confirming the limited hierarchical porosity as shown in the pore size distribution plot. Figure 12d especially demonstrates the hierarchical nature of the larger HPCs. There are large cavernous voids dotted with small pores along the walls. This interconnected network of pores is critical for efficient mass transport and electrolyte penetration to ensure pore accessibility. TEM studies also confirm a similar evolution of the porous structures in these different samples (Figure 13). It is noted that the larger pore size comes at a cost of surface area. The s-HPC has a surface area of 2581 m^2/g, while the XL-HPC has a ~ 40% reduction in surface area to 1614 m^2/g.

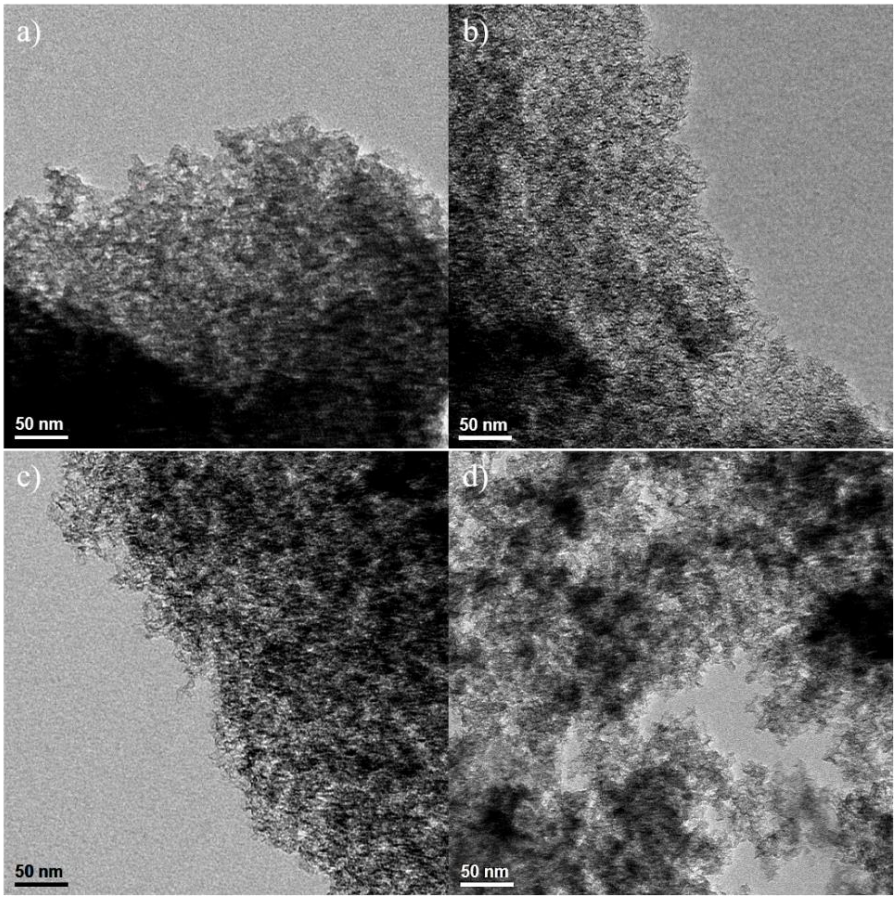

Figure 13. TEM imaging of (a) s-HPC, (b) m-HPC, (c) L-HPC, (d) XL-HPC.

Raman spectroscopy was used to characterize the HPCs. The main peaks of interest are the D-peak (1360 cm^{-1}) which arises from sp^2 hybridized carbon's breathing mode and G-peak (1560 cm^{-1}) is due to the bond stretching of all sp^2 hybridized carbon.[53,54] These can be used to approximate the degree of sp^2 and sp^3 carbon in a sample.[54,55] Carbon samples that are highly graphitized have a low I_D/I_G ratio, while amorphous carbons have a much higher I_D/I_G ratio (ranging from 0.8 – 1.5). Figure 14a shows the contrast between graphite with a low I_D/I_G ratio, and CTFs synthesized at different temperatures. The 400 °C CTF (referred to as CTF-1 in literature) has been shown to stack similar to graphite but with limited periodicity.[48] This leads to an increased I_D/I_G ratio as compared to graphite. The 700 °C sample exhibits an even higher ratio, indicating the structure lacks periodicity, and is mainly amorphous. Figure 14b shows that the HPCs with different pore size each have an I_D/I_G ratio of around 1, which is consistent with other amorphous carbons.[54,56–58] The similar ratios indicate that each sample has roughly the same degree of amorphous character, suggesting that the amount of $ZnCl_2$ did not significantly affect the pyrolysis.

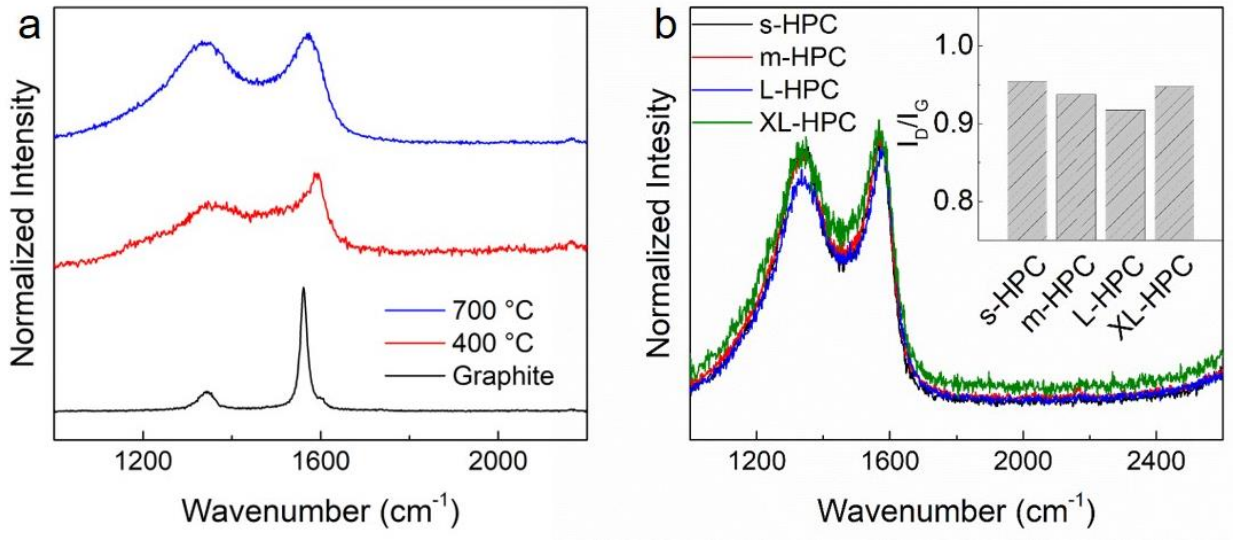

Figure 14. Raman spectra of the high temperature synthesis shows an I_D/I_G ratio of around 1, which is consistent for amorphous carbon (a). Each HPC has a I_D/I_G ratio of around 1 (b), meaning $ZnCl_2$ did not enhance pyrolysis, but acted as a porogen.

The XRD patterns provide further evidence of the amorphous nature of the HPCs. Comparing CTF-1 to the higher temperature displays the difference in structure. As stated previously, CTF-1 has a layered structure that lacks long range periodicity. This broadens the (001) stacking XRD peak at around 26°, as seen in Figure 15.[7] The (001) stacking peak disappeared during the higher temperature synthesis at both low and high $ZnCl_2$ concentrations, which may be attributed to N crosslinking throughout the structure.[13,49]

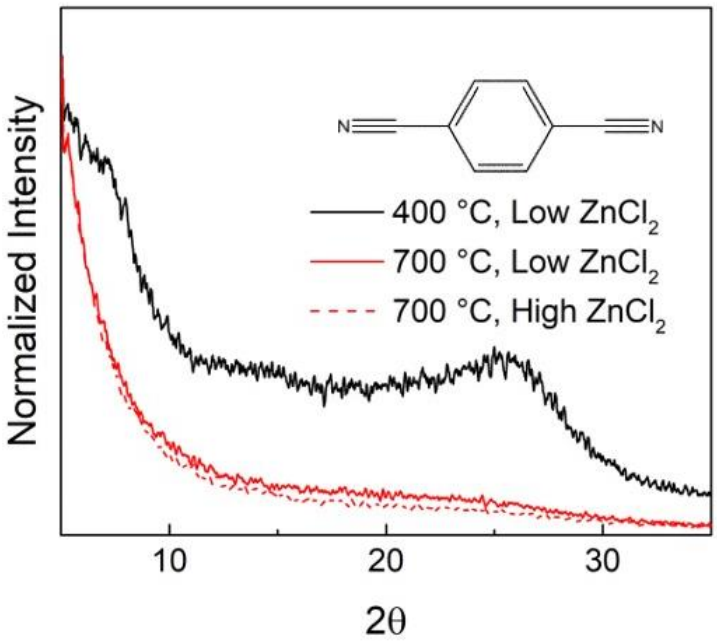

Figure 15. XRD of DCB indicates no graphitization of the sample, and that it is mostly amorphous, losing any periodicity

To probe whether or not the monomer geometry affected the resulting porosity, we have explored two other monomer units for the synthesis under the same reaction conditions. DCB and its meta isomer, mDCB, showed similar behavior at low and high $ZnCl_2$ amounts (Figure 16). The differential pore volume plots show that at high $ZnCl_2$ amounts hierarchical porosity is introduced. In contrast, the pyridine containing monomer DCP showed no such pore expansion. The low and high ratio samples had identical pore size distributions. The solvent-solute interaction is suspected

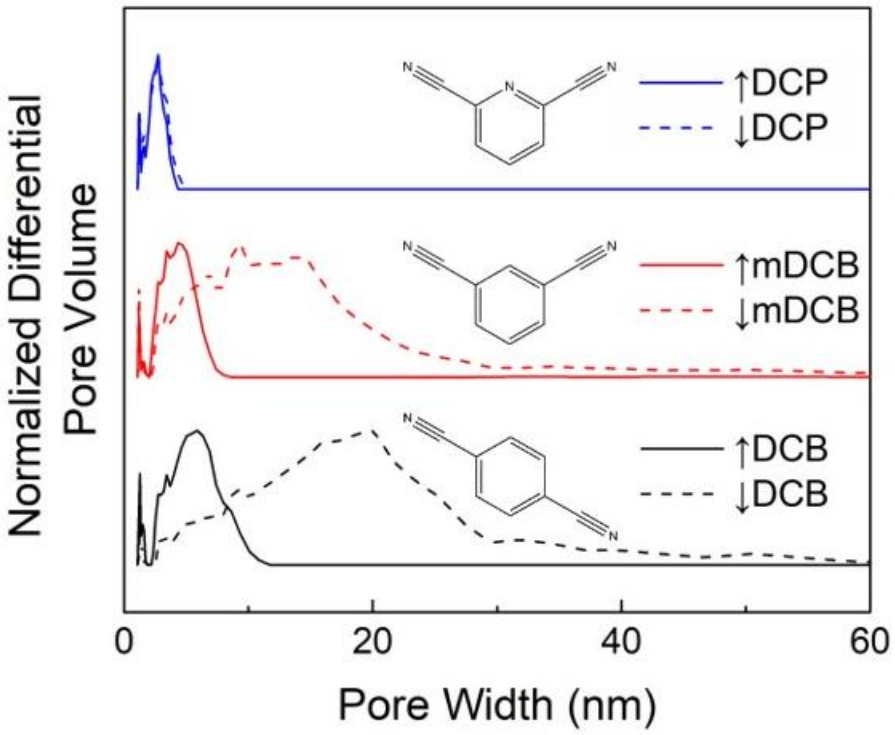

Figure 16. The differential pore volume is dictated not only by the $ZnCl_2$ content, but also the monomer used. Both mDCB (red) and DCB (black) show expanded pore sizes at high monomer:$ZnCl_2$ ratios, while DCP (blue) is unchanged.

to be stronger for DCP than mDCB and DCB due to the presence of a pyridine. This stronger interaction may prevent the $ZnCl_2$ from creating mesopores in the structure because it is "locked" in place inside the CTF structure.[49] The weaker interaction with DCB and mDCB may allow for free $ZnCl_2$ to occupy a large volume between growing CTF sheets giving rise to hierarchical porosity. This further suggests that $ZnCl_2$ is acting as a porogen in the HPC system rather than enhancing pyrolysis of the overall structure. EDAX analysis supports this conclusion because each HPC contains a similar nitrogen amount of 8 – 10 wt% (Table 3). If $ZnCl_2$ promoted hierarchical porosity through pyrolysis there would be a defined loss in N content with increasing $ZnCl_2$ amount.

Table 3. EDX values for carbon and nitrogen for each HPC

Element	s-HPC	m-HPC	L-HPC	XL-HPC
C wt%	91.9	90.8	91.3	89.9
N wt%	8.2	9.2	8.7	10.1
C at%	92.9	92.0	92.5	91.2
N at%	7.1	8.0	7.5	8.8

This combined evidence suggests that the hierarchical porosity results from porogen effects rather than degradation. It is crucial to understand these interactions, because some monomers will not produce hierarchical porosity. To enhance nitrogen content, different monomers with weaker solvent-solute interactions should be chosen, particularly ones lacking a pyridine motif.

2.4 Conclusion

Hierarchical porous carbon with high nitrogen content, derived from covalent triazine frameworks, was explored in this study. Unique pore structures were synthesized, with various levels of porosity; termed small, medium, large, and extra-large. The pore sizes ranged from dramatically with the smallest having an average pore size of 2.5 nm and the largest with an average pore size of 10 nm, containing some pores with diameters of over 50 nm. It was found that the solvent, molten $ZnCl_2$, was responsible for introducing mesoporosity into the sample by acting as a porogen. Weak intermolecular forces between the solvent and solute allow the $ZnCl_2$ to occupy large volumes in-between growing CTF layers during the high temperature synthesis. This leads to large amounts of $ZnCl_2$ producing successively larger pores. This can be disrupted by stronger bonding motifs like pyridines, which prohibit mesopores formation. HPCs contained a high

nitrogen content, even at the high synthesis temperature of 700 °C, with each containing around 9 wt%.

CHAPTER 3: HIERARCHICAL POROUS CARBON AS ACTIVE MATERIAL FOR HIGH MASS LOADING SUPERCAPACITORS

3.1 Introduction

Energy storage is becoming more important than ever as the world's demand for portable energy rapidly increases. Many electronic devices require components that can handle large power spikes, with fast charge and discharge rates (seconds to minutes) like electric vehicles, laptops, and backup power generators.[24,59] Electric double layer capacitors (EDLCs) are attractive for fulfilling such technological needs, through their exceptional power densities and robust cyclability.[24]

These unique high power characteristics of EDLCs are attributed to their fundamental operating mechanism – the electrical double layer effect. Capacitance originates from the separation and absorption of charged ions on the surface of the electrodes.[24,58–60] This process is non-faradaic and only limited by electrolyte diffusion in the electrode, which promises very high charge and discharge rates with unrivaled stability, but often with a limited capacity due to the nature of surface ion absorption. The capacity of EDLCs is directly tied to the surface area of the electrode. In this regard, carbonaceous materials are particularly attractive for their high surface areas as well as excellent electrochemical stability.[20,24] In particular, nanostructured carbon materials have shown great potential for boosting the capacities of supercapacitor electrodes. For example, microporous carbon electrodes have shown high capacities of over 250 F/g at high rates.[20,24] However, the areal mass loading of the electrodes is often overlooked, and is typically very small (0.5 – 1.0 mg/cm^2). In this case, if one takes the mass of the entire device into consideration (casing, current collector, separator, etc.), the overall capacity of the devices with

such low mass loadings is seriously compromised. Realistic loadings of the active materials with a total mass comparable to that of the current collector (~ 10 mg/cm^2) are necessary for practical applications. However, the performance of many supercapacitor materials reported to date drops quickly as the electrodes become thicker at higher mass loading. This is due to many factors, such as increased internal resistance of the electrode and poor ion diffusion through thicker electrodes.[61] Developing nano-architectured materials to maintain their outstanding performance at practical mass loadings is crucial for the development and application of high performance supercapacitors.

A good candidate for supercapacitor active materials are covalent organic frameworks (COFs). They feature several desirable characteristics of a supercapacitor material, including high surface areas, tunable porosities, and diverse functional groups.[4,62] However, typical COFs lack high electrical conductivity, which is essential for EDLC function. Solutions to this problem are mostly achieved through pyrolysis/carbonization of the COF[57,63] or synthesizing the COF in the presence of a conductive host material[64]. Another potential way to enhance conductivity is to use conjugated monomers.[13,65,66] To this end, covalent triazine framework (CTF) represents a unique class of COFs with a fully conjugated structure. Additionally, the rich nitrogen groups in CTFs may also be beneficial to EDLCs through enhanced wettability of the electrolyte, introduction of pseudocapacity (aqueous electrolytes), and increased active surface area.[56] Hao et al. first reported CTFs for supercapacitor applications by using a high nitrogen content monomer unit and a high temperature synthesis to generate a mesoporous framework with desirable high surface area and conductivity.[13]

Previously, we have developed hierarchical porous carbon derived from covalent triazine frameworks with tunable pore sizes described in chapter 2. These materials are used in EDLC's to create high loading supercapacitors with exceptional performance. We show a decreasing

DCB:$ZnCl_2$ ratio gives rise to larger mesopores, with improved pore connectivity and accessibility that is beneficial to mass transport and ion diffusion for high performance electric double layer capacitors (EDLCs) at high mass loadings. We demonstrate EDLCs with specific capacity values over 155 F/g at high mass loadings of 15 mg/cm2, and exceptional areal capacities of over 2.27 F/cm2 at low rates and 1.48 F/cm2 at high rates.

3.2 Experimental

Hierarchical porous carbons (HPC's) were synthesized as described in Chapter 2. In these experiments, HPC's of various sizes were synthesized by varying the amount of $ZnCl_2$ present during the reaction. Sizes of varying pore size were used in electrochemical testing corresponding to small, medium, large and extra-large pores (Figure 10).

A composite was made from the HPCs for EDLC testing. This was achieved by mixing the desired HPC, conductive carbon (Super P), and polytetrafluoroethylene (PTFE) together in a 7:2:1 by weight ratio in an agate mortar, respectively. Water was added to create a free standing film, which was pressed at various thicknesses. Samples were dried in a vacuum oven at 120 °C overnight, cut into circular electrodes with a diameter of 4 mm, then immersed in an ionic liquid electrolyte, 1-ethyl-3-methylimidazolium tetrafluoroborate ($EMIMBF_4$). The symmetric cell was made by pressing two electrodes between 2 gold coated glass slides with a Whatman ashless filter paper as the separator.

Cyclic voltammetry (CV), galvanostatic charge-discharge (GCD), and electrochemical impedance spectroscopy (EIS) were obtained from a CHI760e using symmetric double cells. Specific capacity (C_s, F/g) is measured from the GCD using $C_s = 2It/mV$, where I is the discharge current, t is the discharge time, m is the mass of HPC in a single electrode, and V is the potential

window. Device capacities (C_{all}, F/g_{all}) are calculated by incorporating inert components utilizing the formula $C_{all} = C_s/(1+\sigma_{inert}/\sigma_A)$ where σ_{inert} is the inert component's mass loading (chosen to be 10 mg/cm^2) and σ_A is the mass loading of the HPC. Areal capacity (CA, F/cm^2) is calculated as $C_A = C_s*\sigma_A$. Energy (E, Wh/kg) is determined using $E = \frac{1}{8}C_sV^2$ and power (P, W/kg) is found with $P = E/t$.

3.3 Results & Discussion

To assess the electrochemical properties of the HPCs, EDLCs were made and tested by cyclic voltammetry (CV), galvanostatic charge-discharge (GCD), and electrochemical impedance spectroscopy (EIS). Figure 17a & b show a typical GCD and CV, respectively. Figure 18a represents the capacitance vs. current density at a low loading (3 mg/cm^2) of each HPC. It can be seen that at lower mass loadings the samples are relatively similar, with little capacity degradation comparable to that of other carbon materials using ionic liquids as the electrolyte.[60,67] At low current densities and low loading the highest capacities are achieved. At 0.5 A/g with a loading of

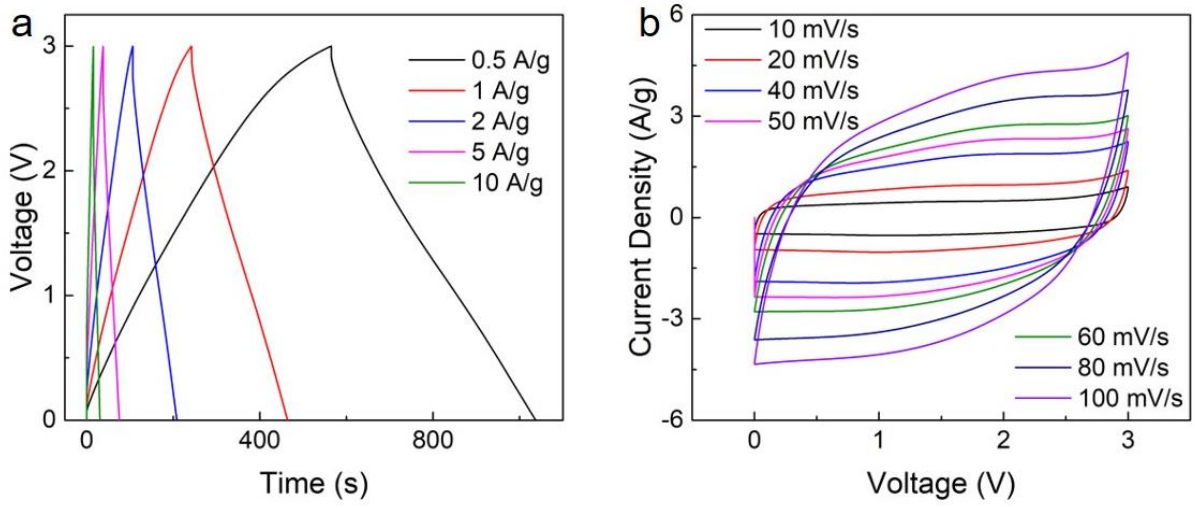

Figure 17. GCD (a) and CV (b) of a typical HPC. The plots exhibit capacitive behaviors with triangular shapes in the GCD and box-like shapes for CV, even at high current densities and scan rates.

3 mg/cm^2 the s, m, L, and XL-HPCs exhibited similar gravimetric (specific) capacities of 171 F/g, 163 F/g, 162 F/g, and 192 F/g, respectively. At this current density, the surface area is more impactful for the smaller HPCs, as s-HPC (2581 m^2/g) has a higher capacitance over m-HPC (2189 m^2/g); both of which have similar pore size distributions. However, L-HPC (1711 m^2/g) and XL-HPC (1614 m^2/g) appear to overcome their low surface area with increased pore accessibility from the hierarchical porous structure as both have lower surface area than s & m-HPC, but rise in capacity. At a higher current density of 10 A/g, the benefit of the hierarchical porosity becomes more evident as the overall capacities for different HPCs drop to 95 F/g (s-HPC), 101 F/g (m HPC),

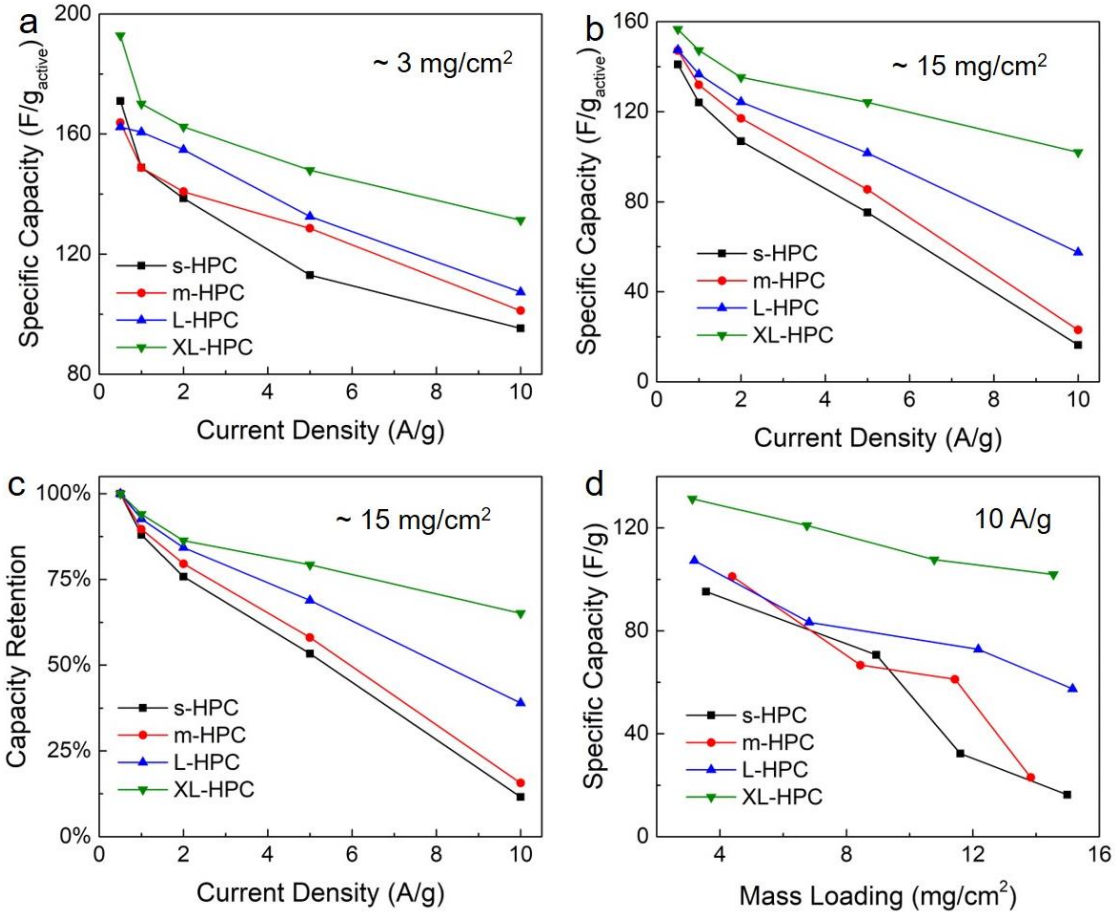

Figure 18. Capacity vs current density plots of each HPC at 3 mg/cm2 (a) and 15 mg/cm2 (b). HPCs with a larger pore size distribution show enhanced capacity retention for high loading (c). Capacity vs mass loading at 10 A/g displays the effectiveness of each HPC as loading is increased (d).

107 F/g (L-HPC), and 131 F/g (XL-HPC). Here the importance of the hierarchical porosity in facilitating more efficient mass transport is clearly manifested, as the samples with the larger pore sizes show higher capacities, as well as a smaller drop in capacity. XL-HPC achieves the highest capacity of 192 F/g, representing the highest value achieved in a CTF derived carbon in a symmetric cell.[13] At a loading of 3 mg/cm^2 with an ionic liquid electrolyte, this data is on par with that of literature values that have capacities ranging from 150-200 F/g at low current densities.[67–71]

At high mass loadings, the capacities differ substantially. An expected drop in specific capacity is observed for all electrodes, due to larger resistances and ion transfer distances in thicker electrodes Figure 18b).[72] Nonetheless, it is apparent that the samples with the larger pores better retain their capacities and rate performance when compared to that of the smaller pore HPCs, demonstrating that the larger pore samples are able to cope with high currents at high loading much better than that of their smaller pore counterparts. At a low rate of 0.5 A/g each HPC has a capacity around 150 F/g. This quickly changes as the current density rises, and at 10 A/g the capacities are

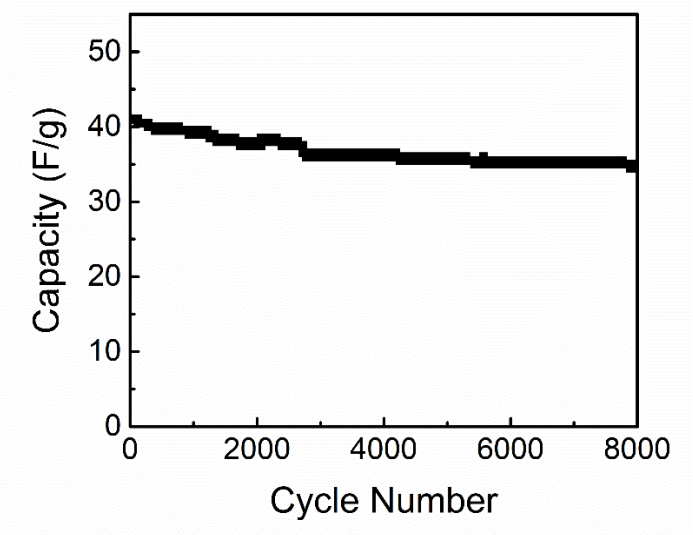

Figure 19. Cycle stability curve for m-HPC at 7.5 A/g. Capacity vs cycle number over 8000 cycles representing a loss of 85% from 41 F/g to 35.5 F/g.

16 F/g, 21 F/g, 57 F/g, and 102 F/g for the s, m, L, and XL-HPCs, respectively. Figure 18c displays the capacity retention trend as the current density rises for the HPCs. Specifically, XL-HPC, with its large pore size distribution, experiences an 65% rate retention relative to a 10% retention for the s-HPC at a loading of 15 mg/cm^2 and current density of 10 A/g. Even the L-HPC begins to show significant fading at this current density; although it is still superior to the smaller pore size HPCs. Once again, XL-HPC shows the best performance at high loading with capacities of 156 F/g and 102 F/g at 0.5 A/g and 10 A/g, respectively. The decreased rate performance as compared to the lower loading samples is due to the increased ion transfer distance.[61,72]

Figure 18d highlights the loading performance of the HPCs. This plot clearly shows how the loading of the sample is detrimental to the s-HPC and m-HPC at 10 A/g. XL-HPC and L-HPC are able to maintain their capacities even at high mass loadings, as seen from the shallow slope of the mass loading curves. The s & m-HPC quickly lose capacity, as ion conduction becomes restricted at high loading in these pore size regimes. The high capacity retention at both high loading and high rate is attributed to the very large pores allowing for efficient mass transport and ion diffusion in the sample.[15,55,58,73] Electrodes also show moderate stability with 85% capacity retention over 8000 cycles (Figure 19).This is especially important for ionic liquids that lack high ionic conductivity.[60] Even though XL-HPC has the lowest surface area, it's huge pore size allows both easier ion conduction as well as better pore accessibility. Volumetric capacities show a similar dependence with the mass loading. At low rate (1 A/g), all HPCs having a relatively constant volumetric capacity over all loadings; on the other hand, at high rate (10 A/g), only XL-HPC maintains a nearly constant volumetric capacity with increasing mass loading, while all other materials show considerable degradation in volumetric capacities at high mass loading due to charge transport limitations (Figure 20a & b).

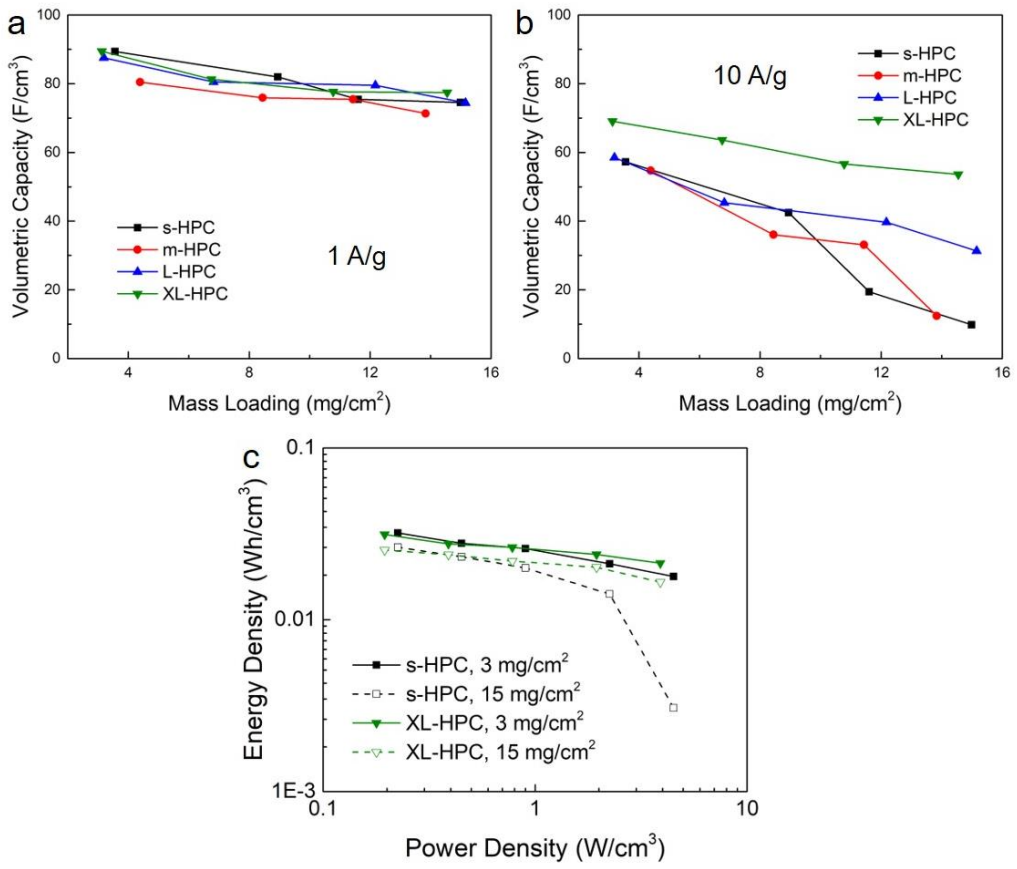

Figure 20. For a low rate of 1 A/g (a) each curve has a relatively flat slope, while at a higher current density of 10 A/g (b) there is significant reduction of capacity for s and m-HPCs. (c) Volumetric Ragone plot for s, and XL-HPC at low and high mass loadings.

Specific capacity normalized by the mass of the active material isn't the best way to evaluate the performance of EDLC, particularly at low mass loading where the passive components make up a large fraction of the total mass in the device. For practical applications, the areal capacity could be a more appropriate parameter to evaluate the practical performance of EDLCs, since all passive components are largely constant in a given area.[74] At a low current density of 0.5 A/g, there is barely any difference in areal capacity for all the HPC samples (Figure 21a). There is a clear linear trend between areal capacity and mass loading at this current density. High values above 2 F/cm^2 are achieved for each HPC at loadings of ~ 15 mg/cm^2, with XL-HPC having the highest at 2.27 F/cm^2. These values are quite high for EDLCs with ionic liquid

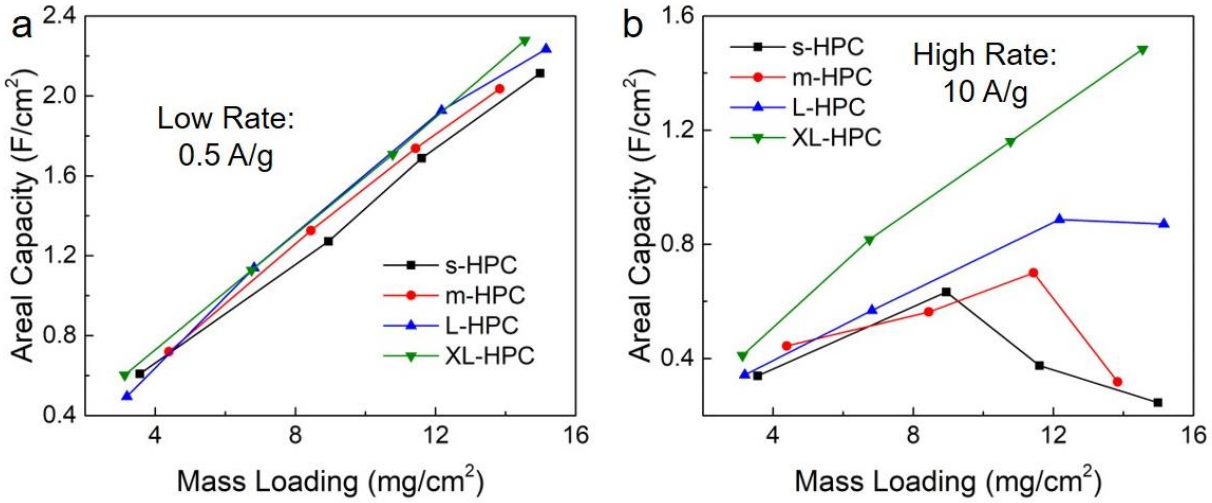

Figure 21. The areal performance at 0.5 A/g (a) and 10 A/g (b) for each HPC. Significant capacity decay is observed for high rate samples, however XL-HPC shows limited fading.

electrolytes, and rival that of aqueous based electrolytes.[58,75,76] At high current densities the HPCs show substantially different behavior with increasing mass loading (Figure 21b). The linear trend disappears, indicating severe ion transport limitations in thick electrode at high current density. The s-HPCs areal capacity shows no increase, indicating the higher material loading is completely offset by the capacity loss due to the transport limitations. There is an initial increase in the areal capacity of m-HPC, however at high loadings of 15 mg/cm^2, the resistance and transport limitations outweigh the benefit of the higher loading. A similar trend is observed for L-HPC; however, the areal capacity decay is much less. Only at the extreme pore size distribution of XL-HPC is there no areal capacity decay with increased mass loading. A high value of 1.48 F/cm^2 is achieved at 10 A/g for this material. Similar to the gravimetric capacitance, the areal capacity is severely impacted by the hierarchical pore size distribution in the HPCs. The larger pores allow for more efficient ion diffusion, even in thick electrodes at both low and high current densities. This is crucial for industrial scale applications where thick electrodes are necessary.

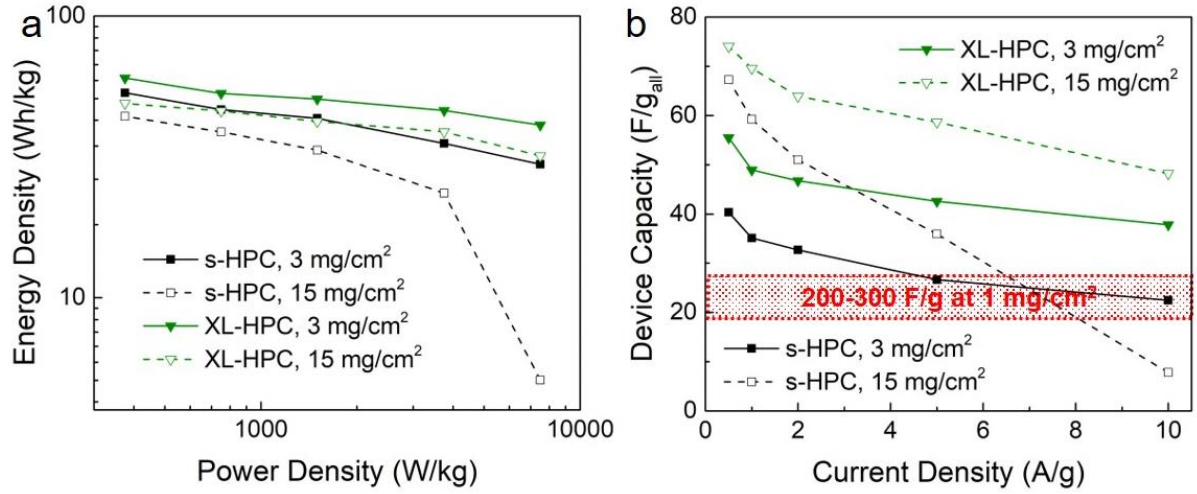

Figure 22. Ragone plots (a) of s-HPC and XL-HPC at high and low loadings. Gravimetric capacitance is normalized by the overall total weight of the device, giving values of device capacity (b). Devices with high gravimetric capacities but low loading are incorporated to show where they fall in terms of device capacitance.

A Ragone plot for both high and low mass loading s-HPC and XL-HPC are presented in Figure 22a. The highest energy density and power density achieved were 60.2 Wh/kg and 7500 W/kg, respectively. These values are consistent with other carbon based materials using ionic liquid electrolytes.[60,69,70] However, it is noteworthy that values of 48.9 Wh/kg at 375 W/kg are achieved with a mass loading of 15 mg/cm^2; a loading that is 5-15 times higher than that of most literature values. Furthermore, at a power of 7500 W/kg the energy only decreases to 31.8 Wh/kg, indicating high energy retention. Ragone plots do not account for material loading, so comparable energy and power densities at such high loadings is impressive. The volumetric Ragone plot shows a similar trend as well (Figure 20c).

Figure 22b takes the mass of the passive components into the gravimetric capacity calculation. This is another way to factor in mass loading similar to areal capacity. A value of 10 mg/cm^2 is chosen for the inert components (a mass loading comparable to common current collectors).[73] Many EDLC materials in literature can reach up to 200 F/g, and some over 300 F/g

at low mass loadings.[15,20,24] However, the loading of many of these materials rarely exceed 1 mg/cm^2. When weighted by the total device, these capacities drop dramatically (red shaded region in Figure 22b). For example, a device with a capacity of 300 F/g at 1 mg/cm^2 has a device capacity of 27 F/g_{all} assuming a 10 mg/cm^2 loading for inert components. Even with the lowest loading of the s-HPC (3 mg/cm^2) the device capacity reaches a comparable 35 F/g_{all} at 1 A/g. However, with a higher loading these values are increased greatly. Both of the 15 mg/cm^2 HPCs show high device capacities at low rates, however s-HPC exhibits a sharp drop in device capacity as the rate is increased, eventually dropping well below that of conventional EDLCs. On the other hand, XL-HPC shows high device capacities of 74 F/g_{all} and 48 F/g_{all} at current densities of 0.5 A/g and 10 A/g, exhibiting outstanding loading and rate performance. The large hierarchical pore size distribution of XL-HPC is crucial for maintaining a high rate and high capacity at high loading.

Electrochemical impedance spectroscopy provides further insight into the excellent performance of HPCs. Nyquist plots of the HPCs are displayed in Figure 23a. The semicircles for each plot decreases with increasing pore size. This region represents the bulk electrolyte resistance;

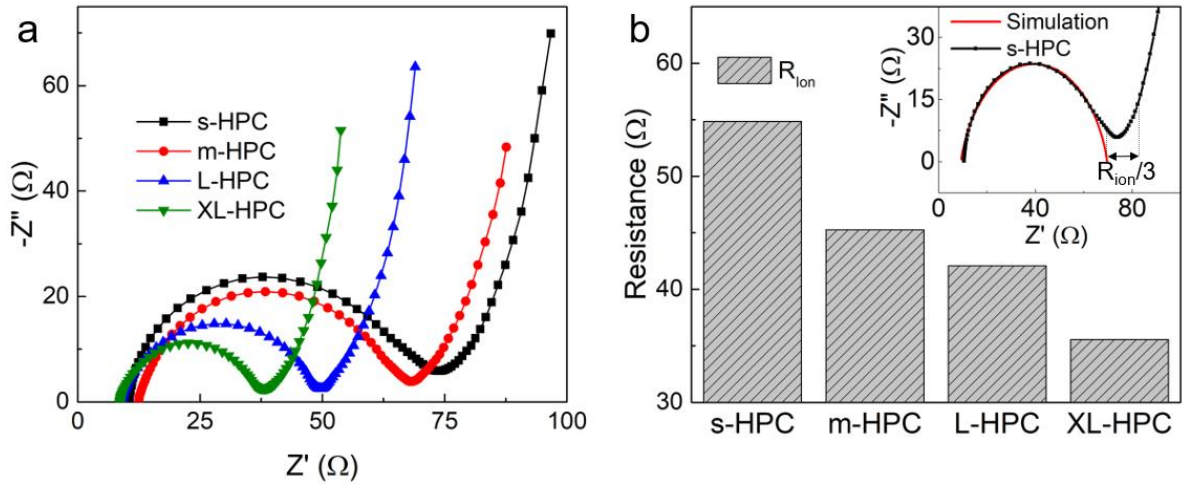

Figure 23. A Nyquist plot of the HPCs with varying pore sizes (a). The semicircle decreases in size with larger pore size HPCs, indicating lower electrolyte resistance. The diffusive resistance in the pores is calculated and found to decrease with increasing pore size (b).

the larger the semicircle the greater the resistance.[77] Similar phenomena have been reported with ionic liquids with varying pore sizes.[67] A decrease in bulk electrolyte resistance is thought to represent an increase in ion mobility.[67] The trend reinforces the GCD data that larger pores allow for enhanced pore accessibility.

The diffuse layer resistance (Figure 23b inset) is represented by the part of the Nyquist plot that has a 45°, before the sharp increase in slope. This region indicates non-faradaic processes, and can be used to calculate the resistance of the electrolyte in the pores, termed R_{ion}.[73,78,79] A simulation was used to determine the semicircle region to get an accurate value for the 45° region for R_{ion} calculations. Ion resistance is shown to decrease with increasing pore size. This trend, combined with the bulk electrolyte results, indicate that the large hierarchical porosity in the HPCs enable high ion mobility and charge transfer during cycling, granting high rate and loading capabilities.

3.4 Conclusion

Capacities attained were consistent with current EDLCs using ionic liquids with a maximum of 192 F/g at 0.5 A/g. However, HPCs displayed superior areal capacities up to 2.27 F/cm^2 due to heightened pore accessibility and ion mobility which was confirmed by EIS measurements. When normalized by the total device weight, HPCs outperformed other materials with an impressive 74 F/g_{all} vs 27 F/g_{all} of an idealized capacitor material (300 F/g at 1 mg/cm^2). Mass loading is not a common parameter investigated in EDLCs, however it is crucial for the development, and implantation of real life devices.[74] Herein, HPCs are displayed to have tunable hierarchical porosities with excellent electrochemical performance. Contrary to current literature,

a larger pore size distribution (with some pore volumes being attributed to pore over 50 nm in diameter) is beneficial to EDLCs, especially for high loading and high rate applications.

CHAPTER 4: SUPERCAPACITORS AS AN EDUCATIONAL TOOL

4.1 Introduction

The focus on renewable energy generation is increasing due to the quest for clean energy. However, the success of clean energy depends on the ability to store it. The field of energy storage is one of the most relatable, relevant, and diverse subjects with an interdisciplinary mix of sciences including chemistry, physics, and engineering. Many students never get a chance to have hands on experience with energy storage technology (at most only covering a galvanic cell) due to many factors ranging from expensive instrumentation, material sensitivity to air/water, complex material synthesis, intricate device preparation, hazardous chemicals, and cost. This lab aims to address many of these problems and provide a laboratory experience for upper level science undergraduates to fabricate supercapacitor devices and test them. The lab will also allow students to have hand on experience with graphene, one of the most popular and exciting 2D-materials.

Supercapacitors are an excellent option to teach energy storage in a laboratory setting because the electrodes and devices are easy to fabricate and they are very safe. Unlike batteries, no glovebox or hazardous materials like metallic lithium are required. Cyclic voltammetry, galvanostatic charge/discharge, electrode synthesis, and device preparation are all techniques used during the lab that are directly applicable to research and industry. The main deterrent for supercapacitor laboratory experiments (as well as battery labs) is the electrode and device fabrication. Normally, slurries are utilized as the electrode and coin cells are used for the device. The processing involved with these methods takes practice, but more importantly time – a precious commodity to undergraduate students. This lab utilizes reduced graphene oxide as the electrode to circumvent these problems. When graphene oxide is reduced under the right conditions it self-

assembles into reduced graphene oxide hydrogels. These can directly act as the electrodes which can be pressed by binder clips to make a simple, functional device.

In the lab, students simultaneously learn about morphology control at the nanoscale, and energy storage. Two different morphologies of electrodes are made; one open and porous and one small and compact. It is easy to see these differences by the naked eye, as well as under high powered microscopes. The students learn about how the morphology at the nanoscale impacts surface adsorption and ion accessibility. Using two different electrolytes paired with different electrode pore morphologies, students learn about capacity, energy density, and power density. Aqueous electrolytes have superior ion mobility through both the compacted and open electrodes and the ionic liquid has limited mobility due to the large ion size. Students can explore the pros and cons of each type of electrolyte and how they could apply each one to different real-world situations. A full lab guide can be found in the Appendix A.

4.2 Experimental

Students work in groups of 2 over the course of 3 lab periods lasting 4 hours each. The lab can be modified to be shorter or longer, and can be taught at various levels to cater to the audience being taught. The device fabrication can be seen in Figure 24, as well as the full synthesis in Figure 25.

For preparation of the electrodes, students prepared 1 mL of a 1 M ascorbic acid solution (does not need to be volumetric). To a single container, students added 0.60 mL of the ascorbic acid solution, followed by the appropriate amount of stock GO and water so that the final concentration will be 1.5 mg/mL GO after all reagents are added together. After mixing the solution vigorously (sonication if available), students pipetted 1.0 mL of the solution into an 8 mL

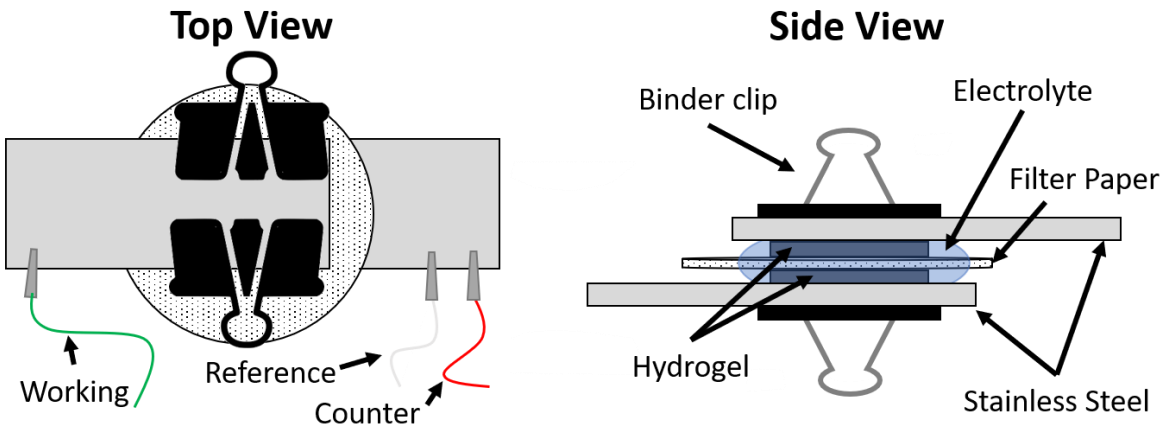

Figure 24. A fully fabricated symmetric cell. This picture is an easy reference for students to use to correctly fabricate the device.

black cap dram vials, and repeated until no solution is left. The caps of the vials were tightly sealed, and placed into an oven set to 95 °C for 1 hour.

After the reduction of GO to rGO has taken place, small black cylinders formed (Figure XB). The newly formed rGO hydrogels must then be washed of any remaining ascorbic acid. All of the hydrogels were carefully removed from the containers and placed into a large beaker. The beaker was filled with water and gently swirled. After waiting 5 minutes, the water was drained from the beaker leaving the hydrogels behind.

Half of the hydrogels were frozen, while the other half was not. They are then all left out to air dry overnight. The previously frozen hydrogels maintain their shape to form porous graphene hydrogels (PGH), while the unfrozen samples shrink dramatically to for nonporous graphene hydrogels (NGH). These dried hydrogels will serve as the electrodes.

In order to fabricate the device, the dried hydrogels were submerged into either 1.0 M H_2SO_4 or 1-Ethyl-3-methylimidazolium tetrafluoroborate ([EMIM][BF_4]) for one hour. After soaking, they were fabricated into symmetric devices by stacking a hydrogel on top of a stainless-steel strip, then a piece of filter paper soaked in the appropriate electrolyte, followed by the other

hydrogel. Finally, another stainless-steel strip was laid on top offset from the bottom layer. The entire device is then secured by two binder clips (Figure 24).

The devices were then tested using CV in 1.0 M H_2SO_4 from 0 – 1 V, and [EMIM][BF_4] from 0 – 2.5 V, with scan rates of 25, 50, 100 and 200 mV/s. GCD is also tested using the same electrolytes and voltage windows, however the current density used is 0.5, 1, 2, 3, and 5 A/g. For aqueous electrolytes additional GCD current densities of 7.5, 12.5, and 20 A/g are tested. If the aqueous cycling curves appeared stable, the current density was increased by an additional 10 A/g until failure (the instrument either fails to run the test, or the curves are severely deformed).

Safety is a key factor in many teaching labs. Fortunately, this experiment uses air and water stable electrodes, so the main hazards are the electrolytes 1.0 M H_2SO_4 and [EMIM][BF_4]. The sulfuric acid is highly concentrated and the ionic liquid is a mild irritant, so gloves are necessary when building the devices. The ascorbic acid, GO, and rGO are all safe to handle and pose little threat to a student's skin.

4.3 Results & Discussion

Students synthesize electrodes, then fabricate supercapacitor devices with them. Graphene oxide acts as the precursor to the free standing electrodes. This experiment allows for students to gain hands on experience with one of the most exciting and promising nanomaterials – graphene. It can be bought commercially or made with Hummer's method.[36] If instructors want to spend more time discussing graphene or even characterizing it pre- and post-reduction, the Zelechowska group has an excellent protocol to follow.[80]

During the reduction process the brown graphene oxide solution (Figure 25a) self assembles into a free standing reduced graphene oxide hydrogel (Figure 25b). Normally, the hydrogels are freeze dried in order to preserve their porosities, however this may be difficult for undergraduate labs that may not have the proper equipment. Thus, a natural drying approach is used. Students make two sets of hydrogels; one being porous, and the other relatively nonporous. This is achieved by freezing one set (Figure 25c), and leaving the other at room temperature. During freezing, ice crystals form and push rGO sheets together creating sturdy structural walls.[81] Upon air drying, the frozen rGO hydrogels are able maintain their shape unlike the non-frozen samples which collapse from the capillary forces from the evaporating water.[82] The frozen hydrogels are termed porous graphene hydrogels (PGHs) and the non-frozen samples are termed nonporous graphene hydrogels (NGHs). SEM pictures reveal that the PGH maintain porosity

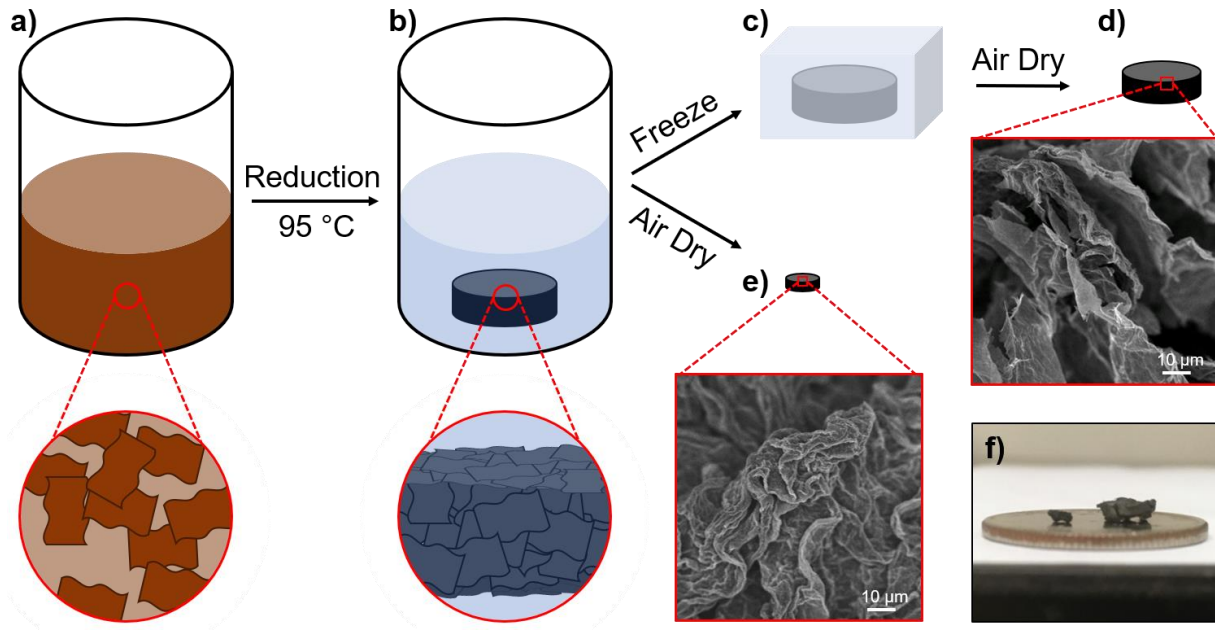

Figure 25. The full synthesis is highlighted here. a) First GO is diluted and mixed with the reducing agent. b) The rGO is heated with ascorbic acid to form rGO hydrogels. c) Half of the hydrogels are frozen. After air drying the hydrogels that were frozen d) maintain their open structure or e) shrink dramatically. f) Actual formed hydrogel differences, with a quarter to scale.

(Figure 25d) while the NGH have very little (Figure 25e). These results are seen on the macroscopic scale, as the NGHs have a dramatic reduction in volume Figure 25f).

Now that the students have nanostructured their electrodes they can make predictions about the performance of each type; either porous or nonporous. Next, the electrodes are soaked in two different electrolytes, 1.0 M H_2SO_4 and [EMIM][BF_4]. These different electrolytes will be used to probe the difference between power and energy by simply changing the electrolyte and leaving the electrode morphology the same. Aqueous electrolytes typically have high capacities and power however they are restricted to low voltage windows (water splitting occurs at >1.23 V) which

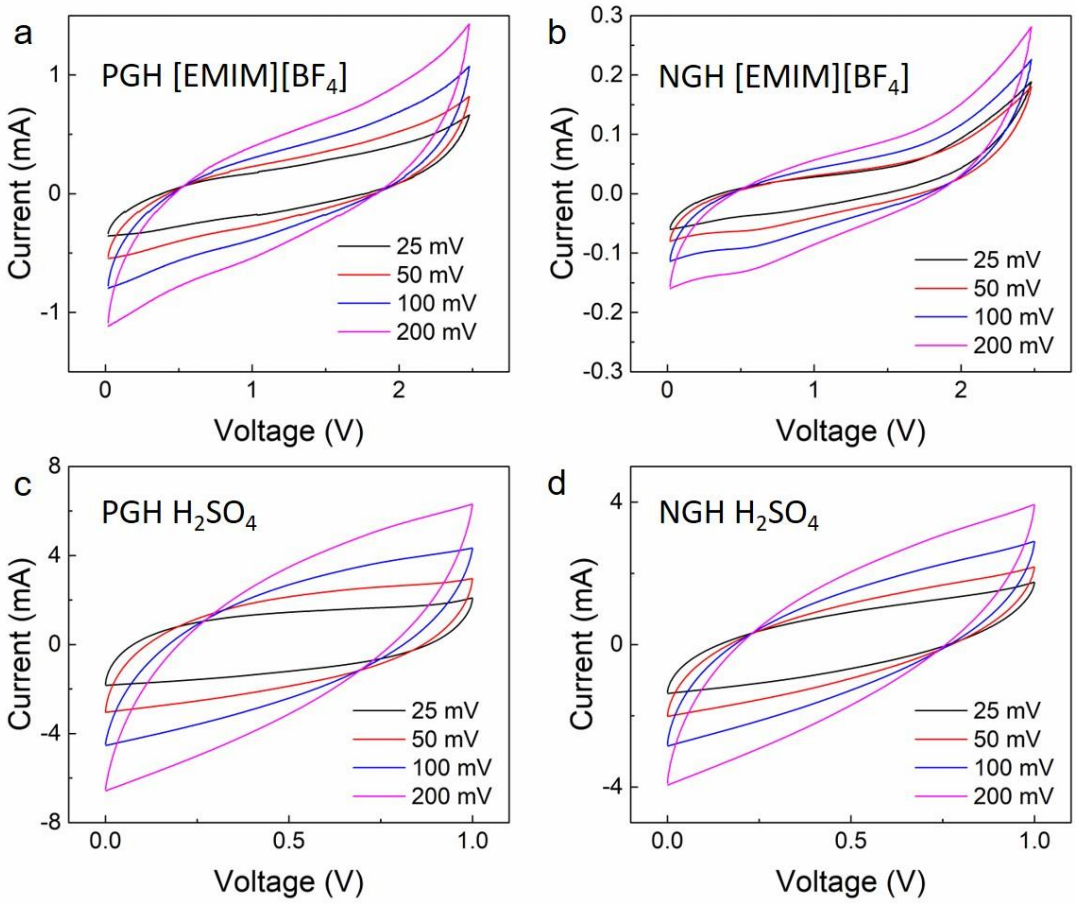

Figure 26. Cyclic voltammetry results of each electrode. Ionic liquid electrodes with PGH (a) and NGH (b) deform even at low scan rates signifying poor rate performance. Aqueous electrolytes appear ideal for both PGH (c) and NGH (d).

limits energy density. Ionic liquids are the opposite, having relatively low power but very high energy density due to large voltage windows.

The cyclic voltammetry results show the differences between both the electrolyte used as well as the morphology of the electrodes. In an ideal supercapacitor the CV should be a perfect rectangle due to pure capacitive current. However, once the scan rate is increased high enough, the diffusion of electrolyte can no longer proceed to completion. Physically this means electrolyte is not completely filling the pores due to the rapidly changing potential.[83] Once electrolyte can no longer fill all the pores, the normal rectangular shape of the CV becomes distorted giving the shape of an oval. Internal resistance beings to dominate in this regime, as was the capacity of the device drops (a resistor would give a perfect line on CV).[84]

It can be seen that the PGH and NGH with [EMIM][BF_4] have misshapen curves, even at low scan rates (Figure 26a & b). It is important to note that the scale of the PGH is much larger than the NGH, signifying more current, thus a higher capacity. These data show how the bulky ions of [EMIM][BF_4] have more difficulty accessing the electrode pores, even in the porous sample. Qualitatively the PGH maintains a more rectangular shape vs the NGH signifying a higher rate capability. For the aqueous electrolytes, the CV curves are much more ideal. Rectangular shapes appear even at high scan rates of 100 mV/s for the PGH Figure 26c), while the NGH begins deformation earlier (Figure 26d). In general, the PGH show more capacitive curves over the NGH samples due to ion accessibility in the pores. Comparing H_2SO_4 to [EMIM][BF_4] it can be seen how much more easily diffusion is for aqueous electrolytes over the ionic liquid. Students can discuss the differences in morphologies and electrolytes from these graphs. In addition, they can speculate on how different morphologies and electrolytes can be used to increase the performance of the electrodes.

The capacity plots explore a much more quantitative analysis of the supercapacitors. As expected, the NGH have lower capacities than their PGH counterparts. The ability of electrolyte to easily access electrode surface and flow in and out of the electrode is enhanced by the high porosity of the PGH. At low rates the electrolyte has ample time to diffuse into the electrodes, as seen with the PGH and NGH which have relatively similar capacities of 84 F/g and 72 F/g respectively. As the rate is increased, the NGH electrode quickly drops in performance, while the PGH is able to cycle with relative ease. The porous structure allows for cycling up to 20 A/g where the NGH barely has measurable capacity at 5 A/g. In the [EMIM][BF_4] electrodes a similar trend is seen, albeit more extreme. The NGH can barely cycle even at the lowest rate of 0.25 A/g, where

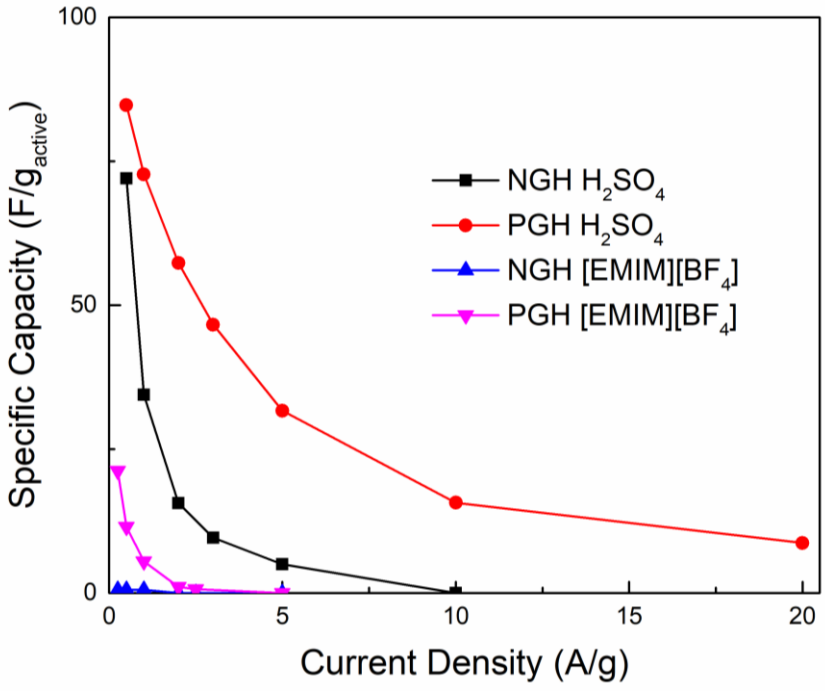

Figure 27. Here PGHs and NGHs are compared with two different electrolytes, H_2SO_4 and [EMIM][BF_4]. It can be seen that PGH outperform NGH with the same electrolyte due to the porous structure. In addition, aqueous electrolytes outperform ionic liquids significantly. The high mobility and small size of aqueous electrolytes are demonstrated through this data, while the opposite is true for ionic liquids.

the PGH is able to attain a capacity of 21 F/g. This is attributed to the large ions in [EMIM][BF_4] having a significantly lower ion mobility and size, making the pore effects more pronounced.

It appears as though the electrode morphology is not the dominant factor when comparing H_2SO_4 and [EMIM][BF_4]. From the capacity vs current density graph (Figure 27) it can be seen that H_2SO_4 outperforms the [EMIM][BF_4] electrodes, even when the electrode is nonporous. This is due to the very high ionic mobility of H^+ and SO_4^- allowing for easy diffusion throughout the electrode, even in the nonporous sample. Before the students calculate the energy and power densities they can discuss which supercapacitor they think will provide the best power and energy. It's important to reiterate how energy density is proportional to the voltage squared, while power is only linearly correlated.

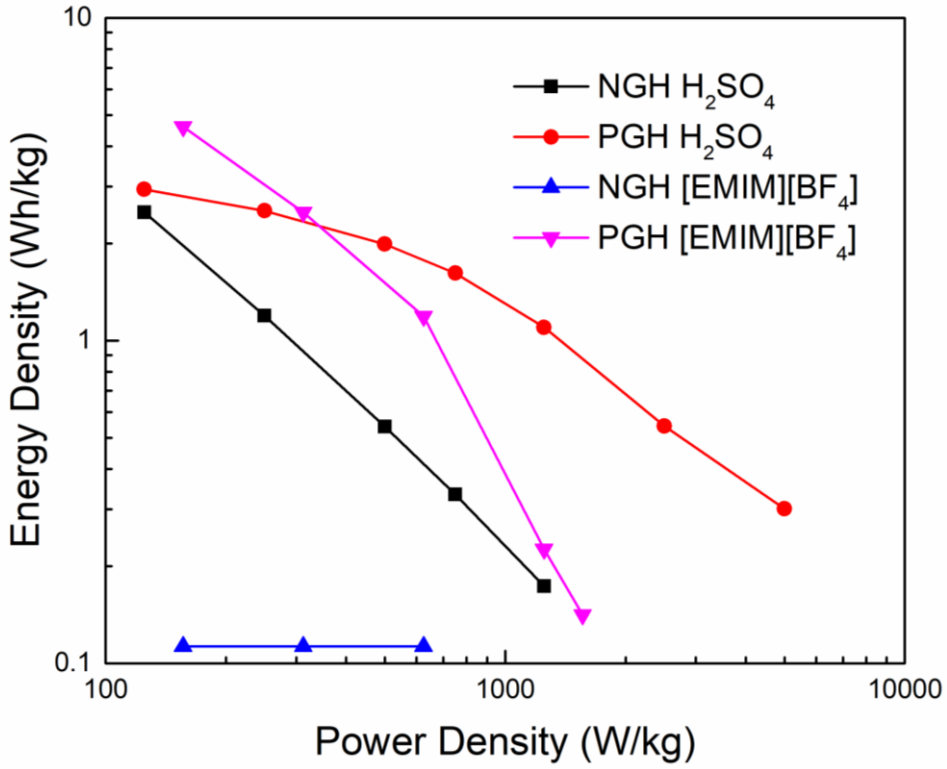

Figure 28. A Ragone plot of each device. The PGH with [EMIM][BF_4] has the highest energy density, but only at low powers. The PGH with H_2SO_4 quickly overtakes the ionic liquid sample with high energy, even at high powers.

The energy density and power density take the voltage window in consideration, giving a complete view of the performance of the supercapacitors (Figure 28). Energy is proportional to the voltage window squared. This allows the ionic liquid samples to attain very high energy densities, but only at low power. The PGH attains a value of 4.6 Wh/kg at low power while the aqueous PGH's maximum energy density is only 2.9 Wh/kg. This difference exemplifies the importance of the voltage window when accessing the performance of supercapacitor devices. As power increases, the aqueous PGH overtakes the energy density of the ionic liquid PGH. Even though the electrodes have the same morphology, the electrolytes respond differently when pushed to high powers. The [EMIM][BF_4] beings to drop dramatically because the ions are not able to diffuse into the electrode. The H_2SO_4 can continue to diffuse due to the high mobility of the ions. Even the H_2SO_4 NHG is comparable to the PGH at high rates truly showing the differences in the electrolyte's motilities.

The students now have a complete set of data to draw conclusions from. Students should be able to see the importance nanostructuring electrodes as well as how the electrolyte dictates performance. Another exercise is comparing other modern energy storage technologies to the actual data obtained. It is also important to emphasize the specific use of the different devices made. For example, a high power device may be more suited for regenerative braking where power is more important over an electric vehicle where energy density matters more. There are many routes for discussion, which can all be catered toward different levels of education and audiences.

4.4 Conclusion

Reduced graphene oxide supercapacitors are an excellent way to teach undergraduate students about nanomaterials as well as energy storage. It gives a glimpse into modern nanoscience

by changing the nanostructure of a material to produce an observable result to the students. The stark contrast from the starting solution to a free standing electrode grabs attention of the students and promotes interest in the experiment. Graphene is a focal point which is interesting to the students, especially because it is popular in the media. The students also get hands on experience with developing energy storage devices, which they can relate to due to the prevalence of portable electronics. The lab can be completed in a reasonable amount of time (roughly over three lab periods) and requires minimal equipment to synthesize and test. The lab can also be expanded to include additional characterization, or shortened (only testing one electrolyte or morphology) to conform to a classes lab schedule.

CHAPTER 5: SYNTHESIS OF TRIAZINE MODIFIED GRAPHENE

5.1 Introduction

Graphene is an allotrope of carbon that is atomically thin 2D sheet of carbon with high conductivity, flexibility, and strength.[31] These properties have lead graphene to be one of the most promising new nanomaterials for a variety of applications like sensors, nanocomposites, and energy storage. However, the properties of graphene can be modified to fit almost any application. Different functional groups can be attached to graphene to enhance its solubility in a variety of solvents and reduce agglomerations to make processing easier. In addition to this, graphene can be chemically modified with catalysts for a variety of reactions including HER, ORR, menthol oxidation, and more.[30,33] One of the most common methods is loading nanoparticles on the graphene. The nanoparticles act as catalyst centers while the graphene acts a conductive scaffold to hold the particles and conducts electrons during the reactions.[85]

A newer method for catalyzing reactions is to synthesize single metal atom catalysts covalently bound to the graphene surface.[86] This has advantages over nanocomposites because it can greatly increases the number of active sites available for a reaction to take place as well as reducing the total amount of material needed to achieve the same performance. However, single metal atom catalysts have some problems. One of the biggest problems is that the catalyst loading is very low. This is an intrinsic problem, due to the fact that as single atoms, the total amount loaded will always be small in comparison to a substrate. It is common for catalyst loading to only be between 0.01 – 0.5 %, with only the highest loadings reaching 1%.[87] When trying to reach high metal content it is very difficult to avoid nanoparticle formation, thus metal content has remained

low. In this work we attempt to increase catalyst loading by utilizing chemically modified graphene to act as single metal atom catalysts.

Many aromatic nitrogen containing groups are excellent metal ligands, ranging from simple molecules like pyridines and triazine to more complex ones containing mixed denticity or polybipyridines.[88] Coupling these types of molecules to graphene is difficult, and has had limited success. In order to synthesis graphene with nitrogen containing functional groups fluorographene was used as a precursor. Fluorographene is graphene with a fluorine atom bonded to every carbon. Fluorographene has rich chemistries available and can be reacted with cyanide to form graphene with cyano groups attached to it termed cyanographene.[89] Herein we apply reaction conditions normally used for the trimerization of nitriles to monomer units with cyanographene present. We show that graphene can be functionalized with 2,4-bis(2-pyrimidyl)-1,3,5-triazine (BPT) in the hopes to use them for catalytic applications.

5.2 Experimental

First, cyanographene (CyG) was synthesized. To start, 200 mg of fluorographite was dispersed in 30 mL of DMF. It was then exfoliated by ultrasonication for 1 hour at 25 °C in an inert atmosphere producing a white dispersion (Figure 29a). Next, 1.3 g of NaCN was added to the flask and attached to a schlenkline under N_2 flow. The reaction mixture was heated at 130 °C for three days under a condenser. A control sample was heated under the same conditions without the addition of NaCN (Figure 29b). The now black solution was left to cool to room temperature. After cooling, an equal volume of acetone was added and the solution was centrifuged. The solid product was kept and the supernatant was discarded. The material was then successively washed

by DMF, dichloromethane, acetone, ethanol, and water 3 times per solvent. After washing the product was dispersed in water and freeze dried.

The molecule attached to the graphene is an analog of 2,4,6-Tri(2-pyrimidyl)-1,3,5-triazine (TPymT). TPymT was synthesized first as a comparison for the final chemically modified graphene. First, 1 g of 2-cyanopyrimidine was heated to 160 °C for one day in an inert atmosphere. The now solid product was ground in a pestle and mortar and washed with chloroform to remove unreacted starting reactant.

Similar reaction conditions to that of TPymT were used to form a 2,4-bis(2-pyrimidyl)-1,3,5-triazine (BPT) group attached to the graphene surface. The BPT graphene was synthesized

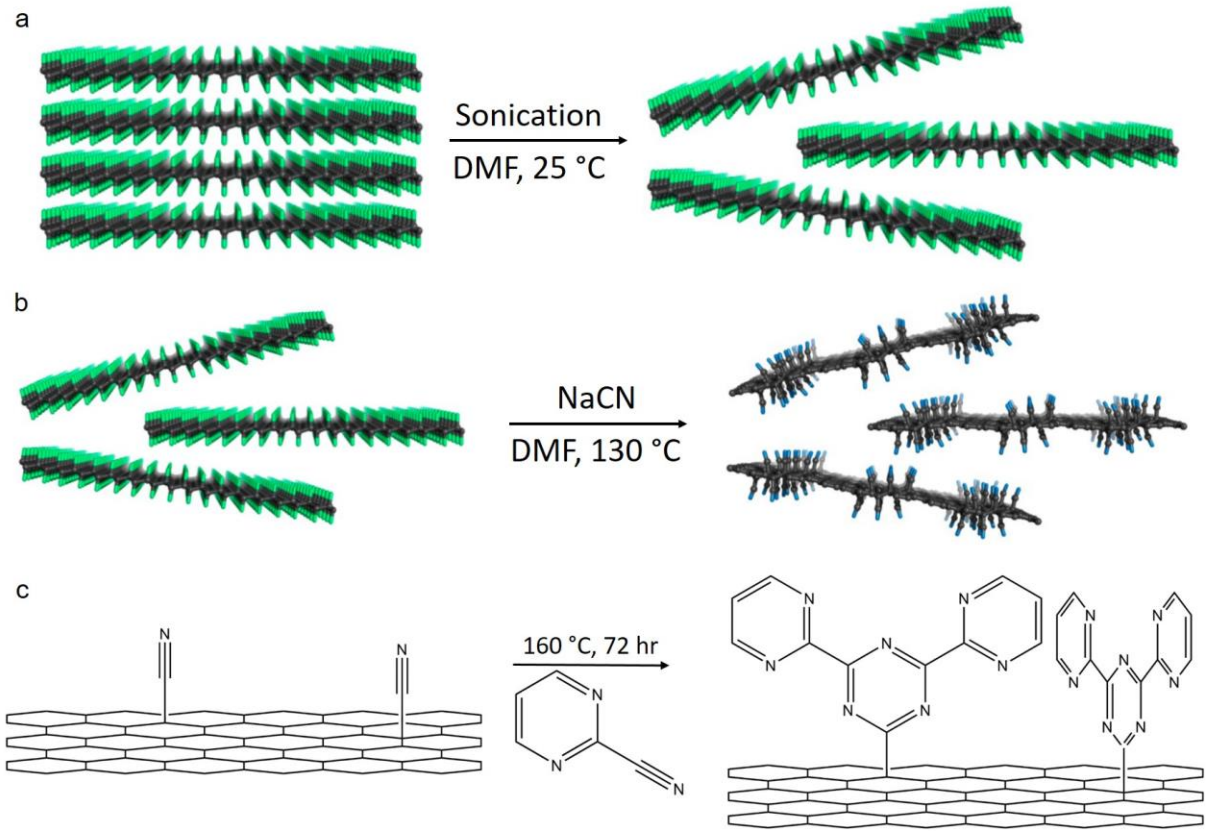

Figure 29. The overall reaction scheme of synthesizing triazine functionalized graphene. (a) Fluorographite is exfoliated by simple sonication methods. (b) Sodium cyanide is added under high heat to both remove fluorine atoms and chemically bond cyano groups to the graphene surface. (c) The last step involves the trimerization of the CyG with 2-cyanopyrimidine yielding the final product.

by the reaction of the freeze dried CyG with 2-cyanopyrimidine (CyPy) (Figure 29c). First, 1.0 g of 2-cyanopyrimidine was mixed with 50 mg of CyG. The reaction mixture was then heated to 160 °C, melting the 2-cyanopyrimidine which acted as the solvent and reactant. After 24 hours of heating the mixture was cooled to room temperature. The reaction mixture was wash with copious amounts of dichloromethane and water to remove any unreacted precursors as well as byproducts.

5.3 Results & Discussion

In order to synthesize BPT functionalized graphene, the precursor cyanographene was made as outlined in the experimental section. In addition, a control sample was prepared to ensure that heating fluorographene in DMF did not introduce any other functionalities.[90] The cyanographene was characterized by FTIR, XRD, and EDAX. The FTIR shows that under heating in DMF, the fluorographene loses a considerable amount of fluorine (Figure 30a). The sharp peak

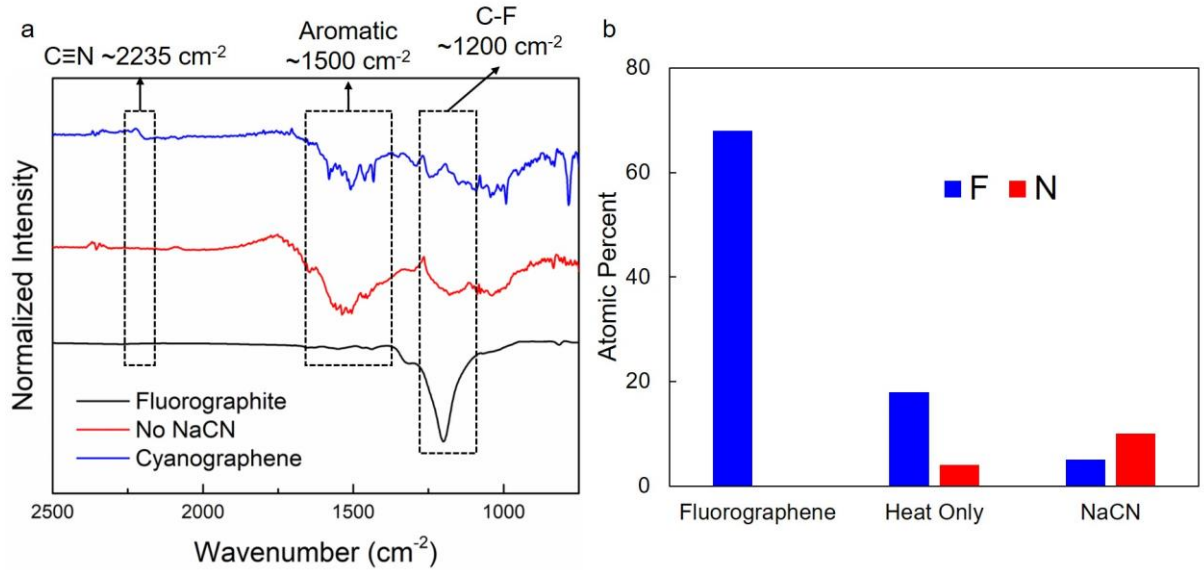

Figure 30. (a) FTIR results indicate the degradation of fluorographene under heating. When NaCN is introduced, a nitrile peak is observed around 2234 cm^{-2}. (b) EDS data show the cyanographene still appears to have a small amount of fluorine in the structure. It also indicates that DMF does introduce a small amount of nitrogen into the structure.

at around 1200 cm^{-2} wavenumber decreases while aromatic peaks around 1500 cm^{-2} appear. EDAX results confirm this loss, with only around 20% F remaining (Figure 30b). In the presence of NaCN, a nitrile group appears in the FTIR spectrum at 2235 cm^{-2}. In addition, aromatic groups can be seen similar to the heating only sample. EDAX confirms a large increase in nitrogen content, up to 10% in the cyanographene sample, however the heating only sample also shows a N increase of 4%. This indicates the actual amount of cyano functionalization is likely near 6%. There is also a small amount of fluorine left in the structure. This is attributed to incomplete exfoliation of fluorographite.

XRD of graphite, fluorographite, and the powered cyanographene were analyzed (Figure 31). Graphite has a well-known peak at around 26.5 ° with an interlayer distance of 0.33 nm.

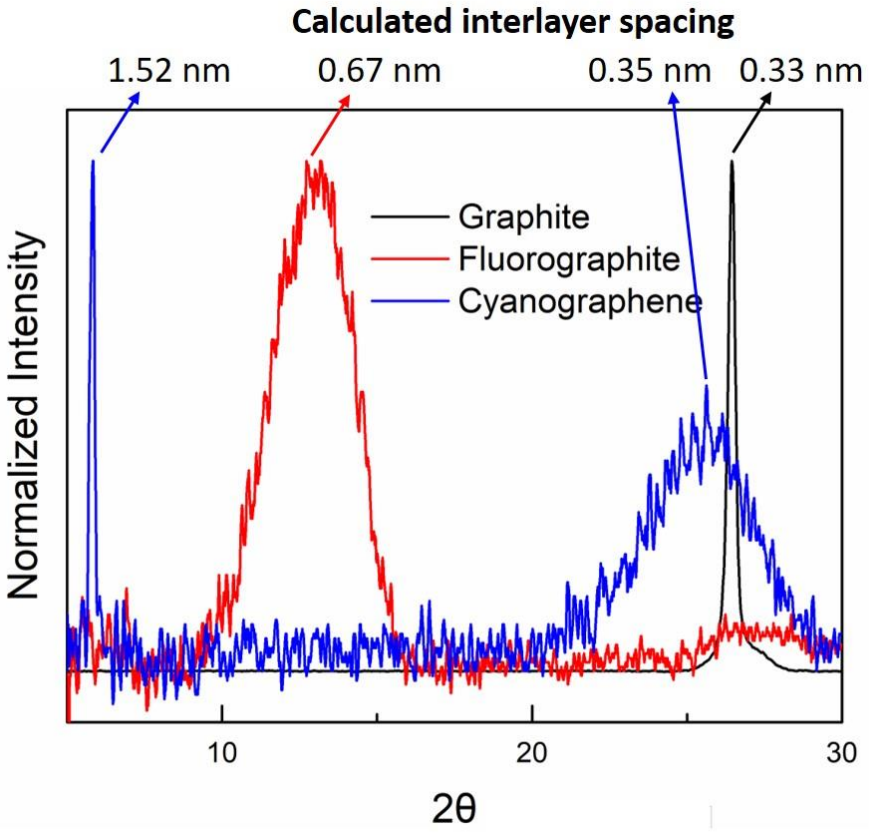

Figure 31. XRD shows the planar stacking peaks for graphite, fluorographite, and cyanographene. The enlarged spacing is indicative of a successful synthesis.

Fluorographene has a larger interlayer distance, corresponding to 0.67 nm.[37] This makes sense, as the carbon fluorine bonds are quite large. Upon cyano functionalization, 2 interlayer spacing appear. One at around 25.5 °and another at 5.8 °. The peak at 25.5 ° is very similar to peaks seen when graphene oxide is reduced to reduced graphene oxide.[31] It is slightly larger than graphite due to imperfect stacking caused by various functional groups on the surface of rGO. Similarly, this is expected for cyanographene as the process proceeds by a comparable mechanism. However, another peak at 5.8 ° is also observed. This corresponds to a 1.52 nm stacking distance. This may correspond to clustered areas of the graphene with cyanographene present. The clustering of functional groups was calculated in a previous paper, and is the most likely cause of this peak.[89] Together, this data indicates the successful synthesis of cyanographene.

Before the trimerization of graphene was completed, the molecular analog of the motif being added was synthesized. This was done by trimerizing 2-cyanopyrimidine at 160 °C. The

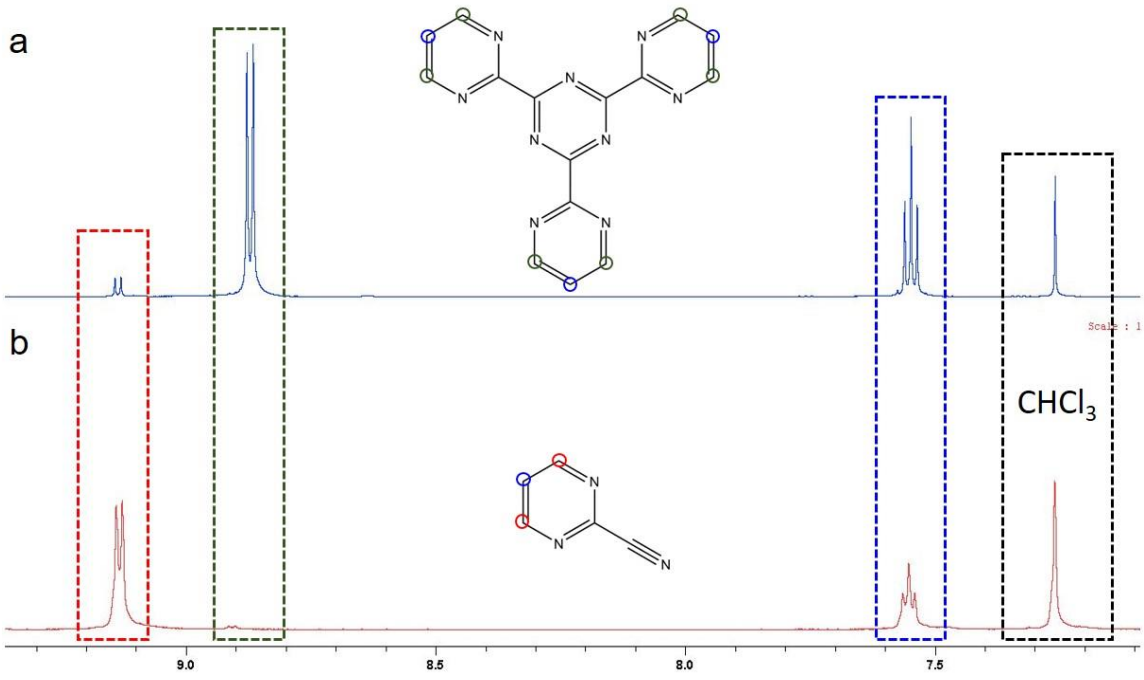

Figure 32. HNMR of (a) 2-cyanopyrimidine as well as (b) TPymT. It can be seen that the reactant and product are very pure, with only minimal left over reagent left after the reaction.

resulting product, TPymT, and 2-cyanopyrimidine were characterized by HNMR (Figure 32a & b). This is one of the only characterization methods that is useful because the functional groups of each are so similar. Figure 32a shows that the as synthesized TPymT is relatively pure, with minimal reactant left over signified by the peak at 9.1 ppm. The facile reaction method allows for almost no other byproducts to form as 2-cyanopyrimidine acts as the reactant and solvent.

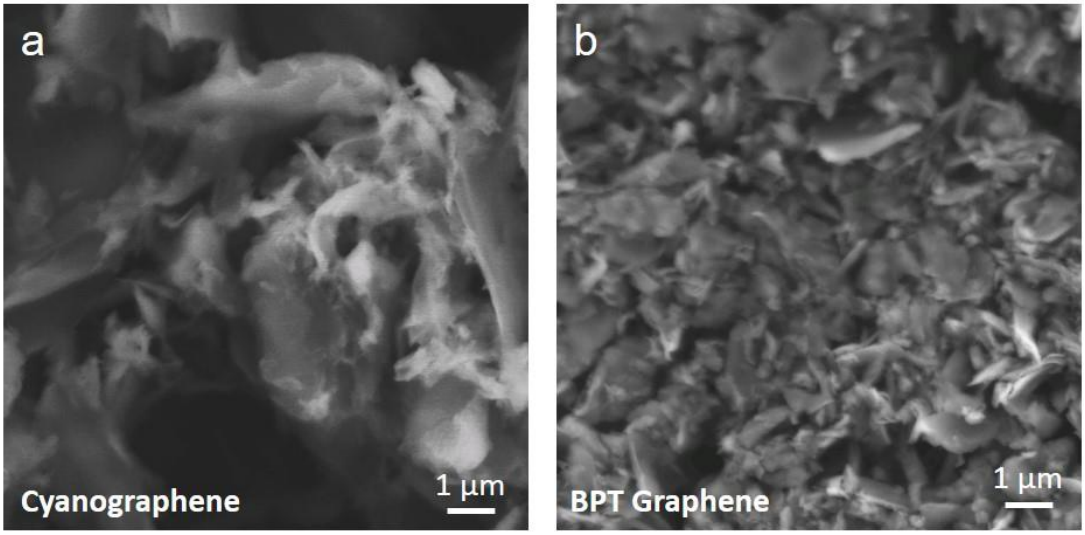

Figure 33. SEM of (a) cyanographene and (b) BPT graphene.

Finally, 2-cyanopyrimidine was reacted with cyanographene. This was completed the same way as the synthesis of TPymT. The CyPy was heated to 160 °C in the presence of a small amount of cyanographene in order to trimerize it. This forms both the BPT graphene as well as TPymT. The TPymT is simply washed out, leaving behind the BPT graphene. SEM images were taken of the cyanographene before and after functionalization (Figure 33). The cyanographene (Figure 33a) appears to be in much larger flakes as compared to the BPT graphene (Figure 33b). The reaction with CyPy may have fully

Characterization of the final product BPT graphene was very challenging. Almost all methods available cannot differentiate between the starting reactants and the product. Therefore,

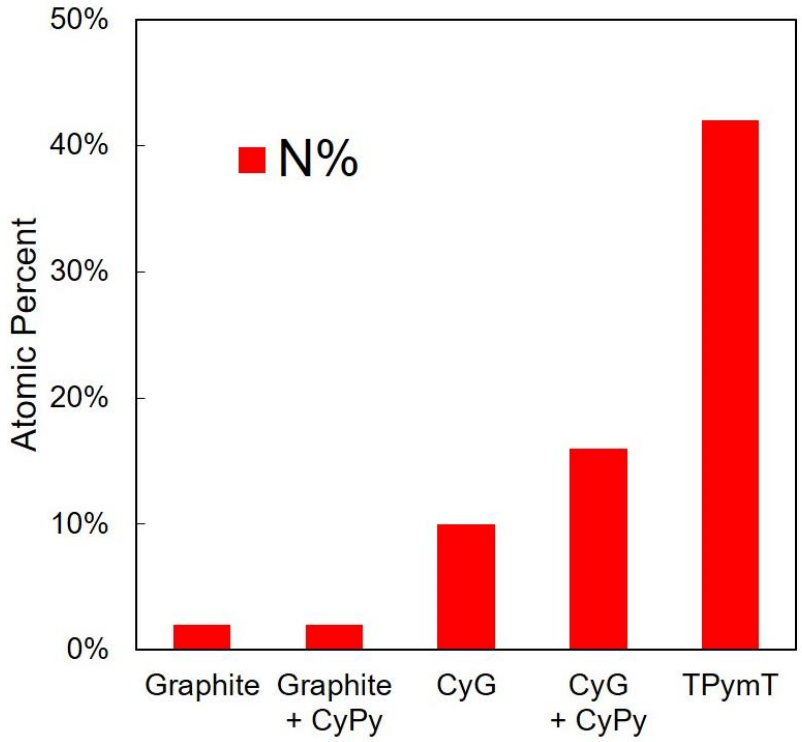

Figure 34. EDAX results for various reactions with 2-cyanopyrimidine (CyPy). Nitrogen content is only increase for reactants with an available cyano group.

EDAX was used to compare nitrogen content. Once cyanographene is functionalized, the nitrogen content should increase dramatically. However, there is a chance that during the synthesis excess TPymT will adsorb to the graphene. To account for this, the trimerization reaction was performed with both cyanographene and regular graphite. If any TPymT adsorbs to the graphite or reacts with it, it will appear as an obvious increase in N content because graphite has a very weak nitrogen signal. A summary of the EDAX data can be found in Figure 34. It can be seen that the graphite samples have little to no nitrogen. TPymT was tested by itself and had an atomic nitrogen percent of 42% which matched its theoretical atomic percent of 41%. Cyanographene started with 10% atomic nitrogen and was increased to 16% after the reaction with CyPy. This confirms the reaction was successful, and that BPT graphene was synthesized.

In future experiments we hope to chelate metals to the chemically modified graphene and sue it for catalysis. With such a strong metal ligand, we expect high mass loadings will be achieved due to the high degree of functionalization of the graphene.

5.4 Conclusion

Chemically modified graphene has the potential to be used as a catalyst scaffold for single metal atoms. In this work, we synthesized a 2,4-bis(2-pyrimidyl)-1,3,5-triazine (BPT) group covalently bound to graphene. This was achieved through a multistep process. First, fluorographite was used as the starting precursor and was reacted with sodium cyanide to create cyano functionalized graphene (CyG). Next, the CyG was reacted with 2-cyanopyrimidine in a nitrile trimerization reaction to covalently bind a BPT group to the graphene surface. The materials were characterized through various methods including FTIR, SEM, XRD, and EDAX. We hope to utilize this new chemically modified graphene to chelate metals for use in catalysis. With a high degree of functionalization, we expect high catalyst loading in the final product. We hope that the BPT graphene will lead to other similar materials in hopes of creating high loading single metal atom catalysts.

CHAPTER 6: CATALYZING LITHIUM SULFUR REACTIONS FOR HIGH RATE CONVERSION BATTERIES

6.1 Introduction

One of the biggest challenges facing modern society is energy storage. There is an inability to store a large amount of energy in a confined space, which directly hinders the advancement of many areas of science and life. This is especially noticeable in renewable energy generation, transportation, and portable electronics.

Today's current technology, the Li-Ion battery, has a modest specific capacity of ~300 mAh/g. However, lithium sulfur batteries have up to 5 times that capacity, with a theoretical specific capacity of 1675 mAh/g. An increase in capacity of this magnitude would dramatically increase the viability of technologies that are on the verge of mass commercialization but, are anchored in public doubt due to lack of high capacity storage. This is essential for electric vehicles as the major setback is a small driving range per charge. For renewable energy it would allow for the storage of energy generated at peak hours and the release of that energy at peak demand.

However, lithium sulfur batteries suffer from a multitude of problems; two of which are low cycle life (how many times you can charge and discharge) and poor rate capability (how quickly you can charge and discharge). The major cause of this problem is a phenomenon called polysulfide shuttling. This is when intermediates (lithium polysulfides) of the lithium-sulfur reaction are generated at the cathode and diffuse across the battery. These intermediates are soluble in the electrolyte which cause loss of active material in the cathode and can create a passivating layer on the surface of the lithium metal used in the cell.[41,43]

To combat this, many different approaches have been taken. These include physical sorption techniques ranging from porous materials, metal oxides, physical barriers, electrolyte additives, and more. One area that has not been fully investigated is the use of catalysts in lithium sulfur batteries.

In this work, a novel catalyst testing method utilizing polysulfide catholyte was developed for analyzing catalyst effectiveness for polysulfide oxidation and reduction reactions. Single metal atom catalysts hosted on reduced graphene oxide were tested and analyzed. Various metals were tested as catalysts for the polysulfide reactions, and it was found the platinum and manganese enhance polysulfide reaction kinetics.

6.2 Experimental

Graphene oxide was made via modified hummers method.[36] Briefly, 6 grams of graphite powder was added to 140 mL of sulfuric acid. The reaction mixture was cooled to 0 °C, while 3 g of NaNO and 18 g of $KMnO_4$ was added slowly under vigorous stirring. The reaction was then heated to 40 °C for 6 hours. Next, 500 mL of water was added. The resulting solution was washed and centrifuged with water until pH 7. It was then purified by dialysis for 2 weeks to remove any impurities. Holey graphene oxide was made by mixing 2 mL of 30% hydrogen peroxide with 50 mL of 2 mg/mL graphene oxide. After 20 minutes the reaction mixture was washed with DI water and centrifugation three times.

To prepare catalysts samples, reduced graphene oxide hydrogels were synthesized in the presence of metal precursors. GO was added to an autoclave with select amounts of metal chloride precursor (ranging from 0.5 - 2% by weight) and heated to 180 °C for 2 hours. The same was done

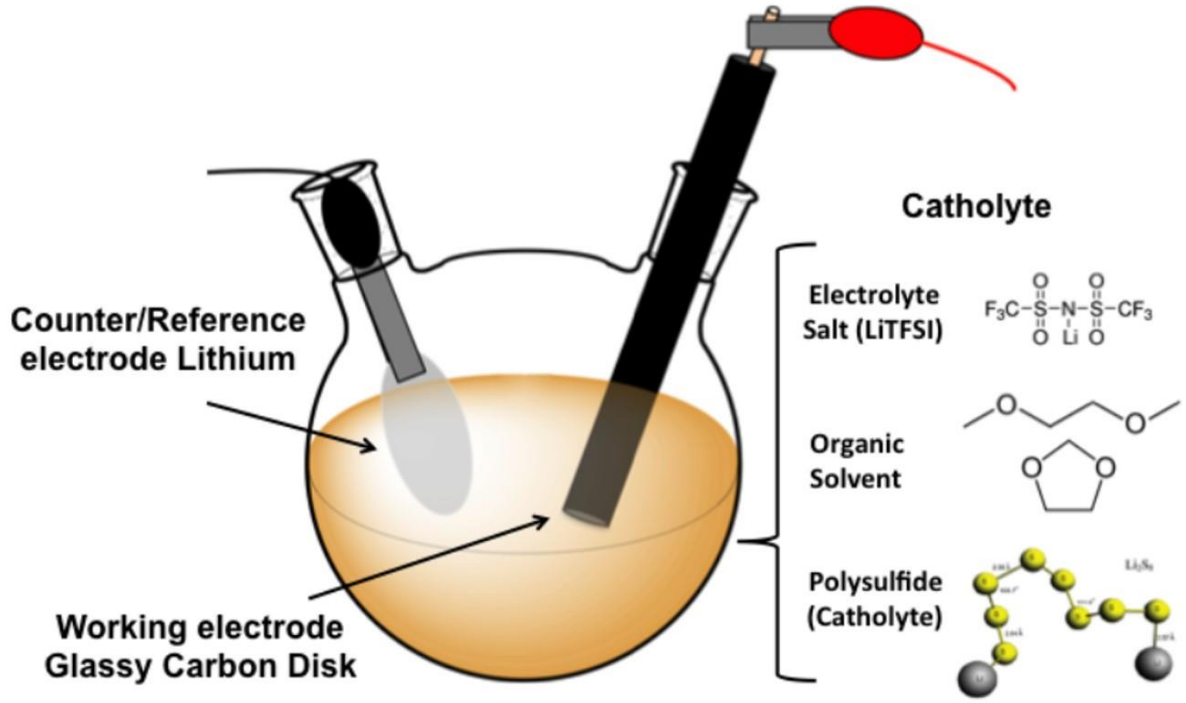

Figure 35. The catalyst testing set-up consisted of a catholyte comprised of a common lithium sulfur battery electrolyte mixed with lithium polysulfides.

for holey graphene oxide samples. Nitrogen doped samples were annealed at 900 °C in ammonia for 2 hours.

Lithium polysulfide catholyte was a prepared for catalyst testing. First, the electrolyte solution was made my mixing 1,3-dioxolane (DOL) and dimethoxyethane (DME) in a 1:1 volume ratio. Then, the appropriate amount of Bis(trifluoromethane)sulfonimide lithium salt (LiTFSI) was added to make the solution 1 M LiTFSI. To stabilize the SEI formed during cycling 1% wt $LiNO_3$ was added. Finally, lithium polysulfides (Li_2S_8) were added by adding stoichiometric amounts of elemental sulfur and Li_2S to the solution and heating to 90 °C. The testing apparatus is outlined in Figure 35. Catalyst samples were first sonicated to disperse them into solution in the presence of 2 wt% polyvinylidene Fluoride (PVDF) or 2 wt% polytetrafluoroethylene (PTFE) binders. They were then dropcast on a glassy carbon electrode which acted as the working electrode and

immersed in the catholyte solution. A Li- metal counter/reference electrode was used to simulate a battery-like environment.

Batteries were prepared with the free standing rGO hydrogels containing catalysts. Coin cell were prepared (size 2032) with stainless steel current collectors with a few drops of catholyte electrode on each electrode.

6.3 Results & Discussion

In our experiments multiple substrates with various catalysts were testing for their electrochemical performance. In order to probe their performance quickly a catholyte testing system was developed. In the setup, polysulfides are synthesized in order to measure the catalytic

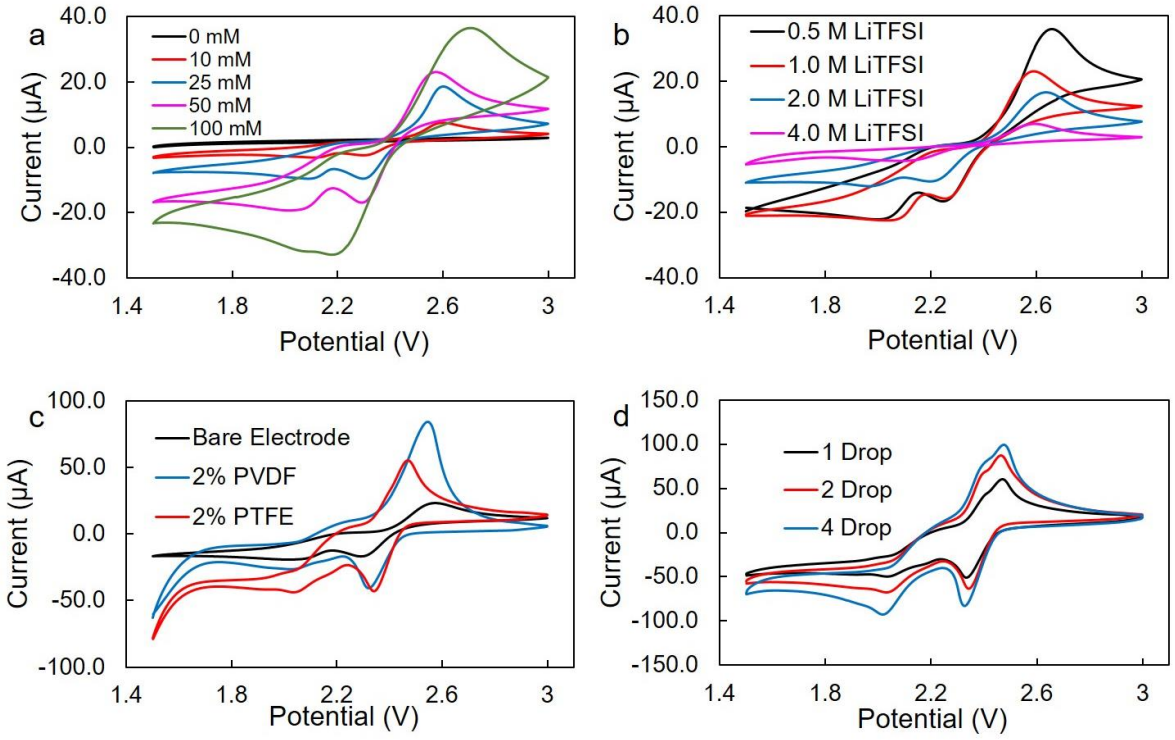

Figure 36. Cyclic voltammetry of (a) polysulfide concentration effect on peak position, (b) LiTFSI concentration on peak position, (c) binder effect on peak position, and (d) mass loading effect on peak position.

properties directly. Normally, under standard operation conditions polysulfides take many cycles to leech into the electrode. By synthesizing them directly, we put the reactant of interest in direct contact with the catalyst. By measuring the peak separation during cyclic voltammetry measurements, the kinetics of the reaction can be probed.[91] A smaller separation of peaks signifies a smaller kinetic barrier, and thus increased reaction speed. This method is very common in catalysis, used frequently in HER and ORR reactions.[92,93] However, this electrolyte system had to be meticulously optimized in order to achieve the best reproducibility possible. Many factors can shift the CV peaks so care must be taken in order to isolate only the variable of interest.

During experiments it was found that a polysulfide concentration of 50 mM gave the most kinetically favorable reaction conditions with a peak separation of 0.282 V (Figure 36a). LiTFSI concentrations for optimal performance matched those of literature, with 1.0 M yielding the most favorable reaction kinetics with a peak separation of 0.335 V (Figure 36b). Binder is another

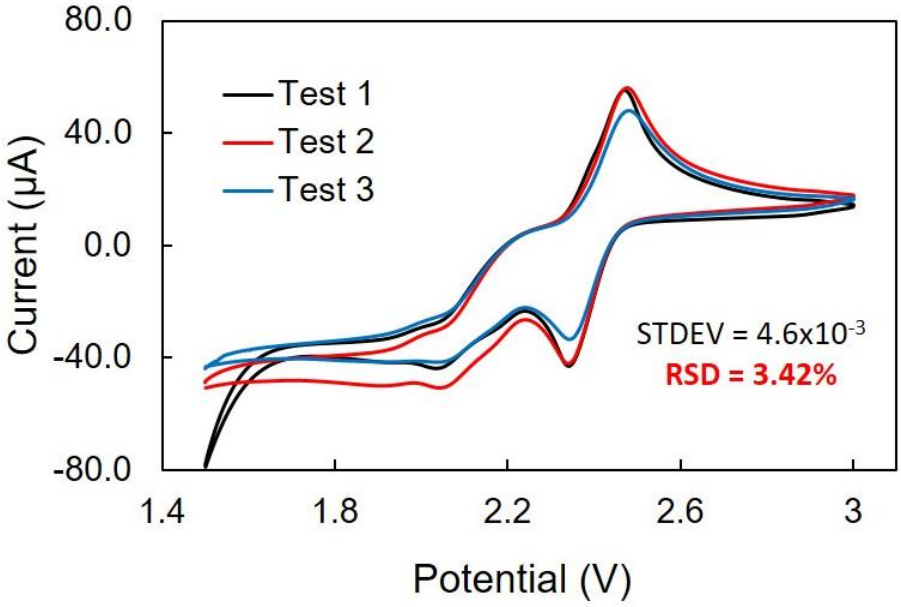

Figure 37. Raw CV data for 3 separate trials. Trial 2 was taken with a different glassy carbon electrode, and Trial 3 was done on a separate day. With a standard deviation of 3.42%, the testing method was quite precise.

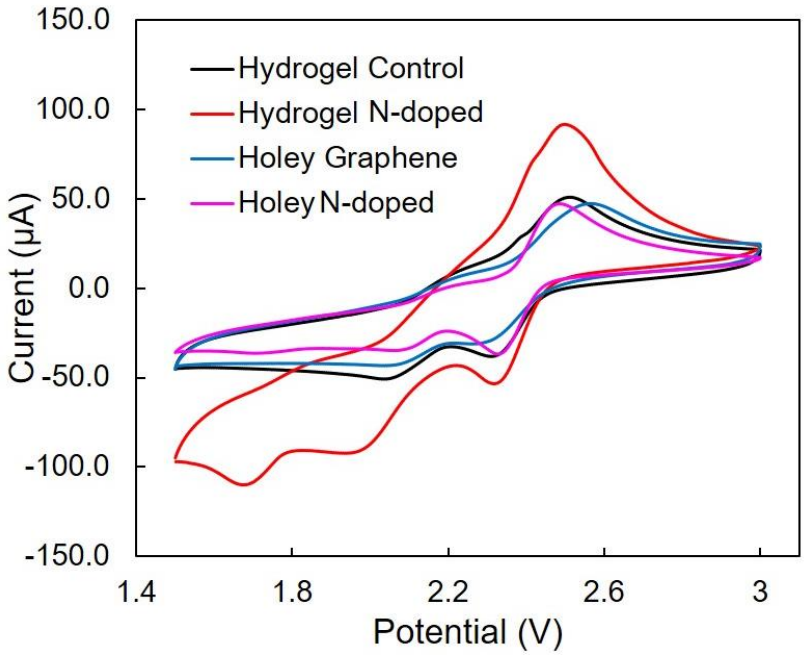

Figure 38. Substrates were tested for catalytic performance. Holey N-doped reduced graphene oxide lowest overpotential and was chose for metal catalyst tests.

crucial component to the catholyte set-up. Both PVDF and PTFE are used regularly in battery fabrication so each was tested. PTFE appeared to facilitate the best reaction kinetics with a CV peak separation of only 0.128 V ((Figure 36c). Lastly, the mass loading was probed for optimal conditions. It was found that 2 drops of catalyst (corresponding to a loading of ~ 0.25 mg/cm^2) had the smallest peak separation of 0.121 V (Figure 36d).

The reproducibility of the optimized electrode was investigated to ensure precision measurements. Trial one was performed normally, Trial 2 was taken on a different glassy carbon electrode, and Trial 3 was taken on a separate day (Figure 37). These measurements ensured reproducibility in measurements, and even miniscule changes in peak position can be attributed to catalytic activity.

The effect of the type of reduced graphene oxide used as the substrate was also investigated. Three different types of rGO was used; regular, N-doped, and holey. Figure 38 summarizes the

substrate effect on the device overpotential. When graphene is exposed to hydrogen peroxide nano sized holes form on the surface. This enhances diffusion throughout the electrode, however it degrades the structure.[19] This degradation caused the holey graphene to have worse performance compared to the non-holey rGO, with overpotentials of 0.283 V and 0.200 V respectively. Upon N-doping the samples overpotential drop dramatically. The rGO hydrogel overpotential lowers to 0.177 V while the holey rGO overpotential drops to 0.158 V. This is most likely due to the rearrangement of atoms on the graphene surface at high temperatures affording higher conductivity.[31] In the holey samples, the annealing effect is much more pronounced due to the defect rich surface of the holey GO.

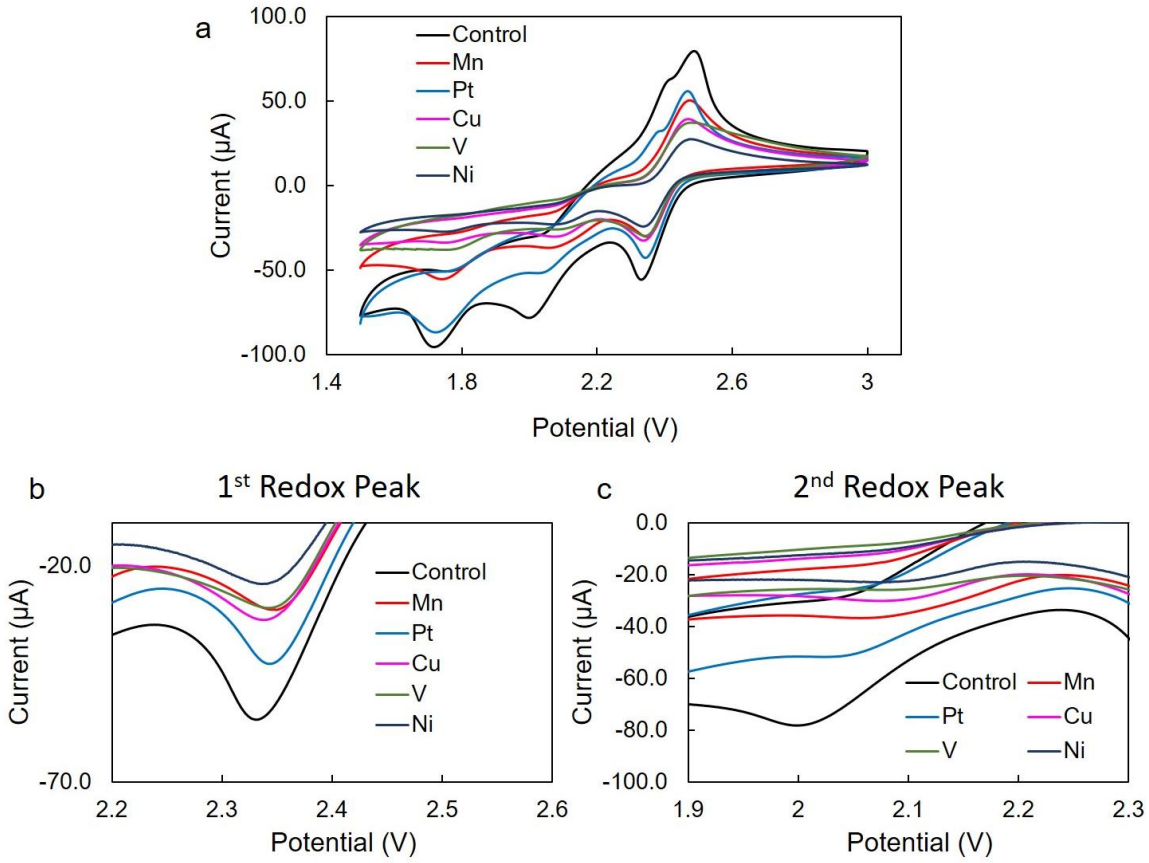

Figure 39. CV of various metal catalysts synthesized at 2% by weight metal at 5 mV/s. (a) Comparison over the entire CV scan of Mn, Pt, Cu, V, and Ni catalysts. (b) The initial reaction peak of elemental sulfur to polysulfide occurs from 2.3 – 2.4 V. (c) Polysulfide reduction to Li_2S occurs from 2 – 2.2 V.

With optimized reaction conditions and substrates, various catalysts were prepared by mixing holey GO with metal chloride salts (2% by weight), and annealing them in ammonia. We suspect that the catalyst samples are single metal atom catalysts due to the similar reaction conditions found in literature.[35] However, typical characterization is difficult to do by traditional means requiring powerful imaging to see the single atom sites. We hope to analyze the structures in the future with STEM and EXAFS. For electrochemical characterization each sample was compared against a control to access the catalysts performance.

Figure 39a summarizes the CVs obtained for various metals including Mn, Pt, Cu, V, and Ni. The peak around 2.5 V is the anodic peak, signifying the charging reaction of lithium

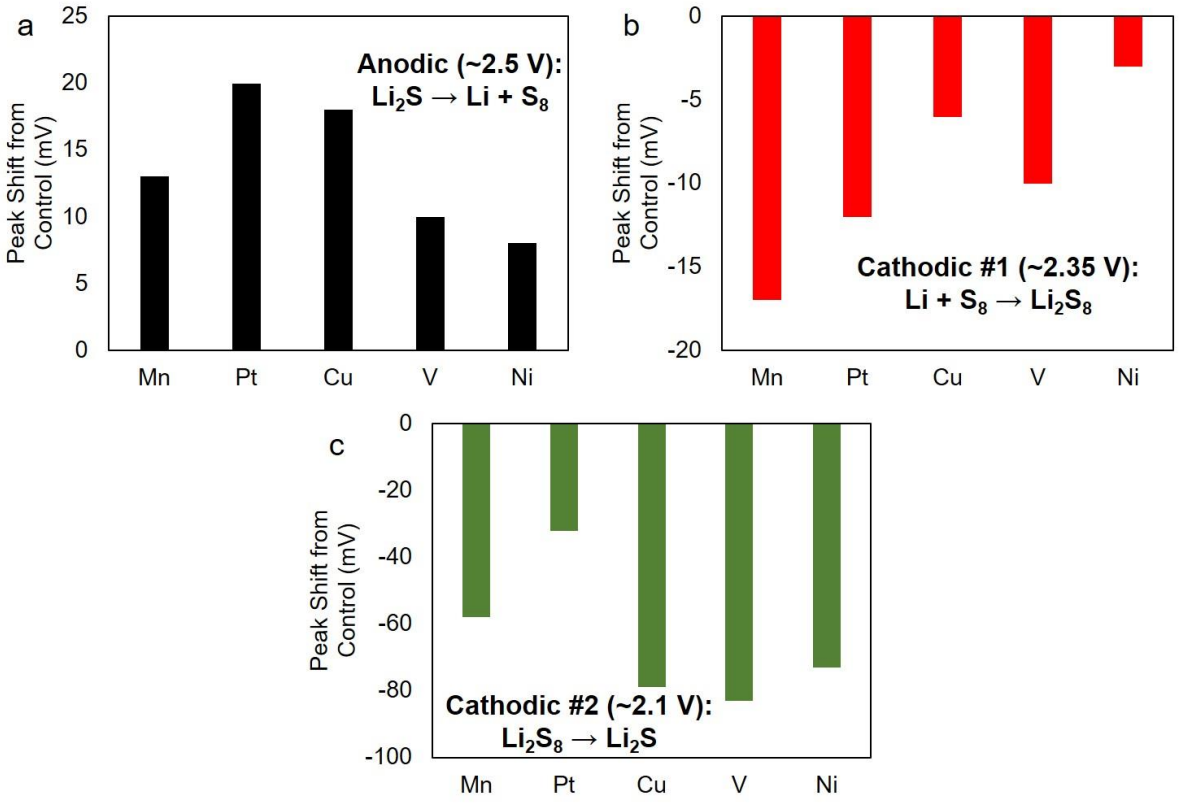

Figure 40. The potential difference for each redox peak from the control holey N-doped holey rGO hydrogel. (a) Pt is the best catalyst for the formation of the charge product, S_8. (b) Mn has the highest performance for the conversion of S_8 to the first discharge product Li_2S_8. (c) V provides the best catalyst for the reduction of high order polysulfides to the final discharge product Li_2S.

polysulfide to elemental sulfur and lithium metal. On the catholic side, the first peak signifies the reduction of S_8 by lithium forming high order polysulfides (Figure 39b). The next peak is the further reduction of high order polysulfides to lower order polysulfides, and finally to the final discharge product Li_2S (Figure 39c). These peaks can be quantitatively analyzed to see which catalyst had the highest performance.

The most interesting result obtained, was that multiple catalysts had the *best* performance, depending on which peak is analyzed. For the anodic reaction of Li_2S back to Li and S_8, Pt has the lowest overpotential compared to the control with a value of 20 mV followed closely by Cu at 18 mV. The first cathodic peak, the reduction of S_8 to high order polysulfides, is catalyzed most effectively by Manganese by a large margin at -17 mV vs the control. The final cathodic peak at ~2.1 V is the reduction of polysulfides to the final discharge product Li_2S. The reaction is most effectively catalyzed by V, Cu, and Ni with overpotentials vs the control of -83, -79, and -73 mV respectively. The data presented points at a very interesting conclusion – different catalysts are better at catalyzing different lithium sulfur reactions. Future work with bimetallic catalysts may be explored to attain synergistic effects in LSBs. Using this data, we focused on a few catalysts to explore further, Pt and Mn.

The cycle life of a battery was tested using single metal atom platinum or manganese holey N-doped reduced graphene oxide (Figure 41). The control battery had modest capacity of 673 mAh/g and ater 50 cycles dropped to 539 mAh/g, a 80% capacity retention. The observed capacity drop off is common among lithium sulfur batteries and is to be expected. When Mn and Pt was introduced the capacities and retention rate increased dramatically. For Mn, the starting capacity was 848 mAh/g and dropped to 662 mAh/g after 50 cycles. This capacity retention of 78% can be explained by the reaction that Mn promotes the most effectively, the transformation of S_8 to

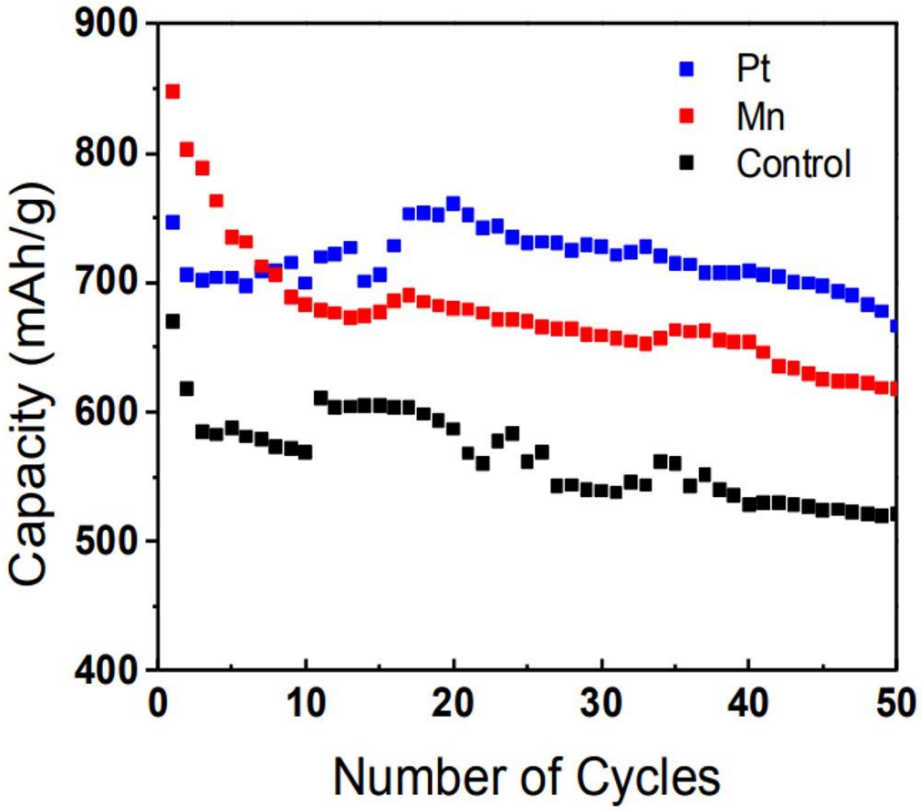

Figure 41. Battery cycling data at 0.1 C for the single metal atom catalyst containing Mn or Pt compared against a control with no catalyst. Pt and Mn significantly outperform the control.

polysulfides. The catalysis of this particular reaction actually means that there are more polysulfides produced, effectively shortening battery life. The opposite is true for Pt. The Pt battery starts with a capacity of 745 mAh/g, and only drops to 692 after 50 cycles. The 93% capacity retention rate is most likely due to the fact that Pt is the best catalyst for the anodic reaction, effectively reducing the total amount of polysulfides in the system upon charging. More experiments are needed to explain all the results seen and bimetallic experiments are of high interest. The work shows very promising results for the future of understanding and using lithium sulfur batteries.

6.4 Conclusion

Catalysts for polysulfide oxidation and reduction reactions were created and analyzed using a novel catholyte testing method. By using a catholyte, lithium polysulfides can be directly reacted on the electrode surface to analyze the reaction kinetics. The method has the potential to streamline catalyst testing and offers a fast method for screening. Holey N-doped reduced graphene oxide was used as the substrate to host various metal catalysts due to its conductivity, flexibility, and favorable interaction with potential catalysts. It was found that different metals catalyzed different steps in the lithium sulfur discharge/charge process. Pt was found to catalyze the anodic reaction the most effectively resulting in a battery with an excellent capacity retention of 93% over 50 cycles at 0.1 C. Mn catalysts appeared promising in testing, and had the lowest overpotential for the reduction of S_8 to high order polysulfides. However, it had a 78% capacity retention after 50 cycles at 0.1C, 2% lower than the control. This gives valuable insight into the parameters that need to be optimized to achieve the best battery performance possible. By catalyzing the right sulfur redox reactions, the battery chemistry can be controlled to give a device with high cycle life and capacity.

REFERENCES

(1) Winter, M.; Brodd, R. J. What Are Batteries, Fuel Cells, and Supercapacitors? *Chem. Rev.* **2004**, *104* (10), 4245–4269. https://doi.org/10.1021/cr020730k.

(2) Ockwig, N. W.; Co, A. P.; Keeffe, M. O.; Matzger, A. J.; Yaghi, O. M. Porous , Crystalline , Covalent Organic Frameworks. **2005**, *310* (November), 1166–1171.

(3) Ding, S. Y.; Wang, W. Covalent Organic Frameworks (COFs): From Design to Applications. *Chem. Soc. Rev.* **2013**, *42* (2), 548–568. https://doi.org/10.1039/c2cs35072f.

(4) Yaghi, Omar M., Adrien P. Coˆte, Annabelle I. Benin, N. W. O.; Yaghi, O. M.; Adrien P. Cote´, Annabelle I. Benin, Nathan W. Ockwig, Michael O'Keeffe, Adam J. Matzger, O. M. Y. Porous , Crystalline , Covalent Organic Frameworks. **2005**, *1166* (2005), 1166–1171. https://doi.org/10.1126/science.1120411.

(5) Liu, M.; Guo, L.; Jin, S.; Tan, B. Covalent Triazine Frameworks: Synthesis and Applications. *J. Mater. Chem. A* **2019**, *7* (10), 5153–5172. https://doi.org/10.1039/c8ta12442f.

(6) Xu, Q.; Tang, Y.; Zhai, L.; Chen, Q.; Jiang, D. Pyrolysis of Covalent Organic Frameworks: A General Strategy for Template Converting Conventional Skeletons into Conducting Microporous Carbons for High-Performance Energy Storage. *Chem. Commun.* **2017**, *53* (85), 11690–11693. https://doi.org/10.1039/c7cc07002k.

(7) Kuhn, P.; Antonietti, M.; Thomas, A. Porous, Covalent Triazine-Based Frameworks Prepared by Ionothermal Synthesis**. https://doi.org/10.1002/anie.200705710.

(8) Zhu, X.; Tian, C.; Mahurin, S. M.; Chai, S. H.; Wang, C.; Brown, S.; Veith, G. M.; Luo, H.; Liu, H.; Dai, S. A Superacid-Catalyzed Synthesis of Porous Membranes Based on Triazine Frameworks for CO 2 Separation. *J. Am. Chem. Soc.* **2012**, *134* (25), 10478–10484. https://doi.org/10.1021/ja304879c.

(9) Puthiaraj, P.; Cho, S. M.; Lee, Y. R.; Ahn, W. S. Microporous Covalent Triazine Polymers: Efficient Friedel-Crafts Synthesis and Adsorption/Storage of CO2 and CH4. *J. Mater. Chem. A* **2015**, *3* (13), 6792–6797. https://doi.org/10.1039/c5ta00665a.

(10) Kamiya, K.; Kamai, R.; Hashimoto, K.; Nakanishi, S. Platinum-Modified Covalent Triazine Frameworks Hybridized with Carbon Nanoparticles as Methanol-Tolerant Oxygen Reduction Electrocatalysts. *Nat. Commun.* **2014**, *5* (May), 1–6. https://doi.org/10.1038/ncomms6040.

(11) Chan-Thaw, C. E.; Villa, A.; Katekomol, P.; Su, D.; Thomas, A.; Prati, L. Covalent Triazine Framework as Catalytic Support for Liquid Phase Reaction. *Nano Lett.* **2010**, *10* (2), 537–541. https://doi.org/10.1021/nl904082k.

(12) Wang, M.; Guo, H.; Xue, R.; Li, Q.; Liu, H.; Wu, N.; Yao, W.; Yang, W. Covalent Organic Frameworks: A New Class of Porous Organic Frameworks for Supercapacitor Electrodes. *ChemElectroChem* **2019**, *6* (12), 2984–2997. https://doi.org/10.1002/celc.201900298.

(13) Hao, L.; Ning, J.; Luo, B.; Wang, B.; Zhang, Y.; Tang, Z.; Yang, J.; Thomas, A.; Zhi, L. Structural Evolution of 2D Microporous Covalent Triazine-Based Framework toward the Study of High-Performance Supercapacitors. *J. Am. Chem. Soc.* **2015**. https://doi.org/10.1021/ja508693y.

(14) Su, B.-L.; Sanchez, C.; Yang, X.-Y. Insights into Hierarchically Structured Porous Materials: From Nanoscience to Catalysis, Separation, Optics, Energy, and Life Science. In *Hierarchically Structured Porous Materials*; Wiley-VCH Verlag GmbH & Co. KGaA: Weinheim, Germany, 2011; pp 1–27. https://doi.org/10.1002/9783527639588.ch1.

(15) Sun, H.; Zhu, J.; Baumann, D.; Peng, L.; Xu, Y.; Shakir, I.; Huang, Y.; Duan, X. Hierarchical 3D Electrodes for Electrochemical Energy Storage. *Nat. Rev. Mater.* **2019**, *4* (1), 45–60. https://doi.org/10.1038/s41578-018-0069-9.

(16) Liu, T.; Zhang, F.; Song, Y.; Li, Y. Revitalizing Carbon Supercapacitor Electrodes with Hierarchical Porous Structures. *J. Mater. Chem. A* **2017**, *5* (34), 17705–17733. https://doi.org/10.1039/c7ta05646j.

(17) Bai, R.; Song, Y.; Li, Y.; Yu, J. Creating Hierarchical Pores in Zeolite Catalysts. *Trends Chem.* **2019**, *1* (6), 601–611. https://doi.org/10.1016/j.trechm.2019.05.010.

(18) Gogotsi, Y.; Simon, P. True Performance Metrics in Electrochemical Energy Storage. *Science (80-.).* **2011**, *334* (6058), 917–918. https://doi.org/10.1126/science.1213003.

(19) Xu, Y.; Lin, Z.; Zhong, X.; Huang, X.; Weiss, N. O.; Huang, Y.; Duan, X. Holey Graphene Frameworks for Highly Efficient Capacitive Energy Storage. *Nat. Commun.* **2014**, *5*. https://doi.org/10.1038/ncomms5554.

(20) Lei, C.; Lekakou, C. Carbon-Based Nanocomposite EDLC Supercapacitors. *Nanotechnol. 2010 Adv. Mater. CNTs, Part. Film. Compos.* **2016**, *1*, 176–179.

(21) Lu, Q.; Chen, J. G.; Xiao, J. Q. Nanostructured Electrodes for High-Performance Pseudocapacitors. *Angew. Chemie - Int. Ed.* **2013**, *52* (7), 1882–1889. https://doi.org/10.1002/anie.201203201.

(22) Cherusseri, J.; Sambath Kumar, K.; Choudhary, N.; Nagaiah, N.; Jung, Y.; Roy, T.; Thomas, J. Novel Mesoporous Electrode Materials for Symmetric, Asymmetric and Hybrid Supercapacitors. *Nanotechnology* **2019**, *30* (20). https://doi.org/10.1088/1361-6528/ab0685.

(23) González, A.; Goikolea, E.; Barrena, J. A.; Mysyk, R. Review on Supercapacitors: Technologies and Materials. *Renew. Sustain. Energy Rev.* **2016**, *58*, 1189–1206. https://doi.org/10.1016/j.rser.2015.12.249.

(24) Zhong, C.; Deng, Y.; Hu, W.; Qiao, J.; Zhang, L.; Zhang, J. Chem Soc Rev A Review of Electrolyte Materials and Compositions for Electrochemical Supercapacitors. *Chem. Soc. Rev. Chem. Soc. Rev* **2015**, *44* (44), 7431–7920.

(25) Pandolfo, A. G.; Hollenkamp, A. F. Carbon Properties and Their Role in Supercapacitors. *J. Power Sources* **2006**, *157* (1), 11–27. https://doi.org/10.1016/j.jpowsour.2006.02.065.

(26) Ramachandran, R.; Wang, F. Electrochemical Capacitor Performance: Influence of

Aqueous Electrolytes. In *Supercapacitors - Theoretical and Practical Solutions*; InTech, 2018. https://doi.org/10.5772/intechopen.70694.

(27) Demarconnay, L.; Raymundo-Piñero, E.; Béguin, F. A Symmetric Carbon/Carbon Supercapacitor Operating at 1.6 v by Using a Neutral Aqueous Solution. *Electrochem. commun.* **2010**, *12* (10), 1275–1278. https://doi.org/10.1016/j.elecom.2010.06.036.

(28) Béguin, F.; Presser, V.; Balducci, A.; Frackowiak, E. Carbons and Electrolytes for Advanced Supercapacitors. *Adv. Mater.* **2014**, *26* (14), 2219–2251. https://doi.org/10.1002/adma.201304137.

(29) Eftekhari, A. Supercapacitors Utilising Ionic Liquids. *Energy Storage Mater.* **2017**, *9*, 47–69. https://doi.org/10.1016/j.ensm.2017.06.009.

(30) Liu, J.; Tang, J.; Gooding, J. J. Strategies for Chemical Modification of Graphene and Applications of Chemically Modified Graphene. *J. Mater. Chem.* **2012**, *22* (25), 12435–12452. https://doi.org/10.1039/c2jm31218b.

(31) Smith, A. T.; LaChance, A. M.; Zeng, S.; Liu, B.; Sun, L. Synthesis, Properties, and Applications of Graphene Oxide/Reduced Graphene Oxide and Their Nanocomposites. *Nano Mater. Sci.* **2019**, *1* (1), 31–47. https://doi.org/10.1016/j.nanoms.2019.02.004.

(32) Yu, W.; Sisi, L.; Haiyan, Y.; Jie, L. Progress in the Functional Modification of Graphene/Graphene Oxide: A Review. *RSC Adv.* **2020**, *10* (26), 15328–15345. https://doi.org/10.1039/d0ra01068e.

(33) Kuila, T.; Bose, S.; Mishra, A. K.; Khanra, P.; Kim, N. H.; Lee, J. H. Chemical Functionalization of Graphene and Its Applications. *Prog. Mater. Sci.* **2012**, *57* (7), 1061–1105. https://doi.org/10.1016/j.pmatsci.2012.03.002.

(34) Terrones, M.; Martín, O.; González, M.; Pozuelo, J.; Serrano, B.; Cabanelas, J. C.; Vega-Díaz, S. M.; Baselga, J. Interphases in Graphene Polymer-Based Nanocomposites: Achievements and Challenges. *Advanced Materials*. 2011, pp 5302–5310. https://doi.org/10.1002/adma.201102036.

(35) Fei, H.; Dong, J.; Chen, D.; Hu, T.; Duan, X.; Shakir, I.; Huang, Y.; Duan, X. Single Atom Electrocatalysts Supported on Graphene or Graphene-like Carbons. *Chem. Soc. Rev.* **2019**, *48* (20), 5207–5241. https://doi.org/10.1039/c9cs00422j.

(36) Hummers, W. S.; Offeman, R. E. Preparation of Graphitic Oxide. *J. Am. Chem. Soc.* **1958**, *80* (6), 1339. https://doi.org/10.1021/ja01539a017.

(37) Chronopoulos, D. D.; Bakandritsos, A.; Pykal, M.; Zbořil, R.; Otyepka, M. Chemistry, Properties, and Applications of Fluorographene. *Appl. Mater. Today* **2017**, *9*, 60–70. https://doi.org/10.1016/j.apmt.2017.05.004.

(38) Nitta, N.; Wu, F.; Lee, J. T.; Yushin, G. Li-Ion Battery Materials: Present and Future. *Mater. Today* **2015**, *18* (5), 252–264. https://doi.org/10.1016/j.mattod.2014.10.040.

(39) Zheng, D.; Zhang, X.; Wang, J.; Qu, D.; Yang, X.; Qu, D. Reduction Mechanism of Sulfur in Lithium-Sulfur Battery: From Elemental Sulfur to Polysulfide. *J. Power Sources* **2016**, *301*, 312–316. https://doi.org/10.1016/j.jpowsour.2015.10.002.

(40) Chen, H.; Wang, C.; Dong, W.; Lu, W.; Du, Z.; Chen, L. Monodispersed Sulfur Nanoparticles for Lithium–Sulfur Batteries with Theoretical Performance. *Nano Lett.* **2015**, *15* (1), 798–802. https://doi.org/10.1021/nl504963e.

(41) Fang, X.; Peng, H. A Revolution in Electrodes: Recent Progress in Rechargeable Lithium-Sulfur Batteries. *Small* **2015**, *11* (13), 1488–1511. https://doi.org/10.1002/smll.201402354.

(42) Zhou, W.; Yu, Y.; Chen, H.; Disalvo, F. J.; Abruña, H. D. Yolk-Shell Structure of Polyaniline-Coated Sulfur for Lithium-Sulfur Batteries. *J. Am. Chem. Soc.* **2013**, *135* (44), 16736–16743. https://doi.org/10.1021/ja409508q.

(43) Li, G.; Wang, S.; Zhang, Y.; Li, M.; Chen, Z.; Lu, J. Revisiting the Role of Polysulfides in Lithium–Sulfur Batteries. *Adv. Mater.* **2018**, *30* (22), 1–19. https://doi.org/10.1002/adma.201705590.

(44) Su, Y. S.; Fu, Y.; Cochell, T.; Manthiram, A. A Strategic Approach to Recharging Lithium-Sulphur Batteries for Long Cycle Life. *Nat. Commun.* **2013**, *4*. https://doi.org/10.1038/ncomms3985.

(45) Lei, T.; Chen, W.; Lv, W.; Huang, J.; Zhu, J.; Chu, J.; Yan, C.; Wu, C.; Yan, Y.; He, W.; et al. Inhibiting Polysulfide Shuttling with a Graphene Composite Separator for Highly Robust Lithium-Sulfur Batteries. *Joule* **2018**, *2* (10), 2091–2104. https://doi.org/10.1016/j.joule.2018.07.022.

(46) Song, J.; Xu, T.; Gordin, M.; Zhu, P.; Lv, D.; Jiang, Y.-B.; Chen, Y.; Duan, Y.; Wang, D. Nitrogen-Doped Mesoporous Carbon Promoted Chemical Adsorption of Sulfur and Fabrication of High-Areal-Capacity Sulfur Cathode with Exceptional Cycling Stability for Lithium-Sulfur Batteries. *ECS Meet. Abstr.* **2014**. https://doi.org/10.1149/MA2014-01/2/182.

(47) Yuan, Z.; Peng, H.-J.; Hou, T.-Z.; Huang, J.-Q.; Chen, C.-M.; Wang, D.-W.; Cheng, X.-B.; Wei, F.; Zhang, Q. Powering Lithium–Sulfur Battery Performance by Propelling Polysulfide Redox at Sulfiphilic Hosts. *Nano Lett.* **2016**, *16* (1), 519–527. https://doi.org/10.1021/acs.nanolett.5b04166.

(48) Kuhn, P.; Antonietti, M.; Thomas, A. Porous, Covalent Triazine-Based Frameworks Prepared by Ionothermal Synthesis. *Angew. Chemie - Int. Ed.* **2008**, *47* (18), 3450–3453. https://doi.org/10.1002/anie.200705710.

(49) Kuhn, P.; Thomas, A.; Antonietti, M. Toward Tailorable Porous Organic Polymer Networks: A High-Temperature Dynamic Polymerization Scheme Based on Aromatic Nitriles. *Macromolecules* **2009**. https://doi.org/10.1021/ma802322j.

(50) SING, K. S. W.; EVERETT, D. H.; HAUL, R. A. W.; MOSCOU, L.; PIEROTTI, R. A.; ROUQUEROL, J.; SIEMIENIEWSKA, T. REPORTING PHYSISORPTION DATA FOR GAS/SOLID SYSTEMS with Special Reference to the Determination of Surface Area and Porosity. *Pure Appl. Chem.* **1985**, *57* (4), 603–619. https://doi.org/10.1351/pac198557040603.

(51) Kuhn, P.; Su, D.; Thomas, A. From Microporous Regular Frameworks to Mesoporous

Materials with Ultrahigh Surface Area: Dynamic Reorganization of Porous Polymer Networks. *J. Am. Chem. Soc.* **2008**, *130* (40), 13333–13337. https://doi.org/10.1021/ja803708s.

(52) Artz, J.; Delidovich, I.; Pilaski, M.; Niemeier, J.; Kübber, B. M.; Rahimi, K.; Palkovits, R. Sulfonated Covalent Triazine-Based Frameworks as Catalysts for the Hydrolysis of Cellobiose to Glucose. *RSC Adv.* **2018**, *8* (40), 22392–22401. https://doi.org/10.1039/c8ra04254c.

(53) Schwan, J.; Ulrich, S.; Batori, V.; Ehrhardt, H.; Silva, S. R. P. Raman Spectroscopy on Amorphous Carbon Films. *J. Appl. Phys.* **1996**, *80* (1), 440–447. https://doi.org/10.1063/1.362745.

(54) Ferrari, A. C. Raman Spectroscopy of Graphene and Graphite: Disorder, Electron-Phonon Coupling, Doping and Nonadiabatic Effects. *Solid State Commun.* **2007**, *143* (1–2), 47–57. https://doi.org/10.1016/j.ssc.2007.03.052.

(55) Zhang, X. Q.; Dong, W.; Lu, A. H.; Li, W. C. Rational Design of Mesoporous Carbon Electrodes with High Mass Loading for Binder-Free Supercapacitors. *Energy Technol.* **2015**, *3* (3), 234–241. https://doi.org/10.1002/ente.201402161.

(56) Deng, Y.; Xie, Y.; Zou, K.; Ji, X. Review on Recent Advances in Nitrogen-Doped Carbons: Preparations and Applications in Supercapacitors. *J. Mater. Chem. A* **2015**, *4* (4), 1144–1173. https://doi.org/10.1039/c5ta08620e.

(57) Zhong, S.; Zhan, C.; Cao, D. Zeolitic Imidazolate Framework-Derived Nitrogen-Doped Porous Carbons as High Performance Supercapacitor Electrode Materials. *Carbon N. Y.* **2015**, *85*, 51–59. https://doi.org/10.1016/j.carbon.2014.12.064.

(58) Ni, M.; Huang, Z.; Zhang, X.; Liu, J.; Qiao, L.; Yang, W. Hierarchical Design of Nitrogen-Doped Porous Carbon Nanorods for Use in High Efficiency Capacitive Energy Storage. *RSC Adv.* **2017**, *7* (36), 22447–22453. https://doi.org/10.1039/c7ra02425h.

(59) Kim, B. K.; Sy, S.; Yu, A.; Zhang, J. Electrochemical Supercapacitors for Energy Storage and Conversion. *Handb. Clean Energy Syst.* **2014**, 1–25. https://doi.org/10.1002/9781118991978.hces112.

(60) Eftekhari, A. Supercapacitors Utilising Ionic Liquids. *Energy Storage Mater.* **2017**, *9*, 47–69. https://doi.org/10.1016/j.ensm.2017.06.009.

(61) Chang, L.; Sun, K.; Hu, Y. H. New Chemistry for New Material: Highly Dense Mesoporous Carbon Electrode for Supercapacitors with High Areal Capacitance. *ACS Appl. Mater. Interfaces* **2018**, *10* (39), 33162–33169. https://doi.org/10.1021/acsami.8b09661.

(62) Feng, X.; Ding, X.; Jiang, D. Covalent Organic Frameworksw. *Chem. Soc. Rev. Chem. Soc. Rev* **2012**, *41* (41), 6010–6022. https://doi.org/10.1039/c2cs35157a.

(63) Kim, D. J.; Yoon, J. W.; Lee, C. S.; Bae, Y. S.; Kim, J. H. Covalent Organic Framework-Derived Microporous Carbon Nanoparticles Coated with Conducting Polypyrrole as an Electrochemical Capacitor. *Appl. Surf. Sci.* **2018**, *439*, 833–838. https://doi.org/10.1016/j.apsusc.2018.01.103.

(64) Wang, P.; Wu, Q.; Han, L.; Wang, S.; Fang, S.; Zhang, Z.; Sun, S. Synthesis of Conjugated Covalent Organic Frameworks/Graphene Composite for Supercapacitor Electrodes. *RSC Adv.* **2015**, *5* (35), 27290–27294. https://doi.org/10.1039/c5ra02251g.

(65) Kou, Y.; Xu, Y.; Guo, Z.; Jiang, D. Supercapacitive Energy Storage and Electric Power Supply Using an Aza-Fused π-Conjugated Microporous Framework. *Angew. Chemie - Int. Ed.* **2011**, *50* (37), 8753–8757. https://doi.org/10.1002/anie.201103493.

(66) Khattak, A. M.; Ghazi, Z. A.; Liang, B.; Khan, N. A.; Iqbal, A.; Li, L.; Tang, Z. A Redox-Active 2D Covalent Organic Framework with Pyridine Moieties Capable of Faradaic Energy Storage. *J. Mater. Chem. A* **2016**, *4* (42), 16312–16317. https://doi.org/10.1039/c6ta05784e.

(67) Noofeli, A.; Hall, P. J.; Rennie, A. J. R. Ionic Liquid Based EDLCs: Influence of Carbon Porosity on Electrochemical Performance. *Faraday Discuss.* **2014**, *172* (0), 163–177. https://doi.org/10.1039/c4fd00057a.

(68) Kim, C. H.; Wee, J. H.; Kim, Y. A.; Yang, K. S.; Yang, C. M. Tailoring the Pore Structure of Carbon Nanofibers for Achieving Ultrahigh-Energy-Density Supercapacitors Using Ionic Liquids as Electrolytes. *J. Mater. Chem. A* **2016**, *4* (13), 4763–4770. https://doi.org/10.1039/c5ta10500e.

(69) Zhou, D.; Wang, H.; Mao, N.; Chen, Y.; Zhou, Y.; Yin, T.; Xie, H.; Liu, W.; Chen, S.; Wang, X. High Energy Supercapacitors Based on Interconnected Porous Carbon Nanosheets with Ionic Liquid Electrolyte. *Microporous Mesoporous Mater.* **2017**, *241*, 202–209. https://doi.org/10.1016/j.micromeso.2017.01.001.

(70) Tran, C.; Lawrence, D.; Richey, F. W.; Dillard, C.; Elabd, Y. A.; Kalra, V. Binder-Free Three-Dimensional High Energy Density Electrodes for Ionic-Liquid Supercapacitors. *Chem. Commun.* **2015**, *51* (72), 13760–13763. https://doi.org/10.1039/c5cc04359j.

(71) Yao, B.; Chandrasekaran, S.; Zhang, J.; Xiao, W.; Qian, F.; Zhu, C.; Duoss, E. B.; Spadaccini, C. M.; Worsley, M. A.; Li, Y. Efficient 3D Printed Pseudocapacitive Electrodes with Ultrahigh MnO 2 Loading. *Joule* **2019**, *3* (2), 459–470. https://doi.org/10.1016/j.joule.2018.09.020.

(72) Maiti, U. N.; Lim, J.; Lee, K. E.; Lee, W. J.; Kim, S. O. Three-Dimensional Shape Engineered, Interfacial Gelation of Reduced Graphene Oxide for High Rate, Large Capacity Supercapacitors. *Adv. Mater.* **2014**, *26* (4), 615–619. https://doi.org/10.1002/adma.201303503.

(73) Sun, H.; Mei, L.; Liang, J.; Zhao, Z.; Lee, C.; Fei, H.; Ding, M.; Lau, J.; Li, M.; Wang, C.; et al. Three-Dimensional Holey-Graphene/Niobia Composite Architectures for Ultrahigh-Rate Energy Storage. *Science.* **2017**, *356* (6338), 599–604. https://doi.org/10.1126/science.aam5852.

(74) Gallagher, K. G.; Trask, S. E.; Bauer, C.; Woehrle, T.; Lux, S. F.; Tschech, M.; Lamp, P.; Polzin, B. J.; Ha, S.; Long, B.; et al. Optimizing Areal Capacities through Understanding the Limitations of Lithium-Ion Electrodes. *J. Electrochem. Soc.* **2015**, *163* (2), A138–A149. https://doi.org/10.1149/2.0321602jes.

(75) Ma, X.; Zhao, L.; Yu, Z.; Wang, X.; Song, X.; Ning, G.; Gao, J. Excellent Compatibility of the Gravimetric and Areal Capacitances of an Electric-Double-Layer Capacitor Configured with S-Doped Activated Carbon. *ChemSusChem* **2018**, *11* (21), 3766–3773. https://doi.org/10.1002/cssc.201801767.

(76) Zhi, L.; Li, T.; Yu, H.; Chen, S.; Dang, L.; Xu, H.; Shi, F.; Liu, Z.; Lei, Z. Hierarchical Graphene Network Sandwiched by a Thin Carbon Layer for Capacitive Energy Storage. *Carbon N. Y.* **2017**, *113*, 100–107. https://doi.org/10.1016/j.carbon.2016.11.036.

(77) Mei, B. A.; Munteshari, O.; Lau, J.; Dunn, B.; Pilon, L. Physical Interpretations of Nyquist Plots for EDLC Electrodes and Devices. *J. Phys. Chem. C* **2018**, *122* (1), 194–206. https://doi.org/10.1021/acs.jpcc.7b10582.

(78) Ogihara, N.; Kawauchi, S.; Okuda, C.; Itou, Y.; Takeuchi, Y.; Ukyo, Y. Theoretical and Experimental Analysis of Porous Electrodes for Lithium-Ion Batteries by Electrochemical Impedance Spectroscopy Using a Symmetric Cell. *J. Electrochem. Soc.* **2012**, *159* (7), A1034–A1039. https://doi.org/10.1149/2.057207jes.

(79) Ogihara, N.; Itou, Y.; Sasaki, T.; Takeuchi, Y. Impedance Spectroscopy Characterization of Porous Electrodes under Different Electrode Thickness Using a Symmetric Cell for High-Performance Lithium-Ion Batteries. *J. Phys. Chem. C* **2015**, *119* (9), 4612–4619. https://doi.org/10.1021/jp512564f.

(80) Kondratowicz, I.; Nadolska, M.; Zelechowska, K. Reduced Graphene Oxide Joins Graphene Oxide to Teach Undergraduate Students Core Chemistry and Nanotechnology Concepts. *J. Chem. Educ.* **2018**, *95* (6), 1012–1017. https://doi.org/10.1021/acs.jchemed.7b00568.

(81) Yang, H.; Zhang, T.; Jiang, M.; Duan, Y.; Zhang, J. Ambient Pressure Dried Graphene Aerogels with Superelasticity and Multifunctionality. *J. Mater. Chem. A* **2015**, *3* (38), 19268–19272. https://doi.org/10.1039/c5ta06452j.

(82) Brun, N.; Yu, S.-H.; White, R. J. CHAPTER 6. Porous Hydrothermal Carbon Materials, Nanoparticles, Hybrids and Composites; White, R., Ed.; Royal Society of Chemistry, 2015; pp 156–190. https://doi.org/10.1039/9781782622277-00156.

(83) Kim, B. K.; Sy, S.; Yu, A.; Zhang, J. Electrochemical Supercapacitors for Energy Storage and Conversion. *Handb. Clean Energy Syst.* **2015**, 1–25. https://doi.org/10.1002/9781118991978.hces112.

(84) Zhao, C. F.; Lu, K.; Ma, H. Direct Interfacial Growth of MnO2 Nanoparticles on Carbon Nanofiber Surfaces for High-Performance Asymmetric Supercapacitors. *RSC Adv.* **2016**, *6* (109), 107638–107643. https://doi.org/10.1039/c6ra23195k.

(85) MacHado, B. F.; Serp, P. Graphene-Based Materials for Catalysis. *Catal. Sci. Technol.* **2012**, *2* (1), 54–75. https://doi.org/10.1039/c1cy00361e.

(86) Yang, W.; Xu, S.; Ma, K.; Wu, C.; Gates, I. D.; Ding, X.; Meng, W.; Gao, Z. Geometric Structures, Electronic Characteristics, Stabilities, Catalytic Activities, and Descriptors of Graphene-Based Single-Atom Catalysts. *Nano Mater. Sci.* **2019**, No. October. https://doi.org/10.1016/j.nanoms.2019.10.008.

(87) Ji, S.; Chen, Y.; Wang, X.; Zhang, Z.; Wang, D.; Li, Y. Chemical Synthesis of Single Atomic Site Catalysts. *Chem. Rev.* **2020**, acs.chemrev.9b00818. https://doi.org/10.1021/acs.chemrev.9b00818.

(88) Steel, P. J. Aromatic Nitrogen Heterocycles as Bridging Ligands; a Survey. *Coord. Chem. Rev.* **1990**, *106* (C), 227–265. https://doi.org/10.1016/0010-8545(60)80005-7.

(89) Bakandritsos, A.; Pykal, M.; Boński, P.; Jakubec, P.; Chronopoulos, D. D.; Poláková, K.; Georgakilas, V.; Čépe, K.; Tomanec, O.; Ranc, V.; et al. Cyanographene and Graphene Acid: Emerging Derivatives Enabling High-Yield and Selective Functionalization of Graphene. *ACS Nano* **2017**, *11* (3), 2982–2991. https://doi.org/10.1021/acsnano.6b08449.

(90) Medveď, M.; Zoppellaro, G.; Ugolotti, J.; Matochová, D.; Lazar, P.; Pospíšil, T.; Bakandritsos, A.; Tuček, J.; Zbořil, R.; Otyepka, M. Reactivity of Fluorographene Is Triggered by Point Defects: Beyond the Perfect 2D World. *Nanoscale* **2018**, *10* (10), 4696–4707. https://doi.org/10.1039/c7nr09426d.

(91) Sandford, C.; Edwards, M. A.; Klunder, K. J.; Hickey, D. P.; Li, M.; Barman, K.; Sigman, M. S.; White, H. S.; Minteer, S. D. A Synthetic Chemist's Guide to Electroanalytical Tools for Studying Reaction Mechanisms. *Chem. Sci.* **2019**, *10* (26), 6404–6422. https://doi.org/10.1039/c9sc01545k.

(92) Shao, M.; Chang, Q.; Dodelet, J. P.; Chenitz, R. Recent Advances in Electrocatalysts for Oxygen Reduction Reaction. *Chem. Rev.* **2016**, *116* (6), 3594–3657. https://doi.org/10.1021/acs.chemrev.5b00462.

(93) Safizadeh, F.; Ghali, E.; Houlachi, G. Electrocatalysis Developments for Hydrogen Evolution Reaction in Alkaline Solutions - A Review. *Int. J. Hydrogen Energy* **2015**, *40* (1), 256–274. https://doi.org/10.1016/j.ijhydene.2014.10.109.

APPENDIX A

Reduced Graphene Oxide (rGO) Supercapacitors

Introduction

With the advent of portable electronic devices and electric vehicles, there has been an ever-increasing demand for fast charging (high power) and long lasting (high energy) energy storage. Capacitors fill the niche for high power applications, but suffer from low energy density while batteries fulfill the opposite need; high energy density but low power. Supercapacitors strike a balance between the two, possessing both high power and energy densities.

Supercapacitors have high capacities (compared to conventional capacitors) that function through fast surface-based interactions. Electric double layer capacitors (EDLCs) are a type of supercapacitor that operate through the electric double layer effect, where ions are adsorbed on the surface of a charged material and two layers of opposite charges develop. This separation of charges generates a capacitance (similar to a classical capacitor) and can be used to power devices. Since there is no electron transfer during the surface adsorption, EDLCs can be quickly cycled (high power) and have a long lifetime. However, because no charge transfer occurs the total energy able to be stored is low.

The source of ions in an EDLC is the electrolyte. Various electrolytes are available and each one imparts different properties on the resultant device. Aqueous electrolytes, which usually consist of a strong acid or base, can by cycled extremely fast due to the high mobility of H^+ and OH^-. However, due to the small voltage window, aqueous electrolytes have a limited energy density. Meanwhile, organic electrolytes and ionic liquids lack high ion mobility but have a large voltage window allowing for high energy density.

The most vital properties of a supercapacitor material include high surface area and high electronic conductivity. To this end, activated carbons are the industry standard for supercapacitor materials, however novel nanomaterials like graphene have been considered. Graphene is an allotrope of carbon arranged in a 2D monolayer and is an attractive alternative due to its unique properties like high electrical conductivity, mechanical strength, surface area, and flexibility. However, its production has been limited due to painstaking and expensive synthesis methods like mechanical exfoliation and chemical vapor deposition (CVD). A more facile synthetic route of graphene production is through a solution processable method which involves the reduction of graphene oxide (GO) to produce reduced graphene oxide (rGO). Compared to CVD grown graphene, rGO has a lower conductivity and more defects, but is far more processable. Due to the ease of synthesis, rGO has proliferated as the main method for graphene production.

When GO is dispersed in water and reduced under the right conditions, rGO hydrogels can be formed. The oxygen groups on GO are hydrophilic, making the GO very soluble in water. As the GO is reduced to rGO, these hydrophilic groups are removed, and hydrophobic graphene domains develop. This forces the sheets to self-assemble into a macroscopic 3D structure comprised of intertwined rGO sheets through hydrophobic forces, as well as π-π interaction between graphene sheets.

In this lab you will synthesize 3D graphene hydrogels from the reduction of graphene oxide. Next you will probe the electrochemical properties of the hydrogels in the presence of different electrolytes. You will assemble symmetric double layer capacitor devices and perform

cyclic voltammetry and galvanostatic charge discharge test on each to access the performance of the devices.

Procedure

Overview

Day 1 Synthesize hydrogels.

Day 2 Make electrodes.

Day 2-3 perform electrochemical measurements.

Hydrogel Synthesis (Day 1)

1. Prepare around 1 mL of a 1 M solution of ascorbic acid. Sonicate the solution to dissolve properly.
2. You will need to make 15 mL of solution total for all the hydrogels. To a single container, add 0.60 mL of the ascorbic solution, followed by the appropriate amount of stock GO and water so that the final concentration will be 1.5 mg/mL GO **after all reagents are added together**.
3. After shaking the solution from step 2 vigorously, then sonicating for 5 minutes, pipette 1 mL of the solution into a small black cap vial (8 mL dram vials). Do this pipetting for 14 total vials. **Cap the vials tightly**.
4. Put the vials into an oven at 80 °C for 1 hour to begin the reduction of the GO.
5. After the reduced graphene oxide (rGO) hydrogels have formed, **carefully** remove the hydrogels from the vials and place them all into a beaker (using a spatula is best, tweezers sometimes puncture the hydrogels and adding some water to the vials and beaker will make the transfer easier). Wash out the dram vials and return them to your box.
6. Carefully fill the beaker with fresh DI water in order to wash the hydrogels. After waiting 2 minutes, pour out the water and fill the beaker with fresh water. Wait 5 more minutes.
7. Pour out the water and refill the beaker with new water. Wait about 10 minutes, then remove **half** of the hydrogels from the container and place them on a petri dish.
8. Place these hydrogels into a freezer to freeze. Take the remaining hydrogels out of the beaker and place them on another petri dish, lined with a paper towel. Leave these non-frozen hydrogels out in open air in place they won't be disturbed.
9. Check on the frozen hydrogels. If they have fully frozen (about 25 – 30 minutes) transfer the frozen hydrogels to a petri dish lined with a paper towel. Place the petri dish out in the open air in a place they won't be disturbed to dry.

Electrode Preparation (Day 2)

1. Prepare the electrolyte solutions. You will need 5 mL of 1.0 M H_2SO_4 and 5 mL of 1-Ethyl-3-methylimidazolium tetrafluoroborate ([EMIM][BF_4]). **Caution: concentrated H_2SO_4 is very caustic, please use caution when handling.**
2. Carefully weigh the hydrogels that were previously frozen. Find a pair of the hydrogels that are close in weight, record the average, and place them in a scintillation vial (20 mL white cap vial). Do this 1 more time, for a total of 2 pairs of hydrogels.

3. Add a different electrolyte to each pair; 1.0 M H_2SO_4 or [EMIM][BF_4]. Use a few mL of the aqueous electrolytes to saturate the hydrogels. For [EMIM][BF_4] use a very small amount, but enough to fully saturate the hydrogels.
4. Let the hydrogels soak for at least 1 hour before testing.
5. Repeat step 2 – 4 for the non-frozen hydrogels.
6. For the separator, cut out 4 pieces of filter paper wider than the stainless strips.
7. You should have a total of 4 hydrogel pairs.
8. The stainless-steel strips are sputtered with gold to enhance contact resistance. If the strips appear scratched, sputter the stainless-steel strips with gold for 2-3 minutes.

Electrochemical Testing (Day 2-3)

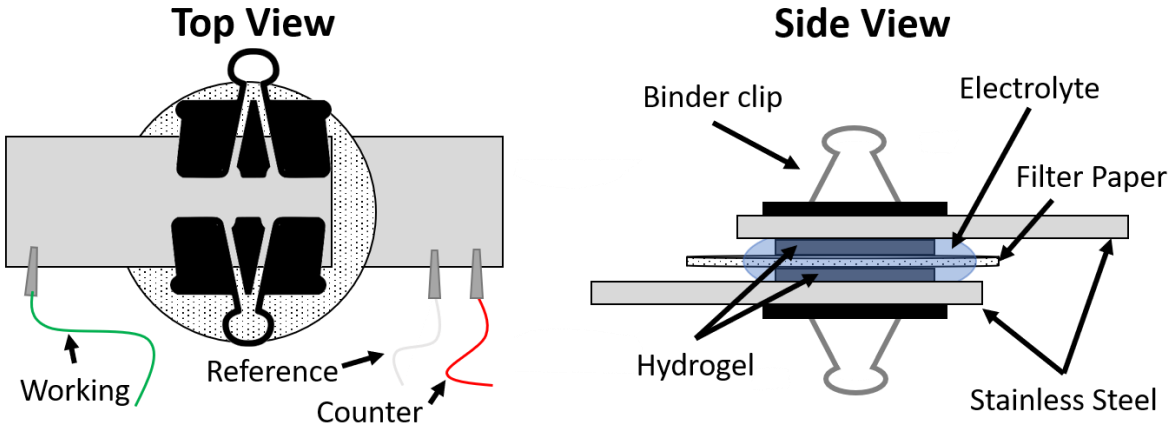

1. Make a symmetric cell, pictured above with each hydrogel pair. In order from bottom to top, stack a hydrogel on top of a stainless-steel strip, then a piece of filter paper soaked in the appropriate electrolyte, followed by the other hydrogel. Lastly, lay another stainless-steel strip on top offset from the bottom layer. Secure the entire device with two binder clips. **Be sure the bare metal strips don't touch directly!**
2. Attach the working electrode (green wire) to one of the stainless-steel strips. To the other, attach both the reference (white) and counter (red) electrode.
3. Perform cyclic voltammetry (CV) on each device (see the *"Cyclic Voltammetry Guidelines"* document on CCLE for a detailed guide). Make sure to set the voltage window to 0 - 1.0 V for the aqueous electrolyte, and 0 - 2.5 V for [EMIM][BF_4]. Scan both forwards and backwards at a scan rate of 25 mV/s, for 3 cycles. Save the data, and do the same process for 50, 100, and 200 mV/s. Do this scan rate test for each device. Graph the CV's at different scan rates for each electrolyte.
4. Next, perform galvanostatic charge/discharge (GCD) on each device, termed chronopotentiometry (see the *"Charge Discharge Guidelines"* document on CCLE for a detailed guide). Set the voltage limits according to the CV experiment. Apply a current so that the total current density applied is 0.5 A/g. **Check your units!!!** You can calculate this by multiplying the current density by the average weight of the electrodes. Let the supercapacitor cycle 3 times. Do this for 1, 2, 3, 5 A/g. For aqueous supercapacitors do additional tests for 7.5, 12.5, and 20 A/g. If the aqueous cycling curves are stable, try increasing the current density by an additional 10 A/g until failure (the instrument either fails to run the test, or the curves are severely deformed). Save the data for each current

density tested. **Caution: pay attention to the voltage during cycling. If the voltage jumps well outside the window set (e.g. the voltage window is 0 – 1, and the instrument reads >1.5 V), stop the test, and consult the TA**

5. Using the equations provided, calculate the last cycle's total discharge time for each current density to determine the specific capacity (in F/g), energy density (Wh/kg), and power density (W/kg). Make a graph of the capacity vs current density for each electrolyte from 0.5 – 5 A/g. Plot each electrolyte's energy density vs power density one a single graph (including the additional data form the aqueous tests), with **log scale axes**.
6. Lastly, charge a supercapacitor to its maximum voltage using a single sweep of the GCD program at 1 A/g. Attach the supercap to a LED, and record the results.

WASTE: All chemicals used in the **"Hydrogel Synthesis" steps are safe to pour down the drain! All chemicals used in the **"Electrode Preparation" and "Electrochemical Testing" steps** must be poured into the correct waste container. Used electrodes can be places into the solid waste bag.**

Calculations:

Specific Capacity (F/g): $C_g = 2\frac{I\Delta t}{m\Delta V}$

Energy (Wh/kg): $E = \frac{1}{8}C_g V^2$

Power (W/kg): $P = \frac{E}{\Delta t/3600}$

- I = charge/discharge current (A)
- Δt = discharge time (s)
- m = Mass of one electrode (g)
- Δ = voltage window (V)

Some Thought Questions:

1. What is the purpose of the ascorbic acid in this lab?
2. Why is it important to wash the rGO hydrogels several times?
3. Why is the voltage window for H_2SO_4 1.0 V? What would happen if you went above this voltage?
4. Qualitatively, how do the CV's of each electrolyte compare? *Hint: What is the shape expected for a supercapacitor.*
5. Are there differences in the specific capacity in each electrode? Explain and differences in the values obtained.
6. Using all the information available, which electrolyte is best for high energy applications? What about high power applications?
7. In your opinion, do you think supercapacitors can replace current lithium ion batteries in portable electronics?